THE ANALYSIS OF OFFSHORE FOUNDATIONS SUBJECTED TO COMBINED LOADING

by

Ross Wesley Bell

A thesis submitted for the
Degree of Master of Science
at the University of Oxford

Wolfson College

Hilary Term, 1991

ABSTRACT

Ross Wesley Bell
Wolfson College

Master of Science
Hilary Term, 1991

The Analysis of Offshore Foundations
Subjected to Combined Loading

Shallow offshore foundations, which achieve their stability through the foundation bearing on the seabed, can in most applications be idealised as large rigid circular footings subjected to vertical, horizontal and moment loading. A small strain linear-elastic perfectly-plastic three-dimensional finite element program was developed to analyse this combined loading problem.

The selection of a suitable three-dimensional finite element for accurate and computationally efficient analysis was based on the element's ability to model incompressible soil conditions, using exact numerical integration. A new approach for evaluating element suitability is developed and is quantified in terms of the parameter *free* degrees-of-freedom (equal to the degrees-of-freedom minus the incompressibility constraints). The tetrahedron family of three-dimensional elements is found to be in general more suitable and computationally efficient than the Serendipity and Lagrangian cube families. The 20-node quadratic strain tetrahedron is adopted for all analyses presented in this thesis.

For combined loading, most of the available elastic analytical solutions are for rigid circular footings placed at the surface. Finite element analyses reveal certain inadequacies in some of these solutions. The elastic numerical analyses also examine the effect of footing embedment for three cases of embedment geometry. This demonstrates that the increase in footing stiffness (reduction in displacement) due to embedment for horizontal and moment loading is developed at shallower depths, and has a greater magnitude, than for vertical loading.

The stability of a rough rigid circular footing placed on the surface of an undrained clay is examined. Zero thickness interface elements, despite experiencing some numerical instability problems, were found to model the footing-soil interaction better than conventional continuum elements. However, application of interface elements to footings which can lose contact with the soil, under moment loading conditions, resulted in numerical instability of the solution. A simpler model was therefore used to define the shape of the three-dimensional failure envelope at high vertical load. Comparisons with the semi-empirical inclination factors of bearing capacity solutions are included.

CONTENTS

ACKNOWLEDGEMENTS

I gratefully acknowledge the support that I have received as a Commonwealth Scholar, and extend my sincere thanks to the Association of Commonwealth Universities (ACU) and the British Council, who jointly administered this award.

I would like to thank Dr Guy Houlsby for his supervision of this project, and his unending guidance and stimulation. Dr Houlsby generously allowed me to use the following two-dimensional programs: OXFEM - finite element analysis, OXMESH - mesh generation, and 2CAN - data contouring.

My thanks also go to Dr Harvey Burd, who was my joint supervisor with Dr Houlsby during the first 12 months of this project. I am also indebted to Dr Burd for allowing me to use OXFEM in the development of the three-dimensional finite element program OXFEM2.

My sincere thanks go to all other members of the Soil Mechanics Group for their friendship and assistance during my study. Special thanks are given to Dr Hai-Sui Yu, Mr Chris Brocklehurst, and Mr Paul Norris. I am also grateful to Mr Chris Martin for proof reading this thesis.

My love and appreciation is extended to my wife Jacqueline for her unfailing support and encouragement during my studies at Oxford.

Finally, my deepest thanks are given to my family and friends in Western Australia who wrote constantly, and thereby made the distance apart not seem so great.

Science is the topography of ignorance .... The best part of our knowledge is that which teaches us where knowledge leaves off and ignorance begins.

Oliver Wendell Holmes
1809-1894

To Sheba,
my childhood
companion

NOMENCLATURE

A	Footing base area
A	Two-dimensional element area
A_b	Plan area of the foundation-soil contact surface
A_w	Area of the footing sidewall-soil interface
A'	Effective contact area
b_n	Computational effort per node
B'	Effective contact width
$[\mathbf{B}]$	Matrix relating strains to nodal displacements
$[\mathbf{B}_i]$	Matrix relating relative velocities to nodal velocities
c	Shear strength in triaxial compression
c_e	Number of constraints per element
C	Interface element material stiffness control parameter
CONTOL	Stiffness formulation control parameter
CONV	Convergence parameter
d_c^*	Ratio of the degrees-of-freedom to constraints in the limit as the mesh is uniformly refined
d_e^*	Number of degrees-of-freedom per element in the limit as the mesh is uniformly refined
D	Mesh dimension
$[\mathbf{D}]^e$	Element material elastic stiffness matrix
$[\mathbf{D}]^{ep}$	Element material elasto-plastic stiffness matrix
$[\mathbf{D}]^p$	Element material plastic stiffness matrix
$[\mathbf{D}_i]^e$	Interface element material elastic stiffness matrix
$[\mathbf{D}_i]^{ep}$	Interface element material elasto-plastic stiffness matrix
$[\mathbf{D}_i]^p$	Interface element material plastic stiffness matrix
e	Number of elements
e	Non-dimensional eccentricity parameter
$\dot{\mathbf{e}}$	Vector of incremental deviatoric strain rates
f_e^*	Number of free degrees-of-freedom per element in the limit as the mesh is uniformly refined
f_n^*	Number of free degrees-of-freedom per node in the limit as the mesh is uniformly refined
$f(\boldsymbol{\sigma})$	Yield function
F_1	Vertical flexibility coefficient
F_2	Horizontal flexibility coefficient
F_3	Rotation flexibility coefficient

F_4	Horizontal and rotation cross coupling flexibility coefficient
$\mathbf{F}$	Vector of nodal forces in equilibrium with the computed displacements
$g(\boldsymbol{\sigma})$	Plastic potential
G	Elastic shear modulus
H	Horizontal footing load
i_c, i_c^a	Inclination factors
$[\mathbf{J}]$	Jacobian of the transformation from global (x, y, z) to local coordinates (α, β, γ)
$[\mathbf{J}_i]$	Jacobian of the transformation from global (x, y) to local coordinates (α, β)
k	Number of mesh interior nodes
K	Non-dimensionalised vertical stiffness
K	Elastic bulk modulus
K_n	Interface element normal stiffness
K_n^{res}	Residual interface normal stiffness after loss of footing contact
K_s	Interface element tangent stiffness
K_s^{res}	Residual interface tangent stiffness after loss of footing contact
K_1	Vertical stiffness coefficient
K_2	Horizontal stiffness coefficient
K_3	Moment stiffness coefficient
K_4	Horizontal and moment cross coupling stiffness coefficient
$K_1^z, K_2^z, K_3^z, K_4^z$	Stiffness coefficients at a depth z.
K_3^s	Moment stiffness at the surface level
K_4^s	Cross coupling stiffness at the surface level
K_3^m	Moment stiffness at the metacentre
K_{1emb}/K_{1surf}	Ratio of the vertical stiffness of an embedded footing to the vertical stiffness of an equivalent surface footing
K_{2emb}/K_{2surf}	Ratio of the horizontal stiffness of an embedded footing to the horizontal stiffness of an equivalent surface footing
K_{3emb}^m/K_{3surf}^m	Ratio of the metacentre moment stiffness of an embedded footing to the metacentre moment stiffness of an equivalent surface footing
$[\mathbf{K}]$	Element tangent stiffness matrix
$[\mathbf{K}_i]$	Interface element tangent stiffness matrix
l	Number of local nodes per element
L'	Effective contact length
m	Sum of the internal nodal angles divided by π
M	Footing moment
n	Number of nodes
n	Number of sectors per quadrant

n_e^*	Ratio of number of nodes to number of elements in the limit as the mesh is uniformly refined
N	Order to which the element polynomial interpolation function is complete
$[\mathbf{N}_i]$	Interface element shape functions
p	Mean stress
$\mathbf{P}$	Vector of external applied loads
q_V	Vertical bearing capacity
r	Number of mesh edge nodes
R	Radius of a circular footing
R_{foot}	Radius of the node defining the footing edge in the three-dimensional mesh
s	Number of mesh face nodes
s_c, s_c^a	Shape factors
s_u	Undrained shear strength of clay
STATE	Constitutive state parameter
$\mathbf{S}$	Vector of deviatoric stresses
t	Time variable
t	Normalised time interval
t'	Remainder of normalised time variable
T	Torsional moment
$\dot{u}$, $\dot{v}$ and $\dot{w}$	Velocities in the x, y and z directions
u_H	Horizontal footing displacement
u_V	Vertical footing displacement
u_{Vemb}	Vertical settlement of an embedded footing
u_{Vsurf}	Vertical settlement of a surface footing
$\mathbf{u}_r$	Vector of relative velocities
$\mathbf{U}$	Vector of nodal displacements
$\dot{v}$	Incremental volumetric strain rate
V	Vertical footing load
V	Element volume
(V^*, H^*, M^*)	Non-dimensional combined loading space
(x, y, z)	Global coordinates
z_D	Depth of footing embedment
z_m	Metacentre depth
α	Angle of inclination of load P to the vertical
(α, β, γ)	Local coordinates
β	Sector angle (in radians)
Δ	Incremental quantity

$\boldsymbol{\varepsilon}$	Vector of strains
$\dot{\varepsilon}_{kk}$	Volumetric strain rate
θ	Internal nodal angle
θ_M	Footing rotation
θ_T	Torsional rotation
μ_{trench}	Reduction in surface settlement for a footing embedded in a trench with no side wall contact
μ_{wall}	Reduction in surface settlement due to part of the applied load being transmitted to the ground through shear tractions acting along the vertical sides of the footing wall
ν	Poisson's ratio
$\boldsymbol{\sigma}$	Vector of stresses

CHAPTER 1 INTRODUCTION

1.1 Background

With the continually increasing demand for oil and gas, exploration and production has moved ever more into the offshore environment. Prior to the 1970s most offshore structures were confined to areas of shallow water depths of approximately 100 m and were tower platforms, generally constructed of tubular steel components (Prevost *et al*, 1981). With the onset of the North Sea oilfield development in the 1970s, gravity structures were developed in order to withstand the hostile environmental forces encountered. In subsequent years steel tower platforms have been constructed in over 300 m of water (Poulos, 1988).

Offshore foundations can be grouped into two main categories: those which achieve their stability through a piled foundation that effectively pins the structure to the seabed, for example tower platforms, and those which achieve stability through the action of the foundation bearing on the seabed. This latter category is commonly referred to as shallow foundations and is the focus of the research presented in this thesis. Shallow bearing foundations can be largely classified into three broad types: foundations of gravity structures, "spudcan" footings of jack-up oil rigs, and mudmats for piled structures. These are illustrated schematically in Figure 1.1 giving typical dimensions.

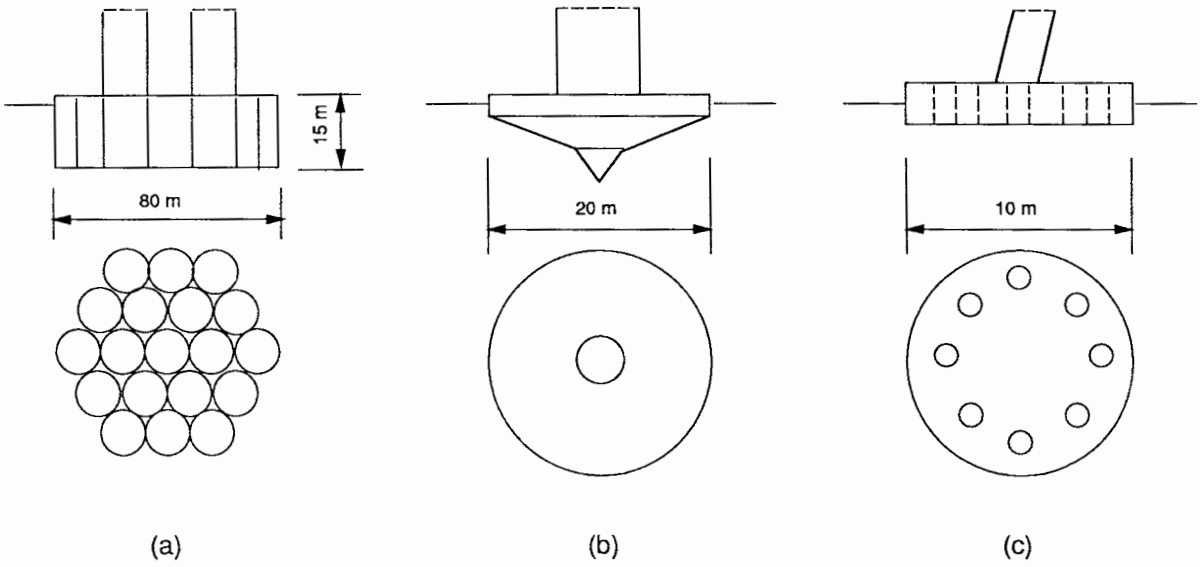

Figure 1.1: Examples of bearing offshore foundations: (a) Gravity foundation, (b) Spudcan footing, (c) Mudmat for piled structure.

In terms of size, gravity structures and their foundations (Figure 1.1a) are an order of magnitude larger than platforms previously built, and achieve stability through their own weight. They are generally installed in water depths of 100-150 m on the unprepared sea bed in favourable foundation conditions, such as either dense sand or stiff clay. Between 1973 and 1986, a total of 17 gravity structures were installed in the North Sea (Poulos, 1988).

Mobile jack-up rigs are used extensively to drill oil and gas wells in water depths of up to about 100 m and typically stay on location for only a few months (Poulos, 1988). They consist of a floatable drilling platform supported on three or more legs which can be raised and lowered (Figure 1.2). A thorough description of the installation procedure is given by Tan (1990). A jack-up platform can have either a common mat foundation, where all legs are supported on a continuous mat, or an independent footing foundation system, as shown in Figure 1.2, where each leg is supported by a separate footing (Arnesen, 1988). Most modern jack-up platforms correspond to the latter category and have approximately conical shaped footings with a protruding tip at the centre. These are commonly referred to as "spudcan" footings (Figure 1.1b).

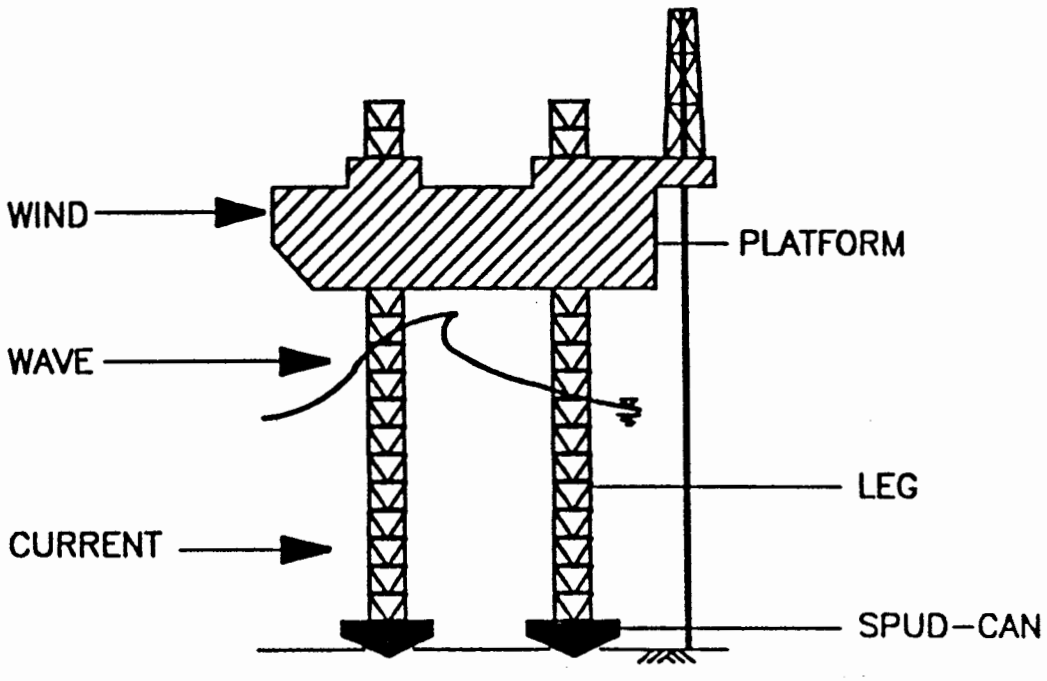

Figure 1.2: Jack-up platform and environmental loads (after Tan, 1990).

Mudmats are required in many cases to provide additional temporary support for jacket and tower structures prior to foundation pile installation. Many different shapes and sizes of mudmats have been used. One particular application of a mudmat is shown schematically in Figure 1.1c, where the mudmat has holes through which piles are installed.

Offshore structures are subjected to gravity and environmental loads. Gravity loads correspond to the weight of the structure and act vertically. As shown in Figure 1.2, environmental loads consist of wave, wind and current components and act laterally producing horizontal and moment loads at the foundation. The loads encountered in offshore foundations differ from those in onshore foundations in two main ways. Firstly, under storm conditions, offshore foundations can be subjected to horizontal forces that range up to 30 % of the total vertical load, thereby producing a correspondingly large moment (Poulos, 1988). Onshore foundations are subjected to much smaller lateral loads, typically no more than 5 % of the vertical load. Secondly, for design purposes, it may be safely assumed that onshore foundations are subjected to static loading, while for offshore foundations a major cyclic component of vertical and horizontal loads is present, and cannot be disregarded. This study, however, does not address the issue of cyclic loading.

1.2 Problem Definition

In a theoretical study of this nature, it is important to have a clear definition of the problem identifying the key parameters to be investigated. This function is performed in Figure 1.3 and includes the associated notation and sign convention to be adopted in this thesis.

Bearing offshore foundations can in most applications be idealised as large rigid circular footings, this point being emphasised in the illustrations of Figure 1.1. A circular geometry is considered advantageous in that it can be approximated in many cases by conventional two dimensional axisymmetric formulations and may also be used to approximate the behaviour of other geometrical shapes.

Embedment into the sea bed can significantly affect the behaviour and performance of bearing offshore foundations. Examination of the influence of embedment depth z_D is complicated by the fact that in many cases it is intermediate between the cases of conventional shallow and deep foundations. Note that the footing sidewall boundary condition in Figure 1.3 is dependent on

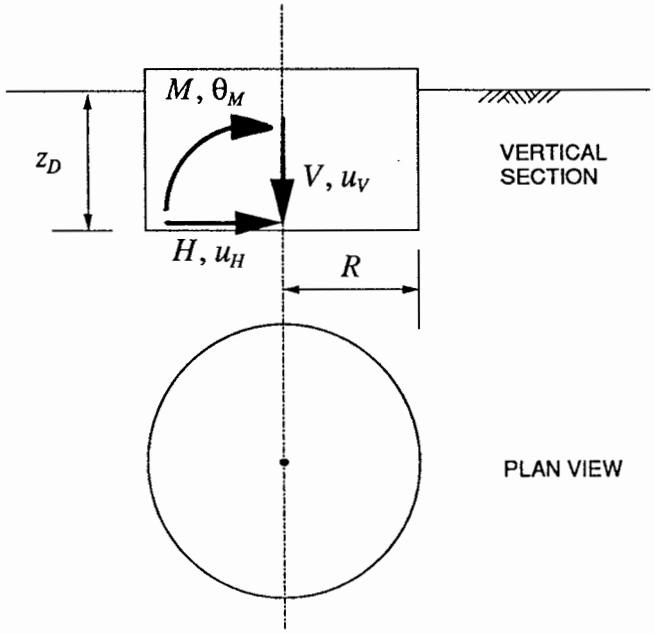

Figure 1.3: Problem definition and key parameters to be investigated.

the embedded foundation considered. As illustrated in the elastic analyses of Chapter 4, this can vary from no sidewall contact (open trench) to full rough contact, and can include the special case of an embedded footing covered with soil.

As demonstrated in Figure 1.2, the wind, wave and current components of the lateral load generally act on an offshore structure in the same direction. The vertical (V), horizontal (H) and moment (M) loads applied to an offshore foundation and resulting deformations (u_V, u_H, θ_M) can therefore be assumed to act in a single vertical plane (Figure 1.3).

1.3 Objective of Study

The design of offshore foundations is a complex problem in which numerous aspects such as installation procedure, cyclic loading, choice of appropriate constitutive model for the soil, and other issues must be examined. However, a significant deficiency in the current design of offshore foundations is the method used in the evaluation of foundation stability under combined loading. These methods are based mainly on empiricism (Meyerhof, 1953; Brinch Hansen, 1970; Vesic, 1975) and are considered inadequate. The elastic behaviour also has important applications in various aspects of offshore foundation design, and, like the stability issue, it has not been thoroughly examined under combined loading and embedment conditions. The main

objective of this study, therefore, is to examine the elastic behaviour and stability of offshore foundations, under combined loading, using both existing analytical solutions and finite element modelling techniques.

1.4 Scope of Thesis

The remainder of this thesis is divided into four main chapters. Chapter 2 describes the elastic-plastic three-dimensional finite element model adopted in this research. Note that whilst the geometry of the problem can be modelled using a conventional two-dimensional axisymmetric formulation, the combination of vertical (V), horizontal (H) and moment (M) loads needs to be modelled by a fully three dimensional finite element analysis. An alternative two-dimensional technique of harmonic loading analysis, where the variation of load and stress in the third dimension is approximated by a Fourier series expansion, is applicable to this problem (Zienkiewicz, 1977). However, its development was beyond the scope of this research.

The choice of a suitable three-dimensional finite element for accurate and computationally efficient analysis of the rigid circular footing problem is not a straightforward decision. Chapter 3 addresses this issue and shows that the most important consideration is the ability of the element to model incompressible soil conditions. A new approach for examining element suitability for modelling incompressibility is introduced, which clearly demonstrates that some elements are better suited computationally than others, while some elements are totally unsuitable. The most appropriate element is chosen for the ensuing analyses of Chapters 4 and 5. The chapter concludes by presenting the mesh generator developed and used in this research.

As a preliminary to carrying out stability calculations, Chapter 4 presents the results of a thorough elastic analysis of the rigid circular footing problem. Elastic solutions are commonly used in the preliminary estimation of offshore foundation deformations (Poulos, 1988). For combined loading, the bulk of the available analytical solutions corresponds to the theoretically simpler case of a surface footing. Finite element elastic analyses reveal certain inadequacies in these analytical solutions. The elastic analysis is then extended to consider the important effect of footing embedment on the combined loading response.

Chapter 5 presents the preliminary work leading towards a comprehensive analysis of the stability of shallow offshore foundations. The chapter commences with a short review of the existing bearing capacity solutions which attempt to model the combined loading problem. To

account for the loss of contact which occurs when tensile stresses develop between the footing base and the soil, two-dimensional interface elements are introduced to the finite element model. Preliminary plasticity calculations to establish the combinations of loading which cause failure of the foundation are presented. The chapter concludes with a brief comparison of the computed failure envelope with the bearing capacity equations.

CHAPTER 2 THREE DIMENSIONAL FINITE ELEMENT MODEL

2.1 General Comments

This chapter concentrates on the theory and computer implementation of the three-dimensional finite element model adopted in this research.

The finite element method can take many different forms. The displacement finite element method, which is characterised by displacement being the primary unknown variable, is used here. The strains are defined by infinitesimal theory. The element stiffness matrices are evaluated by numerically integrating the stiffnesses at given points, commonly known as "Gauss points". The stresses and strains are similarly evaluated as these points. The model is applicable to the analysis of linear elastic and non-linear elasto-plastic problems.

A major limitation of three-dimensional finite element analysis is the overall computation effort involved (Zienkiewicz, 1977; Cook, 1981), and this has frequently been the motivation for adopting simplified two-dimensional formulations. For many three-dimensional applications, the most computationally intensive part of the analysis is the solution of the stiffness equations. The method described in this chapter attempts to take this into consideration by minimising the number of times equation solution is performed.

2.2 Global Solution Scheme

The governing equations in finite element analysis are derived from the principle of virtual work, which states that the external applied loads (**P**) must be in equilibrium with the internal stresses. This is usually written (Zienkiewicz, 1977)

$$\mathbf{P} = \int_V [\mathbf{B}]^T \boldsymbol{\sigma}\, dV \tag{2.1}$$

where $\boldsymbol{\sigma}$ is the vector of current stresses and the matrix [**B**] relates the strains ($\boldsymbol{\varepsilon}$) to the nodal displacements (**U**) as follows

$$\boldsymbol{\varepsilon} = [\mathbf{B}]\mathbf{U} \tag{2.2}$$

The matrix [**B**] depends on the strain definitions and element shape (displacement) interpolation functions, and for three-dimensional finite elements this is discussed in greater detail by Zienkiewicz (1977). Taking into account the stress-strain relationship represented by the matrix $[\mathbf{D}]^{ep}$, Equation (2.1) can be written in terms of the nodal applied forces (**P**) and nodal displacements (**U**)

$$\mathbf{P} = [\mathbf{K}]\mathbf{U} \tag{2.3}$$

where [**K**] is the tangent stiffness matrix and is expressed as

$$[\mathbf{K}] = \int_V [\mathbf{B}]^T [\mathbf{D}]^{ep} [\mathbf{B}] dV \tag{2.4}$$

In problems where material non-linearities are present, such as the analyses presented in Chapter 5, Equation (2.3) has generally been solved using incremental procedures. Reviews of the many different solution schemes available are provided by Mondkar and Powell (1978) and Sloan (1981). These schemes can be divided into two main categories: iterative Newton-Raphson procedures and non-iterative Euler schemes.

Within each increment, the standard Newton-Raphson scheme adopts an iterative procedure in which the stiffness matrix is updated within each iteration. For most three-dimensional analyses this leads to excessive computing time because of the frequency with which the stiffness matrix is inverted. Various modifications of the Newton-Raphson scheme to counteract this limitation have been proposed. A popular refinement is the constant stiffness method (also commonly known as the initial stress method) where the initial elastic stiffness matrix is used for all increments and iterations. This method, however, is not well suited to problems which exhibit strong non-linearity, such as footing collapse load calculations (Sloan, 1981).

The simplest non-iterative solution scheme is the Euler method in which the exact load-displacement curve is approximated by a series of straight lines having a slope equal to that of the exact curve at the start of the increment. This method is limited in that the error in each increment of analysis is accumulated from one increment to the next, and can therefore furnish results which are significantly not in equilibrium. A more accurate and robust scheme is achieved by evaluating the unbalanced nodal loads at the conclusion of each load step and adding these on to the applied nodal loads for the next increment. A schematic representation of this scheme for a one degree-of-freedom system is presented in Figure 2.1. This scheme was

successfully applied by Sloan (1981) to two-dimensional vertical collapse load calculations and was termed the "modified Euler scheme". Burd (1986) also implemented the same solution scheme for the plane strain analysis of reinforced unpaved roads and Yu (1990) for axisymmetric cavity expansion analyses.

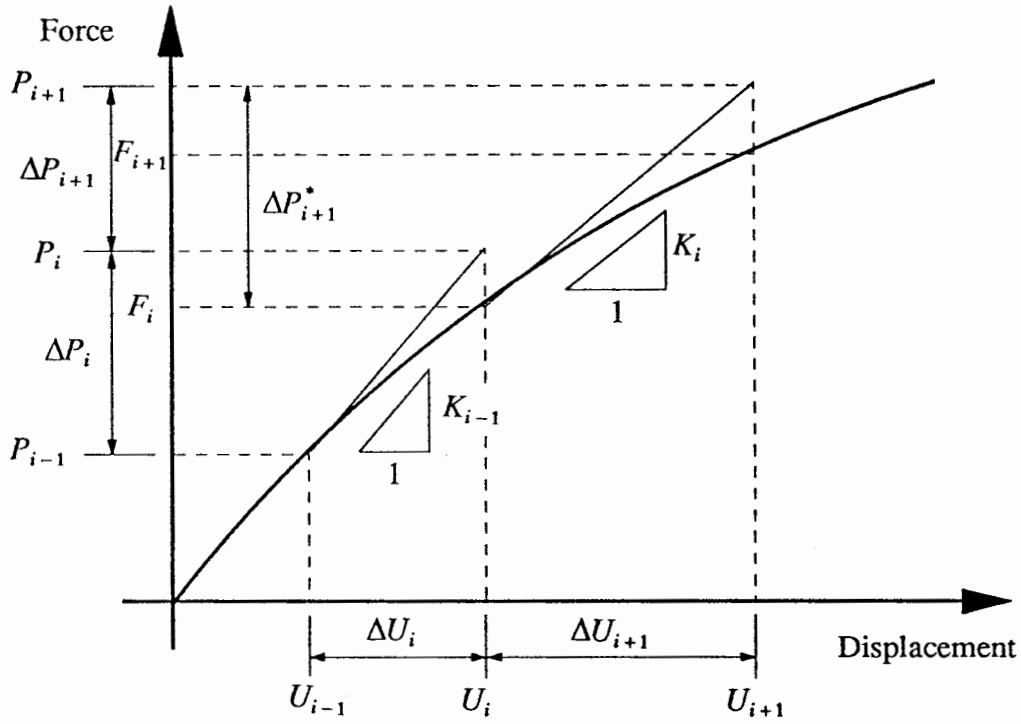

Figure 2.1: Modified Euler solution scheme for a one degree-of-freedom system.

The modified Euler scheme was adopted for all analyses reported in this thesis because of its robust nature and proven record for different types of analysis. However, like most of the Newton-Raphson schemes, it has the serious disadvantage that each increment of analysis involves stiffness matrix formulation and inversion, which for three-dimensional analysis can account for at least 95% of the computing time per increment. This limitation was alleviated by implementing the adaption of the Modified Euler scheme presented in the flow diagram of Figure 2.2. In this case the stiffness matrix is only formulated and inverted when the error in the previous increment of analysis has reached an unacceptable level. The error is measured by the parameter CONV, which is defined in Figure 2.2 and repeated below in its non-incremental form:

$$\text{CONV} = \frac{\Sigma(\mathbf{P}-\mathbf{F})^2}{\Sigma \mathbf{F}^2} \tag{2.5}$$

The vector **F** is the nodal forces in equilibrium with the calculated nodal displacements (**U**) and represents the right hand-side of Equation (2.1). It is computed from the equilibrium stresses in the stress updating phase of the scheme. This important aspect of the analysis is addressed in the following section.

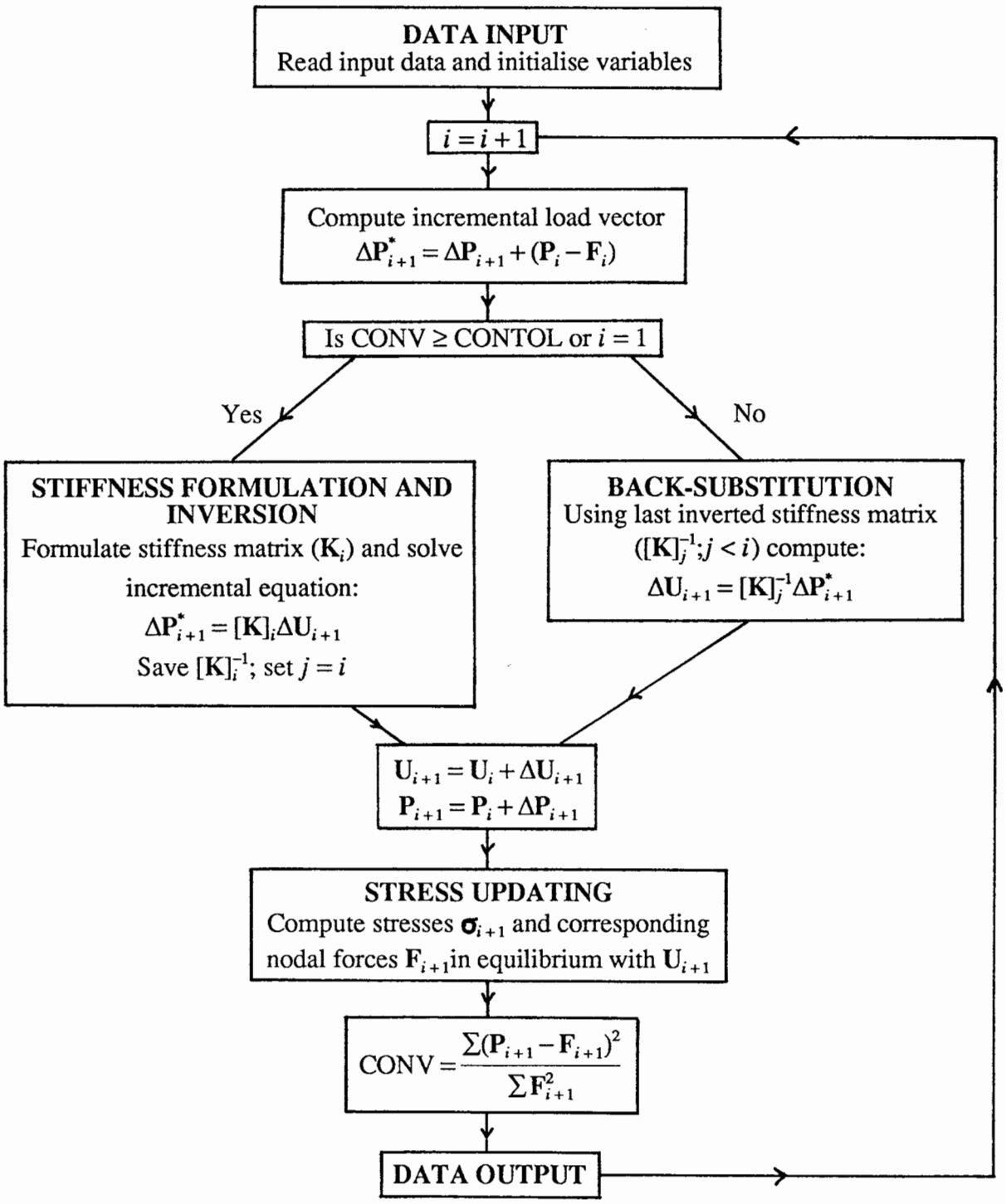

Figure 2.2: Flow diagram of modified Euler scheme with selective stiffness formulation.

Formulation and inversion of the stiffness matrix is controlled by the parameter CONTOL. A typical value of CONTOL adopted in the non-linear analyses of Chapter 5 is 0.0001, which by definition corresponds to about a 1% error in the out of balance nodal forces ($\mathbf{P} - \mathbf{F}$). If CONV is greater than or equal to CONTOL, the stiffness matrix is reformulated and inverted; if CONV is less than CONTOL, the nodal displacements are calculated by multiplying the last inverted stiffness matrix with the current applied loads. This is commonly referred to as "back-substitution". For the analyses presented in Chapter 5, the computing time associated with back-substitution was less than 1% of the time associated with stiffness formulation and inversion.

The "modified Euler scheme with selective stiffness formulation" is a blend between the standard modified Euler scheme and a non-iterative constant stiffness scheme. It reduces to the modified Euler scheme when CONTOL is set to a very small value, and alternatively, the constant stiffness scheme when CONTOL is set to a very large value. Adopting an intermediate value of CONTOL produces a scheme which utilises the advantages of both of these methods. The modified Euler scheme is activated in non-linear sections of the load - displacement curve, and the constant stiffness scheme in reasonably linear sections of the response. The stiffness matrix formulation and inversion, the most computationally expensive part of the analysis, is therefore only performed as many times as required for the level of accuracy defined by CONTOL.

For linear elastic analysis, the same solution scheme is used, except that only a single increment of analysis is required. The equilibrium check of Equation (2.5), not necessary for a single step linear analysis, serves as a useful check that the elastic analysis has been performed accurately. The computed parameter CONV should in this case be zero.

2.3 Elasto-plasticity Model

The most common constitutive law for modelling undrained clay has been the linear-elastic perfectly-plastic Tresca model. However, this has disadvantages under axisymmetric conditions, as examined in this research, because singularities are encountered at the corners of the yield function (Sloan, 1981). Even though corrections can be made for these special cases, the alternative von Mises yield criterion, shown in Figure 2.3, is differentiable everywhere, and is thought to be more realistic for modelling soil behaviour (Wroth and Houlsby, 1985). The linear-elastic perfectly-plastic von Mises yield function has therefore been adopted for all non-linear analyses.

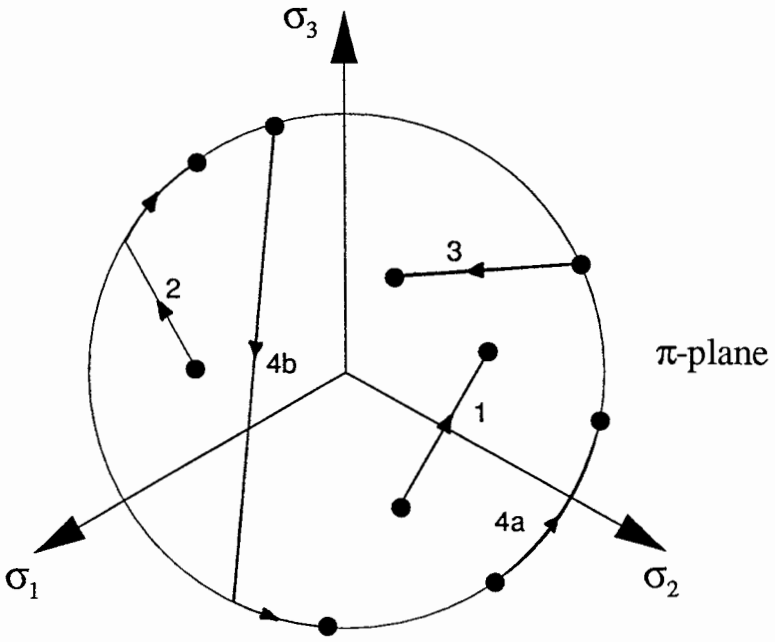

Figure 2.3: von Mises yield surface and possible cases of constitutive behaviour.

2.3.1 von Mises plasticity

For three-dimensional problems, the von Mises yield function is defined as (Calladine, 1985)

$$f(\boldsymbol{\sigma}) = (\sigma_{xx} - \sigma_{yy})^2 + (\sigma_{yy} - \sigma_{zz})^2 + (\sigma_{zz} - \sigma_{xx})^2 + 6\tau_{xy}^2 + 6\tau_{yz}^2 + 6\tau_{zx}^2 - 8c^2 \qquad (2.6)$$

where c is the shear strength of the material in triaxial compression. In the application to undrained clay, c is set to s_u, the undrained shear strength of the clay.

2.3.2 Element stiffness matrix

The technique of isoparametric mapping, where the interpolation functions defining the geometry of the element and the displacements within the element are the same, is used to formulate the element stiffness matrix. This is a well established technique which allows a straight edged element, defined in local coordinates (α, β, γ), to be mapped to a curved sided element in global coordinates (x, y, z) (Zienkiewicz, 1977). The tangent element stiffness matrix [**K**], defined in Equation (2.4), is expressed for isoparametric mapping as

$$[\mathbf{K}] = \int_V [\mathbf{B}]^T [\mathbf{D}]^{ep} [\mathbf{B}] \det[\mathbf{J}] d\alpha \, d\beta \, d\gamma \qquad (2.7)$$

where [J] is the Jacobian of the transformation from global (x, y, z) to local (α, β, γ) coordinates, the matrix [B] relates the strains ($\boldsymbol{\varepsilon}$) to the nodal displacements (U) (Equation 2.2), and $[\mathbf{D}]^{ep}$ is the element material elasto-plastic stiffness matrix. $[\mathbf{D}]^{ep}$ is defined by the constitutive model adopted and is expressed

$$[\mathbf{D}]^{ep} = [\mathbf{D}]^{e} + [\mathbf{D}]^{p} \tag{2.8}$$

where $[\mathbf{D}]^{e}$ is the element material elastic stiffness matrix and $[\mathbf{D}]^{p}$ is the element material plastic stiffness matrix. The latter can be written in the general form

$$[\mathbf{D}]^{p} = \frac{-[\mathbf{D}]^{e}\left[\frac{\partial g}{\partial \sigma}\right]\left[\frac{\partial f}{\partial \sigma}\right]^{T}[\mathbf{D}]^{e}}{\left[\frac{\partial f}{\partial \sigma}\right]^{T}[\mathbf{D}]^{e}\left[\frac{\partial g}{\partial \sigma}\right]} \tag{2.9}$$

where $f(\boldsymbol{\sigma})$ is the yield function and $g(\boldsymbol{\sigma})$ is the plastic potential. The derivation of Equation (2.9) is given by Burd (1986) and involves the assumptions that: the total strain rate can be decomposed into elastic and plastic components, the stress rate is related to the elastic strain rate, and the plastic strain rate is defined by the plastic potential $g(\boldsymbol{\sigma})$. Note that Equation (2.9) only applies when the Gauss point stress lies on the yield surface; if the stress point lies inside the yield surface, $[\mathbf{D}]^{p}$ is set to zero.

For the constitutive model adopted, the element material elastic stiffness matrix $[\mathbf{D}]^{e}$ is

$$[\mathbf{D}]^{e} = \begin{bmatrix} K+\frac{4G}{3} & K-\frac{2G}{3} & K-\frac{2G}{3} & 0 & 0 & 0 \\ K-\frac{2G}{3} & K+\frac{4G}{3} & K-\frac{2G}{3} & 0 & 0 & 0 \\ K-\frac{2G}{3} & K-\frac{2G}{3} & K+\frac{4G}{3} & 0 & 0 & 0 \\ 0 & 0 & 0 & G & 0 & 0 \\ 0 & 0 & 0 & 0 & G & 0 \\ 0 & 0 & 0 & 0 & 0 & G \end{bmatrix} \tag{2.10}$$

where G is the elastic shear modulus and K is the bulk modulus. These are related via Poisson's ratio (ν) as follows

$$K = \frac{2(1+\nu)G}{3(1-2\nu)} \tag{2.11}$$

The plastic strain rates are derived from an *associated flow* rule which assumes the plastic potential is the same as the yield function ($g(\boldsymbol{\sigma}) = f(\boldsymbol{\sigma})$) and therefore that the plastic strain component is always normal to the yield surface. Based on this assumption, the element material plastic stiffness matrix $[\mathbf{D}]^p$ (Equation 2.9) for a perfectly-plastic von Mises three-dimensional material becomes

$$[\mathbf{D}]^p = \frac{-3G}{4c^2}\begin{bmatrix} S_{xx}^2 & S_{xx}S_{yy} & S_{xx}S_{zz} & S_{xx}\tau_{xy} & S_{xx}\tau_{yz} & S_{xx}\tau_{zx} \\ S_{yy}S_{xx} & S_{yy}^2 & S_{yy}S_{zz} & S_{yy}\tau_{xy} & S_{yy}\tau_{yz} & S_{yy}\tau_{zx} \\ S_{zz}S_{xx} & S_{zz}S_{yy} & S_{zz}^2 & S_{zz}\tau_{xy} & S_{zz}\tau_{yz} & S_{zz}\tau_{zx} \\ \tau_{xy}S_{xx} & \tau_{xy}S_{yy} & \tau_{xy}S_{zz} & \tau_{xy}^2 & \tau_{xy}\tau_{yz} & \tau_{xy}\tau_{zx} \\ \tau_{yz}S_{xx} & \tau_{yz}S_{yy} & \tau_{yz}S_{zz} & \tau_{yz}\tau_{xy} & \tau_{yz}^2 & \tau_{yz}\tau_{zx} \\ \tau_{zx}S_{xx} & \tau_{zx}S_{yy} & \tau_{zx}S_{zz} & \tau_{zx}\tau_{xy} & \tau_{zx}\tau_{yz} & \tau_{zx}^2 \end{bmatrix} \tag{2.12}$$

where the notation S denotes deviatoric stresses[1].

2.3.3 Gauss Point Stress Updating

The global solution scheme adopted in this thesis (Figure 2.2) involves an equilibrium check at the end of each calculation increment. The first step in this phase of the analysis is to calculate the incremental strains $\Delta\boldsymbol{\varepsilon}$ at the Gauss points which are compatible with the incremental nodal displacements $\Delta\mathbf{U}$, using the incremental form of Equation (2.2). The next step is to update the stresses at each Gauss point by evaluating an integral of the form

$$\Delta\boldsymbol{\sigma} = \int_t^{t+\Delta t} [\mathbf{D}]^{ep}\Delta\dot{\boldsymbol{\varepsilon}}dt \tag{2.13}$$

which relates the change in stress $\Delta\boldsymbol{\sigma}$ to the incremental strain rate $\Delta\dot{\boldsymbol{\varepsilon}}$ over the time step of loading Δt. Assuming the incremental strain rates to be constant during the complete time step, closed-form solutions to Equation (2.13) exist for the constitutive model adopted, and are evaluated at a deviatoric stress and strain level. Before presenting these solutions, it is necessary to define the mean stress p, incremental volumetric strain rate $\dot{v}$, deviatoric stresses S_{xx}, S_{yy}, S_{zz}, and incremental deviatoric strain rates $\dot{e}_{xx}$, $\dot{e}_{yy}$, $\dot{e}_{zz}$, as follows

---

1 Deviatoric stresses are defined in sub-section 2.3.3.

$$p = \frac{1}{3}(\sigma_{xx} + \sigma_{yy} + \sigma_{zz}) \tag{2.14}$$

$$\dot{v} = \Delta\dot{\varepsilon}_{xx} + \Delta\dot{\varepsilon}_{yy} + \Delta\dot{\varepsilon}_{zz} \tag{2.15}$$

$$S_{xx} = \sigma_{xx} - p, S_{yy} = \sigma_{yy} - p, S_{zz} = \sigma_{zz} - p \tag{2.16}$$

$$\dot{e}_{xx} = \Delta\dot{\varepsilon}_{xx} - \frac{\dot{v}}{3}, \dot{e}_{yy} = \Delta\dot{\varepsilon}_{yy} - \frac{\dot{v}}{3}, \dot{e}_{zz} = \Delta\dot{\varepsilon}_{zz} - \frac{\dot{v}}{3} \tag{2.17}$$

The stress updating algorithm commences by assuming all stress increments to be initially elastic, regardless of the initial stress state. In all of the solutions described below, the strain rates are taken to occur during the normalised time interval $0 \le t \le 1$. Therefore the deviatoric stresses at the end of the step are calculated to be

$$S_{xx} = S_{xx_o} + t2G\dot{e}_{xx} \tag{2.18}$$

$$S_{yy} = S_{yy_o} + t2G\dot{e}_{yy} \tag{2.19}$$

$$S_{zz} = S_{zz_o} + t2G\dot{e}_{zz} \tag{2.20}$$

$$\tau_{xy} = \tau_{xy_o} + tG\dot{\gamma}_{xy} \tag{2.21}$$

$$\tau_{yz} = \tau_{yz_o} + tG\dot{\gamma}_{yz} \tag{2.22}$$

$$\tau_{zx} = \tau_{zx_o} + tG\dot{\gamma}_{zx} \tag{2.23}$$

where $t = 1$ and the subscript o denotes the stresses at the beginning of the time step. The direct stresses are then computed from the deviatoric stresses using Equations (2.14) and (2.16) noting that the mean stress at time t is

$$p = p_o + tK\dot{v} \tag{2.24}$$

where K is the elastic bulk modulus defined earlier in Equation (2.11).

The von Mises yield function (Equation 2.6) is then evaluated to determine whether the stresses at the end of the assumed elastic load step lie either inside or on the yield function ($f \le 0$), or outside the yield function ($f > 0$). Realising that the initial stress state ($t = 0$) is either elastic

(STATE = 0) and lies inside the yield function or plastic (STATE = 1) and lies on the yield function, four main cases of constitutive behaviour exist, as shown schematically in Figure 2.3. These are addressed in further detail below:

1. STATE = 0, $f \leq 0$

The calculated stresses at the end of the assumed elastic time step are correct, as the entire step was elastic.

2. STATE = 0, $f > 0$

The initially elastic Gauss point stresses have yielded at some stage during the increment of analysis. The time t at which the yield surface is intersected is evaluated by substituting Equations (2.18) to (2.23), corresponding to elastic behaviour, into the yield function of Equation (2.6) to give the following quadratic function in t.

$$f = at^2 + bt + c = 0 \tag{2.25}$$

where

$$a = G^2\{4(\dot{e}_{xx}^2 + \dot{e}_{xx}\dot{e}_{yy} + \dot{e}_{yy}^2) + \dot{\gamma}_{xy} + \dot{\gamma}_{yz} + \dot{\gamma}_{zx}\} \tag{2.26}$$

$$b = G\{4\dot{e}_{xx}S_{xx_o} + 2\dot{e}_{xx}S_{yy_o} + 2\dot{e}_{yy}S_{xx_o} + 4\dot{e}_{yy}S_{yy_o} + 2\dot{\gamma}_{xy}\tau_{xy_o} + 2\dot{\gamma}_{yz}\tau_{yz_o} + 2\dot{\gamma}_{zx}\tau_{zx_o}\} \tag{2.27}$$

$$c = S_{xx_o}^2 + S_{xx_o}S_{yy_o} + S_{yy_o}^2 + \tau_{xy_o}^2 + \tau_{yz_o}^2 + \tau_{zx_o}^2 - \frac{4}{3}s_u^2 \tag{2.28}$$

Equation (2.25) has one root for $0 \leq t < 1$. The increment is now split into two independent parts where for $0 \rightarrow t$ the Gauss point stresses are updated using the elastic solutions of Equations (2.18) to (2.23), while the remainder of the increment, $t \rightarrow 1$, corresponds to plastic behaviour. For many constitutive laws, the plastic incremental stresses are computed by numerically integrating the stress - strain rate relationship of Equation (2.13). However, for a von Mises yield criterion and assuming the strain rates to be constant for the time increment of plasticity, Krieg and Krieg (1977) derive the closed-form solution for the deviatoric stresses to be

$$S_{xx}\eta = S_{xx_o} + 2G\dot{e}_{xx}\xi \tag{2.29}$$

$$S_{yy}\eta = S_{yy_o} + 2G\dot{e}_{yy}\xi \tag{2.30}$$

$$S_{zz}\eta = S_{zz_o} + 2G\dot{e}_{zz}\xi \tag{2.31}$$

$$\tau_{xy}\eta = \tau_{xy_o} + G\dot{\gamma}_{xy}\xi \tag{2.32}$$

$$\tau_{yz}\eta = \tau_{yz_o} + G\dot{\gamma}_{yz}\xi \tag{2.33}$$

$$\tau_{zx}\eta = \tau_{zx_o} + G\dot{\gamma}_{zx}\xi \tag{2.34}$$

where

$$\eta = \cosh\left(\frac{\beta}{\alpha}t'\right) + \chi\sinh\left(\frac{\beta}{\alpha}t'\right) \tag{2.35}$$

$$\xi = \left(\frac{\alpha}{\beta}\right)\sinh\left(\frac{\beta}{\alpha}t'\right) + \left(\frac{\alpha}{\beta}\right)\chi\cosh\left(\frac{\beta}{\alpha}t'\right) - \left(\frac{\alpha}{\beta}\right)\chi \tag{2.36}$$

$$\chi = \frac{G}{\alpha\beta}\{S_{xx_o}(2\dot{e}_{xx} + \dot{e}_{yy}) + S_{yy_o}(\dot{e}_{xx} + 2\dot{e}_{yy}) + \tau_{xy_o}\dot{\gamma}_{xy} + \tau_{yz_o}\dot{\gamma}_{yz} + \tau_{zx_o}\dot{\gamma}_{zx}\} \tag{2.37}$$

$$\alpha = \frac{2s_u}{\sqrt{3}} \tag{2.38}$$

$$\beta^2 = 4G^2\left\{\dot{e}_{xx}^2 + \dot{e}_{xx}\dot{e}_{yy} + \dot{e}_{yy}^2 + \frac{1}{4}(\dot{\gamma}_{xy}^2 + \dot{\gamma}_{yz}^2 + \dot{\gamma}_{zx}^2)\right\} \tag{2.39}$$

Note that t' in Equations (2.35) and (2.36) corresponds to the remainder of the time step ($= 1 - t$). The direct stresses at the end of the load step are then computed from the deviatoric stresses using Equations (2.14) and (2.16) and noting that the volumetric behaviour is always elastic and the mean stress p is therefore given by Equation (2.24) . This category of stress updating is concluded by setting the STATE parameter to 1 to signify that the Gauss point stresses have ended the increment in a plastic state.

3. STATE = 1, $f \leq 0$

This case of stress updating involves elastic unloading from the yield surface. As the Gauss point stresses at the end of the load step lie inside the yield surface ($f \leq 0$), the entire increment is assumed to be elastic and the calculated elastic stress increments are taken to be correct. The STATE parameter is therefore set to zero.

4. STATE = 1, $f > 0$

Even though it can be confidently concluded that the Gauss point stresses commenced and ended the time step on the yield surface, two possible cases of constitutive behaviour exist as represented by stress paths 4a and 4b in Figure 2.3. The entire time step is plastic for the case of stress path 4a, while path 4b shows initially elastic unloading of the Gauss point stresses followed by subsequent reyielding. These two possibilities are distinguished by calculating the derivative of the yield function at the beginning of the time step, assuming it to be initially elastic. This amounts to computing the derivative of Equation (2.25) for $t = 0$ to give

$$\left.\frac{df}{dt}\right|_{t=0} = b \tag{2.40}$$

where b is defined in Equation (2.27). The two possible outcomes are then considered:

(a) $\left.\frac{df}{dt}\right|_{t=0} \geq 0$

A zero or positive gradient signifies that the elastic strain rate vector is directed outward from the yield surface. Therefore the entire increment is plastic and the Gauss point stresses at the end of the step are calculated using Equations (2.29) to (2.34) for $t' = 1$.

(b) $\left.\frac{df}{dt}\right|_{t=0} < 0$

A negative gradient indicates that the elastic strain rate vector is directed inwards from the yield surface, and therefore elastic unloading has taken place. The stress update calculation is performed as given in Case 3, where the increment is split into elastic ($0 \rightarrow t$) and plastic ($t \rightarrow 1$) parts.

The final part of the equilibrium check is to determine the nodal forces (**F**) which are consistent with the Gauss point stresses and therefore in equilibrium with the calculated displacements. This is simply the case of evaluating the right hand-side of Equation (2.1), which is rewritten below in its integral form.

$$\mathbf{F} = \int_V [\mathbf{B}]^T \boldsymbol{\sigma} dV \tag{2.41}$$

2.4 Selected Aspects of Computer Implementation

The three-dimensional finite element program OXFEM2, used in this research, was developed from a two-dimensional finite element program OXFEM[2], which can analyse plane strain and axisymmetric problems. All software development in this research was performed on SUN 3 workstations using the scientific language FORTRAN 77. Initial computer runs of three-dimensional problems highlighted the need for greater processing speed and accessible memory than was available. OXFEM2 was therefore mounted on a vector processing CONVEX super-computer. The CONVEX was observed to have a processing speed in the range 30-50 times greater than the SUN 3 workstations. The total central processing unit (cpu) times on the CONVEX for the single step elastic analyses presented in this thesis were in the range 30 to 60 minutes. For incremental non-linear analyses, cpu times of 10 to 20 hours were involved. Similar runs on the SUN 3 workstations would have taken excessively long.

The CONVEX has the added benefit that it accommodates programs with a large memory storage requirement, for which it has an upper limit of 100 Mb. For the analyses presented in this thesis, OXFEM2 used memory storage in the range 70 to 100 Mb. A large percentage of this space is required by an array which is used to store the Gaussian eliminated equations associated with the Frontal solution procedure (discussed below). The size of this array is directly related to the size and nature of the finite element mesh and therefore places a limit on the level of mesh refinement, and therefore the accuracy of analysis, achieved.

In the finite element method, the linear algebraic equations associated with the stiffness matrix (Equation 2.3) are sparse, and therefore can be solved considerably more efficiently using a technique which takes this sparsity into account. The Frontal solution procedure is used in this research and is thought to be as efficient computationally as alternative techniques, such as the Skyline (or profile) solver (Zienkiewicz, 1977). In the frontal method the unknowns are determined by applying straightforward Gaussian elimination. However, the complete stiffness matrix is not assembled explicitly, as the matrix assembly and elimination processes are interleaved. At a given stage of the frontal procedure, only a part of the stiffness matrix is

2 OXFEM was developed by the Oxford University Soil Mechanics Group

contained in a much smaller frontal matrix, which can be conceptualised as sweeping through the nodes of the mesh element by element. The efficiency of this scheme is dependent on the order of element numbering in the mesh. An element reordering algorithm developed by Sloan (1981) was therefore utilised in the mesh generation procedure described in Section 3.3.

A simple example demonstrating the frontal solution procedure is given by Cheung and Yeo (1979). Many variations of this procedure have been used, with added efficiency being achieved at the expense of increased complexity of code. Adopting the frontal procedure outlined by Hinton and Owen (1977), Burd (1986) developed the subroutine FRONTL. This subroutine has been developed further, as part of the development of OXFEM2, to produce two companion subroutines: FRNSTF and FRNBCK. Subroutine FRNSTF performs the same overall function as FRONTL, but has the advantage that the element stiffness matrices are computed internally as the procedure sweeps through each element of the mesh, while FRONTL requires that all element stiffness matrices be initially available in one large buffer. Subroutine FRNBCK, utilising the stored array of Gaussian eliminated equations produced from the previous run of FRNSTF, effectively performs only the back-substitution phase of the frontal solution procedure. The interaction of FRNSTF and FRNBCK is an important aspect of the global solution procedure described in Section 2.2. Further developments of subroutine FRONTL which have been incorporated into subroutines FRNSTF and FRNBCK include: (i) the ability to solve both two and three dimensional problems, (ii) symmetric and non-symmetric matrices can be considered (even though the symmetric case is only examined in this research), and (iii) a repacking algorithm has been implemented which ensures that the number of inactive columns in the frontal matrix is minimised.

Because of the large amount of computing time associated with non-linear analysis, especially for three-dimensional problems, a facility which allows a computer run to be restarted was developed in OXFEM2. This facility has proven particularly important for the CONVEX batch system which only allows a maximum of 2 hours cpu time per job. It functions by writing a file to disk at the end of every load step (or as the user may specify), which effectively contains all stress, strain, force and displacement information. The restart file facility allows the continuation of a given run of analysis, or the commencement of a new run using the end stress state of a previous run.

CHAPTER 3 CHOICE OF THREE DIMENSIONAL FINITE ELEMENT

3.1 Introduction

The geometry of elements that have been adopted in previous three-dimensional finite element analyses can be placed into two main groups: rectangular prisms (to be referred to as cubes) and tetrahedra. Other simple three-dimensional elements, such as triangular prisms, have been used in certain applications (Zienkiewicz, 1977), but are not considered here. Cubic elements can be divided into a further two classes: Lagrangian and Serendipity elements.

The first four elements of the Lagrangian cube family, ranging from the 8-node cube to the 125-node cube, are shown in Figure 3.1. Excluding the 8-node cube, this family of elements is characterised by the element having face and interior nodes arranged in a regular grid-like fashion. Each element is defined by the parameter N, the order to which the polynomial interpolation displacement function is complete. For example, the displacement function for the 8-node cube is complete to order one ($N = 1$). Furthermore, the number of nodes per element, and therefore number of polynomial displacement terms in the shape functions, is $(N + 1)^3$.

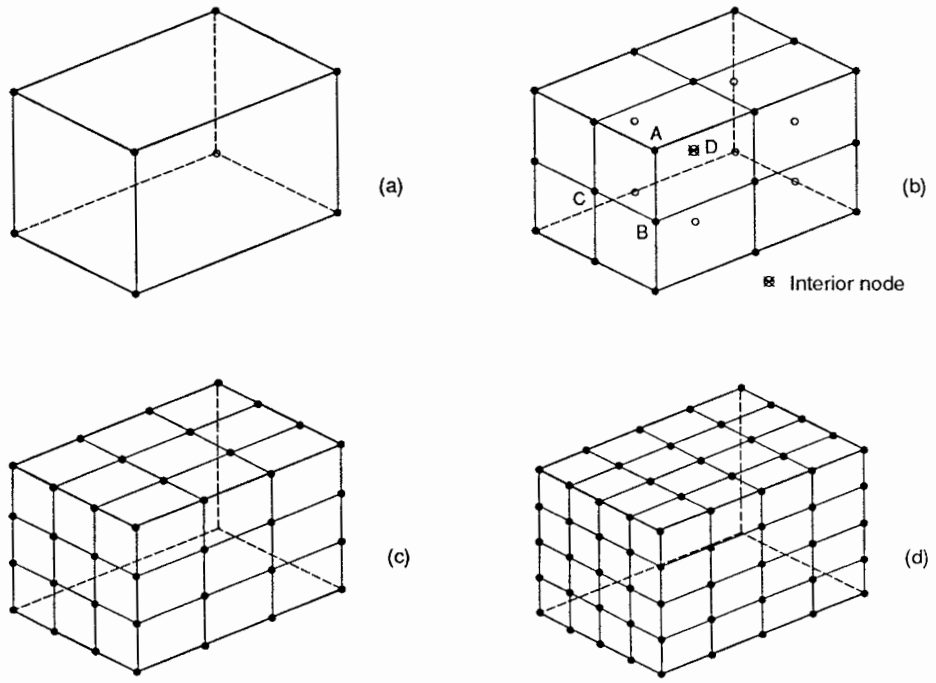

Figure 3.1: Lagrangian cube family: (a) 8-node cube, (b) 27-node cube, (c) 64-node cube*, (d) 125-node cube*; (* - visible nodes are only shown on immediate faces).

Figure 3.2 presents the first three elements of the Serendipity cube family. The lower order elements of this family are generally characterised as having only edge and corner nodes. Extension to the fourth element of this family ($N = 4$) is not straightforward as it appears that 3 face and/or interior nodes need to be introduced to achieve a shape (displacement) function that is complete to order 4. Unfortunately this distribution of nodes cannot be achieved symmetrically. Note that the 8-node cube is equivalent to the 8-node Lagrangian cubic element.

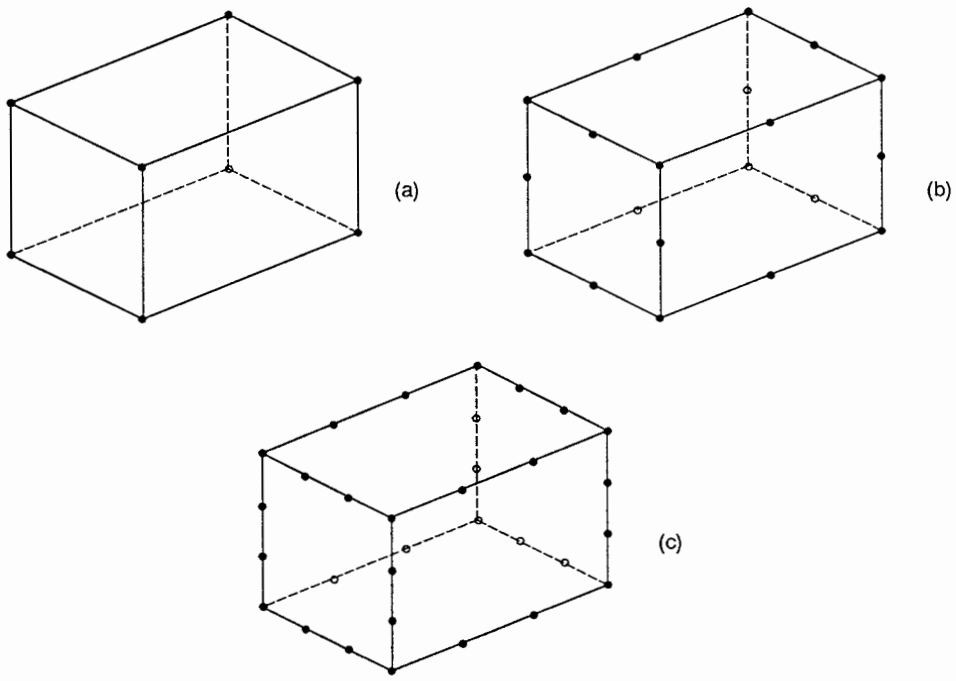

Figure 3.2: Serendipity cube family: (a) 8-node cube, (b) 20-node cube, (c) 32-node cube.

The first four elements of the tetrahedron family are shown in Figure 3.3. Tetrahedral elements have the unique characteristic that the shape function describing the nodal displacements is "complete" to order N, that is, no additional polynomial terms exist. This property of the tetrahedron family makes it very favourable for finite element analysis, since all polynomial terms are contributing to the accuracy of the computation. A major limitation of the tetrahedron, however, is mesh generation and visualisation in three dimensions. This can be largely overcome by adopting a regular cubic arrangement of elements, where a cube is divided into either 5 tetrahedra, as shown in Figure 3.4a, or 6 tetrahedra, as given in Figure 3.4b (Zienkiewicz, 1977). The 6 tetrahedra per cube arrangement is simply the addition of two triangular prisms which are themselves divided into 3 tetrahedra (Figure 3.4c).

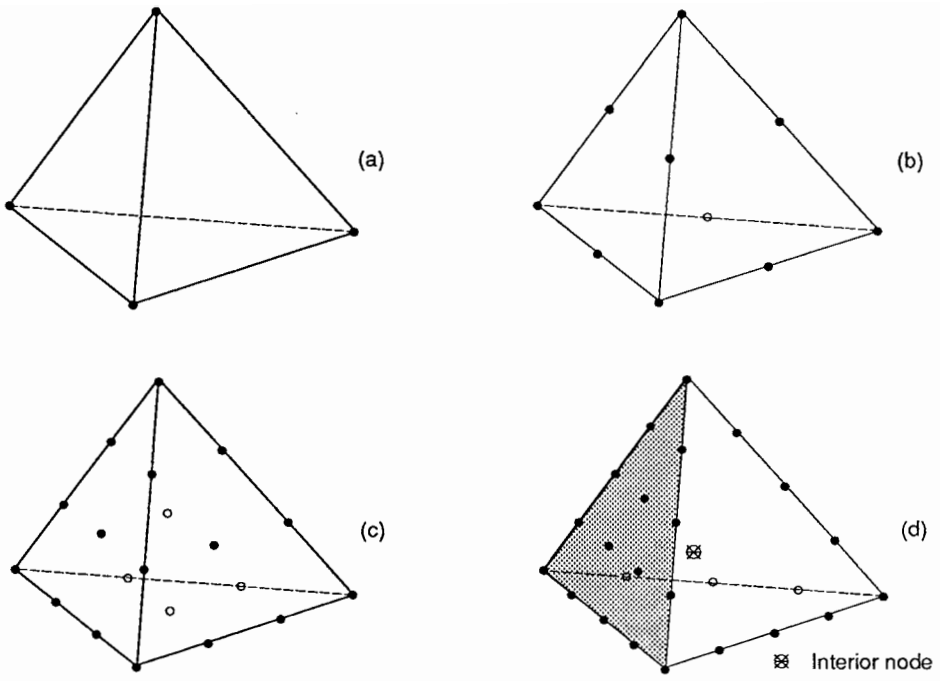

Figure 3.3: Tetrahedron family: (a) 4-node constant strain tetrahedron, (b) 10-node linear strain tetrahedron, (c) 20-node quadratic strain tetrahedron, (d) 35-node cubic strain tetrahedron*; (* - face nodes are only shown on shaded face).

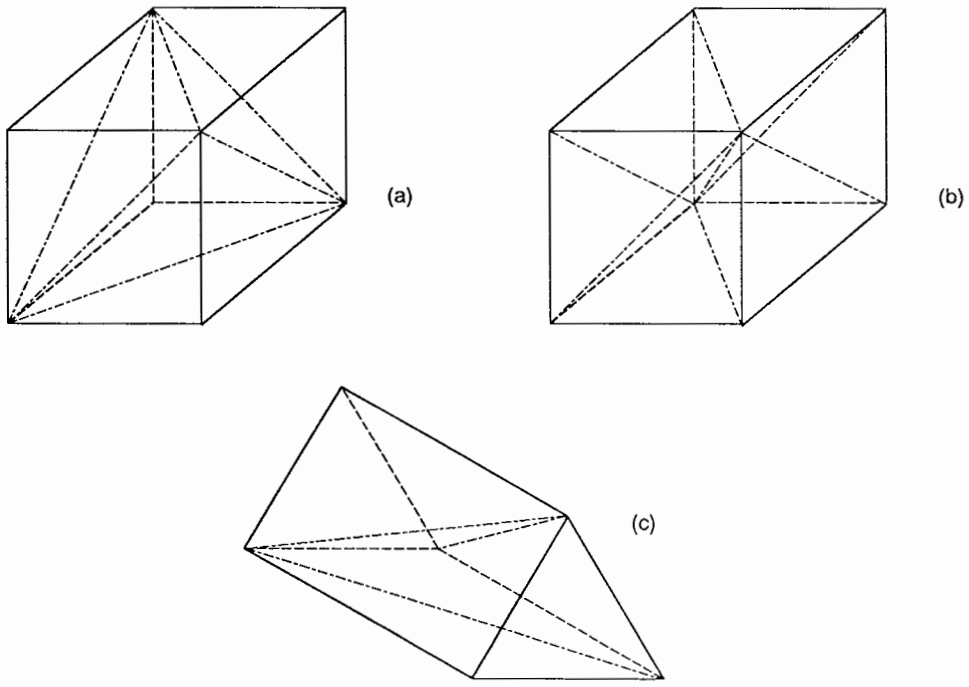

Figure 3.4: Tetrahedra arrangements: (a) 5 tetrahedra per cube, (b) 6 tetrahedra per cube, (c) 3 tetrahedra per triangular prism.

In choosing a finite element, the main considerations are the element's ability to model accurately the problem under examination, and the computational effort required to achieve this objective, the latter being particularly important in three-dimensional analyses. Many of the analyses performed in this research embrace materials that are, or become, incompressible. Using the displacement finite element method, this incompressibility proves a major limitation to the accuracy of the analysis, as an over-stiff response has been observed in many cases. The inaccuracy of the load-displacement curve is a result of the incompressibility condition imposing additional kinematic constraints on the nodal displacements, thereby reducing the available "free" degrees-of-freedom in the finite element mesh. This phenomenon has been observed in elastic-plastic problems where incompressibility applies in the fully plastic region (Nagtegaal *et al*, 1974; Sloan and Randolph, 1982; de Borst and Vermeer, 1984) or elastic problems where incompressibility is enforced pointwise throughout the continuum as Poisson's ratio approaches a value of 0.5 (Sloan and Randolph, 1982; Burd and Houlsby, 1990).

The following section addresses the issue of three-dimensional finite element suitability for incompressible material analysis. The section clearly demonstrates that some elements are better suited than others, while some elements are totally unsuitable. In this context, the important issue of computational efficiency is also considered.

3.2 Suitability of Three Dimensional Finite Elements for Modelling Material Incompressibility

3.2.1 Background

Nagtegaal *et al* (1974), in their pioneering work in this area, proposed a criterion for determining the suitability of a particular finite element for incompressible material analysis. They evaluate the ratio of the total number of degrees-of-freedom (equal to the number of nodes multiplied by the number of degrees-of-freedom per node) to the total number of constraints (the number of elements multiplied by the number of incompressibility constraints per element). This ratio is evaluated in the limit as the mesh is refined, assuming a special arrangement of elements is not employed[1]. If this ratio is greater than one, the finite element is suitable for material

1 Special arrangements of elements are discussed in sub-section 3.2.6.

incompressibility analysis. Similarly, if the ratio is less than one, the finite element is unsuitable. However, there is some conjecture about the suitability of finite elements when the ratio is equal to one, and this important issue is addressed in this section.

With the acknowledgement that certain finite elements yield inaccurate results in analyses where the material is (or becomes) incompressible, much effort has been given to developing special finite element formulations in which the detrimental effect of incompressibility is reduced. A concise summary of the many formulations developed is provided by Burd and Houlsby (1990). The methods include techniques such as uniform reduced integration, reduced selective integration, and mixed finite element formulations. Each method has advantages and disadvantages and no single technique has emerged as a clear first choice. A philosophy different from many of those developed was introduced by Sloan and Randolph (1982). They demonstrated that as the order of the polynomial defining the displacements within an element is increased, the increase of new degrees-of-freedom is greater than the increase in the incompressibility constraints. Therefore, if a particular type of finite element has a ratio of degrees-of-freedom to constraints of less than one, then an element suitable for incompressibility analysis may be found by progressing to a higher order element of the same family.

This section documents and compares the suitability of the three-dimensional finite element families, introduced in Section 3.1, for the analysis of incompressible materials using the displacement finite element method. The assessment of element suitability is initially performed using the ratio of degrees-of-freedom to incompressibility constraints, as described by Nagtegaal *et al* (1974). However, to facilitate a more quantitative understanding of the problem and develop a comparative measure of performance applicable to finite elements of different type and order, two new parameters are introduced. These are evaluated for the two-dimensional elements previously examined by Sloan and Randolph (1982), to help support the concepts introduced, and for the three-dimensional elements under consideration. The important consideration of computational effort is then introduced into the comparison of the finite elements examined. Two three-dimensional numerical experiments are then reported and compared with a similar two-dimensional study of Sloan (1981). These help to clarify and substantiate the findings of this section.

3.2.2 The ratio of degrees-of-freedom to incompressibility constraints

Sloan and Randolph (1982), following the work of Nagtegaal *et al* (1974), demonstrated that the ratio of total number of degrees-of-freedom to total number of constraints, in the limit as the mesh is uniformly refined, can be evaluated at an element level. That is

$$\frac{\text{degrees-of-freedom}}{\text{constraints}} = \frac{\text{degrees-of-freedom per element}}{\text{constraints per element}} \tag{3.1}$$

For a two dimensional finite element mesh, the ratio of number of nodes (n) to number of elements (e) in the limit as the mesh is uniformly refined is (Nagtegaal *et al*, 1974; Sloan and Randolph, 1982)

$$n_e^* = \lim_{n \to \infty} \left(\frac{n}{e} \right) = \frac{m}{2} \tag{3.2}$$

where m is the sum of the internal nodal (planar) angles divided by π. The asterisk (*) notation adopted throughout this section refers to the limit as the mesh is uniformly refined ($n \to \infty$), and the subscript e represents the division by the number of elements. Noting there are two degrees-of-freedom per node, Equation (3.2) can be written as

$$d_e^* = \lim_{n \to \infty} \left(\frac{d}{e} \right) = m \tag{3.3}$$

where the number of degrees-of-freedom per element (d_e^*) is directly related to the sum of the internal nodal angles represented by m. The proof of this relationship will not be repeated here, but its extension to three-dimensional problems is as follows.

Consider a regular 27-node Lagrangian cubic element as shown in Figure 3.1b. This element consists of 8 corner nodes, 12 edge nodes, 6 face nodes and 1 interior node. In direct analogy to planar angles, the "volumetric" internal angles of these nodes (measured in steradians) are $\pi/2$ (corner node A), π(edge node B), 2π (face node C) and 4π (interior node D), respectively[2]. The sum of the internal volumetric nodal angles is therefore 32π. For any general three dimensional finite element, the sum of the internal volumetric nodal angles can be written as

2 Nodes A, B, C, and D are shown in Figure 3.1b

$$\sum_{i=1}^{l} \theta_i = m\pi \tag{3.4}$$

where l is the number of nodes per element and m varies with element type (and the configuration of the elements, as will be shown later). For a regular mesh of e elements, it therefore follows that the sum of the mesh internal nodal volumetric angles is

$$\sum_{j=1}^{e} \sum_{i=1}^{l} \theta_i^j = em\pi \tag{3.5}$$

An alternative way of summing the internal nodal angles of the mesh is to consider the nodes alone without any reference to elements. For the purpose of simplicity, let us assume that the mesh is a rectangular prism with n nodes consisting of 8 corner nodes, r edge nodes, s face nodes and k interior nodes. Noting the internal volumetric nodal angles for the 27-node Lagrangian cube discussed earlier, it follows that

$$\sum_{j=1}^{e} \sum_{i=1}^{l} \theta_i^j = (4+r+2s+4k)\pi \tag{3.6}$$

Equating (3.5) and (3.6) and rearranging gives

$$\frac{e}{k} = \frac{4}{m} + \frac{(4+r+2s)}{mk} \tag{3.7}$$

Upon uniform refinement of the mesh, k will increase at a greater rate than the number of boundary nodes $(8+r+s)$ and therefore will tend to the total number of nodes (n). In this limit, the second term on the right side of (3.7) becomes small and the ratio of number of nodes to number of elements becomes

$$n_e^* = \lim_{k \to \infty} \left(\frac{k}{e} \right) = \frac{m}{4} \tag{3.8}$$

Rewriting this in terms of degrees-of-freedom per element (d_e^*) for a three-dimensional mesh gives

$$d_e^* = \lim_{n \to \infty} \left(\frac{d}{e} \right) = \frac{3}{4}m \tag{3.9}$$

Hence, in the limiting case of a uniformly refined mesh, the degrees-of-freedom per element for a three-dimensional finite element is three-quarters the sum of the element internal nodal volumetric angles divided by π. For a mesh with any given external boundary configuration, the number of interior nodes (k) will always tend to the total number of nodes (n), in the limiting case of a uniformly refined mesh. And Equations (3.8) and (3.9) will similarly result, independent of the rectangular prismatic mesh adopted in the above formulation.

Unlike the two-dimensional case, where the value of m is constant for a given element arranged randomly in a mesh, for three-dimensional elements m is dependent on the arrangement of the elements since the sum of the internal volumetric angles of a polyhedron is not constant (Nagtegaal *et al*, 1974). Therefore the degrees-of-freedom per element for three-dimensional finite elements is dependent on the arrangement of the elements adopted. All three-dimensional element configurations examined in this section are assumed to be of a regular (orthogonal) cubic arrangement.

The procedure for evaluating the number of constraints per element (c_e) for plane strain and axisymmetric two dimensional conditions has been well documented by Nagtegaal *et al* (1974) and Sloan and Randolph (1982). Extension to three dimensional problems is straightforward, as briefly summarised below.

Under incompressible conditions the element is required to deform so that the volumetric strain rate $\dot{\varepsilon}_{kk} = 0$. For a three dimensional problem, this condition may be written

$$\dot{\varepsilon}_{xx} + \dot{\varepsilon}_{yy} + \dot{\varepsilon}_{zz} = \frac{\partial \dot{u}}{\partial x} + \frac{\partial \dot{v}}{\partial y} + \frac{\partial \dot{w}}{\partial z} = 0 \qquad (3.10)$$

where $\dot{u}$, $\dot{v}$ and $\dot{w}$ denote velocities in the x, y and z directions, respectively. Within each finite element these can be expressed in the vector form

$$\dot{\mathbf{u}} = \begin{Bmatrix} \dot{u} \\ \dot{v} \\ \dot{w} \end{Bmatrix} = \mathbf{a} + \mathbf{b}x + \mathbf{c}y + \mathbf{d}z + \ldots \qquad (3.11)$$

where the vectors **a**, **b**, **c**, **d**, .., are expressed in terms of the nodal velocities and coordinates. Substituting Equation (3.11) into (3.10) yields an equation in terms of the coefficients of the **a**,

b, **c**, **d**, .. vectors. Assuming "exact" integration is to be used in the stiffness formulation of the element, the number of constraints for the element (c_e) is taken to be equal to the number of coefficients (or combinations of coefficients) which are constrained to be zero in the resulting equation.

As addressed by Sloan and Randolph (1982), it is usual in finite elements to evaluate the element stiffness formulations at a discrete number of integration points. For a given straight-sided element, there is a particular number and positioning of the integration points such that the element stiffness is determined exactly. This is termed exact integration (Laursen and Gellert, 1978). The incompressibility constraints imposed on an element vary with the number of integration points. The approach of reducing the number of constraints by reducing the number of integration points and thereby improving the suitability of a particular element for incompressibility analysis has been widely used and is called "reduced integration" (Zienkiewicz, 1977). However, it has been shown that under certain conditions this inexact method may be unacceptably inaccurate (de Borst and Vermeer, 1984; de Borst, 1982). All analyses presented in this thesis use the exact integration approach and therefore the following considerations are limited to this case.

Prior to examining the suitability of three-dimensional finite elements for incompressible analysis based on the analyses described previously, it is appropriate to rewrite Equation (3.1) in terms of the notation adopted in this sub-section

$$d_c^* = \frac{d_e^*}{c_e} \tag{3.12}$$

where d_c^* is the ratio of the degrees-of-freedom to constraints in the limit of a uniformly refined mesh.

Lagrangian cube family

Table 3.1 demonstrates the suitability of the Lagrangian cubic elements (Figure 3.1) for incompressible material analysis using the displacement finite element method. The first two elements of this family, the 8-node and 27-node cubes, are shown to be unsuitable since their ratios of degrees-of-freedom to constraints (d_c^*) are less than one. However, d_c^* is seen to increase with the order of the polynomial displacement function (N), this result being consistent with

the findings of Sloan and Randolph (1982) for two-dimensional finite elements. Subsequent higher order elements to the 27-node cube have a d_c^* value greater than one, and are therefore classified as suitable.

Table 3.1: Suitability of Lagrangian cubic elements for incompressible material analysis

Element[1] type	N [2]	Degrees-of-freedom per element (d_e^*)	Constraints[3] per element (c_e)	Degrees-of-freedom per constraint ($d_c^* = d_e^*/c_e$)	Suitable	Free degrees-of-freedom per element (f_e^*)	Free degrees-of-freedom per node (f_n^*)
8-node cube	1	3	7	0.43	No	-4	-4.00
27-node cube	2	24	26	0.92	No	-2	-0.25
64-node cube	3	81	63	1.29	Yes	18	0.67
125-node cube	4	192	124	1.55	Yes	68	1.06

Notes:
1. Refer to Figure 3.1 for schematic diagrams of Lagrangian cubic elements.
2. Order of "complete" polynomial displacement function.
3. Based on assumption of exact integration of a straight-sided element.
4. * represents the limiting case of a uniformly refined mesh.

Closer examination of Table 3.1 reveals that a relationship exists between the order to which the shape function is complete (N) and the degrees-of-freedom per element (d_e^*) and constraints per element (c_e). These are as follows

$$d_e^* = 3N^3 \tag{3.13}$$

$$c_e = (N+1)^3 - 1 \tag{3.14}$$

Equations (3.13) and (3.14) combined with Equation (3.12) can be used to extend Table 3.1 to any higher order Lagrangian cubic element so desired.

Serendipity cube family

The suitability for accurate incompressible material analysis of the first three elements of the Serendipity cube family, schematically presented in Figure 3.2, is presented in Table 3.2. All

three elements have values of d_c^* of less than one and are therefore classified as unsuitable. These results are consistent with the findings of Nagtegaal *et al* (1974) who examined the suitability of the first two elements of this family.

Table 3.2: Suitability of Serendipity cubic elements for incompressible material analysis

Element[1] type	N [2]	Degrees-of-freedom per element (d_e^*)	Constraints[3] per element (c_e)	Degrees-of-freedom per constraint ($d_c^* = d_e^*/c_e$)	Suitable	Free degrees-of-freedom per element (f_e^*)	Free degrees-of-freedom per node (f_n^*)
8-node cube	1	3	7	0.43	No	-4	-4.00
20-node cube	2	17	12	0.71	No	-5	-1.25
32-node cube	3	29	21	0.72	No	-8	-1.14

Notes:
1. Refer to Figure 3.2 for schematic diagrams of Serendipity cubic elements.
2. Order of "complete" polynomial displacement function.
3. Based on assumption of exact integration of a straight-sided element.
4. * represents the limiting case of a uniformly refined mesh.

Tetrahedron family

Table 3.3 demonstrates the suitability for incompressibility analysis of the first four elements of the tetrahedron family (Figure 3.3) when arranged in a regular cubic type lattice. As stated earlier, for three dimensional problems the ratio of degrees-of-freedom to elements in the limit of a uniformly refined mesh is dependent on the configuration of the elements. Therefore, because a cube can be divided into either 5 or 6 tetrahedra per cube (Figures 3.4a and 3.4b, respectively), both cases are considered in Table 3.3. The results for the 6 tetrahedra per cube arrangement are also applicable to a triangular prism divided into 3 tetrahedra (Figure 3.4c), since the former (Figure 3.4b) is simply the addition of two of the latter.

Table 3.3: Suitability of tetrahedral elements for incompressible material analysis

			5 tetrahedra per cube arrangement					6 tetrahedra per cube arrangement				
Tetrahedron[1] element type	N [2]	Constraints[3] per element (c_e)	Degrees-of-freedom per element (d_e^*)	Degrees-of-freedom per constraint ($d_c^* = d_e^*/c_e$)	Suitable	Free degrees-of freedom per element (f_e^*)	Free degrees-of freedom per node (f_n^*)	Degrees-of-freedom per element (d_e^*)	Degrees-of-freedom per constraint ($d_c^* = d_e^*/c_e$)	Suitable[4]	Free degrees-of freedom per element (f_e^*)	Free degrees-of freedom per node (f_n^*)
Constant strain	1	1	0.6	0.60	No	-0.4	-2.00	0.5	0.5	No	-0.5	-3.0
Linear strain	2	4	4.2	1.05	Yes	0.2	0.14	4.0	1.0	#	0.0	0.0
Quadratic strain	3	10	13.8	1.38	Yes	3.8	0.83	13.5	1.35	Yes	3.5	0.78
Cubic strain	4	20	32.4	1.62	Yes	12.4	1.15	32.0	1.60	Yes	12.0	1.12

Notes:

1. Refer to Figure 3.3 for schematic diagrams of tetrahedral elements.
2. Order of "complete" polynomial displacement function.
3. Based on assumption of exact integration of a straight-sided element.
4. # on the border-line of suitability. Considered suitable for a refined mesh with the number of unrestrained degrees-of-freedom exceeding the number of incompressibility constraints.
5. * represents the limiting case of a uniformly refined mesh.

The 4-node constant strain tetrahedron has values of d_c^* of less than one for both 5 and 6 tetrahedra per cube configurations and is therefore unsuitable for incompressibility analysis. However, the linear strain tetrahedron is suitable when placed in a 5 tetrahedra per cube arrangement ($d_c^* = 1.05$) and is on the borderline of suitability for the 6 tetrahedra per cube arrangement ($d_c^* = 1$)[3]. For the 5 tetrahedra arrangement, the results for the constant and linear strain tetrahedra are consistent with the findings of Nagtegaal *et al* (1974). The higher order tetrahedral elements in Table 3.3 have values of d_c^* well above one for both configurations and are therefore suitable.

As for the Lagrangian cube family, relationships exist between N and the degrees-of-freedom per element and constraints per element. These can be used to extend Table 3.3 to higher order elements. The relationship for the constraints per element (c_e) is

$$c_e = \frac{N(N+1)(N+2)}{6} \tag{3.15}$$

The relationships for the 5 and 6 tetrahedra cube arrangements between N and the degrees-of-freedom per element (d_e^*) are (noting that a unique relationship for the 5 tetrahedra per cube arrangement only exists for those elements of order 4 or higher)

5 tetrahedra per cube:

$$d_e^* = \frac{1}{10}N(5N^2+1) \quad \text{for} \quad N \geq 4 \tag{3.16}$$

6 tetrahedra per cube:

$$d_e^* = \frac{1}{2}N^3 \tag{3.17}$$

3.2.3 The comparative performance of finite elements in terms of free degrees-of-freedom

While considering the ratio of degrees-of-freedom to constraints d_c^*, in the limit as the mesh is uniformly refined, provides a qualitative measure of the suitability of an element, it does not provide a rigourous quantitative measure of element suitability. A more meaningful approach to the problem is to consider the *free* degrees-of-freedom per element (f_e^*), defined as

$$f_e^* = d_e^* - c_e \tag{3.18}$$

---

3 A discussion on the suitability of elements when $d_c^* = 1$ is given in sub-section 3.2.6.

This new parameter defines the number of free degrees-of-freedom introduced by each element after the constraints imposed by the incompressibility condition are taken into account. There is of course a direct relationship between f_e^* and d_c^*. An element is taken to be suitable for the analysis of an incompressible material when f_e^* is greater than zero since each element then introduces free degrees-of-freedom to the problem, and so allows an accurate prediction of the load-displacement curve to be approached. Similarly if f_e^* is less than zero, the element is unsuitable since no free degrees-of-freedom are introduced and the mesh is over-constrained. Based on the definition of f_e^*, one would also expect an element to be unsuitable when f_e^* is equal to zero. That is, if one considers a sub-region of the mesh away from the boundaries, then the available degrees-of-freedom will be governed solely by the parameter f_e^*.

However, $f_e^* = 0$ is equivalent to the parameter $d_c^* = 1$, which Sloan and Randolph (1982) interpret as corresponding to a suitable element. They base this interpretation on their examination of two-dimensional mesh suitability when incompressibility is enforced throughout the mesh. They present an inequality which specifies the required number of unrestrained boundary degrees-of-freedom, such that the total number of degrees-of-freedom will exceed the total number of boundary and incompressibility constraints. Based on this criterion for mesh suitability, they show that an element with $d_c^* = 1$ is suitable if the number of *unrestrained* mesh boundary degrees-of-freedom exceeds the number of *restrained* boundary degrees-of-freedom. They support their argument by presenting accurate finite element collapse load results for a smooth rigid strip footing (in plane strain) using the 8-node and 12-node quadrilateral elements, which have a value of $d_c^* = 1$. The discrepancy between the *free* degrees-of-freedom philosophy and that postulated and observed by Sloan and Randolph (1982) is addressed later in the discussion of sub-section 3.2.6.

While f_e^* does help to quantify the suitability of an element, it does not allow comparison between different element types since the number of elements in a mesh with a given number of nodes will vary with element type. For the purpose of comparison it is better to normalise the number of free degrees-of-freedom with respect to the number of nodes, rather than the number of elements. This introduces the new parameter of free degrees-of-freedom per node (f_n^*) which takes into account the number of nodes per element (n_e^*) in the limit of a uniformly refined mesh:

$$f_n^* = \frac{\lim_{n\to\infty}\left(\frac{f}{e}\right)}{\lim_{n\to\infty}\left(\frac{n}{e}\right)} = \frac{f_e^*}{n_e^*} = \frac{d_e^* - c_e}{n_e^*} \tag{3.19}$$

Two-dimensional finite elements

For the two-dimensional problem, substituting Equation (3.3) into Equation (3.18) gives the number of free degrees-of-freedom per element

$$f_e^* = m - c_e \tag{3.20}$$

and substituting Equations (3.2) and (3.3) into Equation (3.19) gives the number of free degrees-of-freedom per node

$$f_n^* = 2 - 2\frac{c_e}{d_e^*} = 2 - 2\frac{c_e}{m} \tag{3.21}$$

Table 1 in Sloan and Randolph (1982), which examines the suitability of the two-dimensional triangular and Serendipity quadrilateral finite elements for plane strain and axisymmetric conditions, is repeated in Table 3.4. The parameters f_e^* and f_n^* introduced in this section are included in the table. For plane strain conditions, the linear, quadratic and cubic strain triangular elements and the 17-node quadrilateral element are shown to introduce free degrees-of-freedom under incompressibility conditions and are therefore suitable. The constant strain triangle and the 8-node and 12-node quadrilateral elements have values of $f_e^* = 0$ and therefore are on the border-line of suitability. For axisymmetric conditions, Table 3.4 shows the lowest order suitable element to be the cubic strain triangle[4], this being consistent with the findings of Sloan and Randolph (1982).

4 An alternative approach to the problem has been developed by Yu (1990). By employing a *modified* displacement interpolation function, he showed the 6-node triangular element satisfies the axisymmetric incompressibility condition. This formulation stems from the fact that the *standard* 6-node linear strain triangle is suitable under plane strain conditions (Table 3.4).

Table 3.4: Suitability of triangular and Serendipity quadrilateral elements for incompressible material analysis

		Plane strain					Axisymmetry				
Element type	Degrees-of-freedom per element (d_e^*)[1]	Constraints per element (c_e)[1,2]	Degrees-of-freedom per constraint ($d_c^* = d_e^*/c_e$)	Free degrees-of freedom per element (f_e^*)	Free degrees-of freedom per node (f_n^*)	Suitable[3]	Constraints per element (c_e)[1,2]	Degrees-of-freedom per constraint ($d_c^* = d_e^*/c_e$)	Free degrees-of freedom per element (f_e^*)	Free degrees-of freedom per node (f_n^*)	Suitable
Constant strain triangle	1	1	1	0	0	#	3	$\frac{1}{3}$	-2	-4	No
Linear strain triangle	4	3	$\frac{4}{3}$	1	$\frac{1}{2}$	Yes	6	$\frac{2}{3}$	-2	-1	No
Quadratic strain triangle	9	6	$\frac{3}{2}$	3	$\frac{2}{3}$	Yes	10	$\frac{9}{10}$	-1	$-\frac{2}{9}$	No
Cubic strain triangle	16	10	$\frac{8}{5}$	6	$\frac{3}{4}$	Yes	15	$\frac{16}{15}$	1	$\frac{1}{8}$	Yes
4-node quadrilateral	2	3	$\frac{2}{3}$	-1	-1	No	5	$\frac{2}{5}$	-3	-3	No
8-node quadrilateral	6	6	1	0	0	#	9	$\frac{2}{3}$	-3	-1	No
12-node quadrilateral	10	10	1	0	0	#	13	$\frac{10}{13}$	-3	$-\frac{3}{5}$	No
17-node quadrilateral	16	14	$\frac{8}{7}$	2	$\frac{1}{4}$	Yes	19	$\frac{16}{19}$	-3	$-\frac{3}{8}$	No

Notes

1. Data after Sloan and Randolph (1982)
2. Based on assumption of exact integration of a straight-sided element.
3. # on the border-line of suitability. Considered suitable for a refined mesh with the number of unrestrained degrees-of-freedom exceeding the number of incompressibility constraints.
4. * represents the limiting case of a uniformly refined mesh.

The free degrees-of-freedom per node parameter f_n^*, defined in Equation (3.19) and given in Table 3.4, can be used to compare the performance of different suitable finite elements. The comparison can be made in the following way for meshes of different element type and/or order. Consider the ratio of the number of mesh nodes such that the same number of free degrees-of-freedom are introduced. It is expected that this will lead to calculations of similar accuracy. For example from Table 3.4, a 17-node quadrilateral mesh ($f_n^* = 1/4$) would require twice as many nodes as a linear strain triangle mesh ($f_n^* = 1/2$) to give approximately the same accuracy. This discussion, however, is limited in that the parameter f_n^* does not take into consideration the computational effort involved for different element types and meshes of different sizes (numbers of nodes). This important detail is addressed in sub-section 3.2.4.

Three-dimensional finite elements

For the three-dimensional problem, substituting Equation (3.9) into Equation (3.18) gives the number of free degrees-of-freedom per element

$$f_e^* = \frac{3}{4}m - c_e \tag{3.22}$$

Substituting Equations (3.8) and (3.9) into Equation (3.19) gives the number of free degrees-of-freedom per node

$$f_n^* = 3 - 3\frac{c_e}{d_e^*} = 3 - 4\frac{c_e}{m} \tag{3.23}$$

The parameters from Equations (3.22) and (3.23) are included in Tables 3.1 to 3.3 for the Lagrangian cubic, Serendipity cubic and tetrahedral elements, respectively. It is interesting to note in Table 3.3 that for the quadratic and cubic tetrahedral elements, f_n^* values for the 5 and 6 tetrahedra per cube arrangements are within 5 % of each other, signifying that there is no great difference in performance and accuracy for calculations using either of the two arrangements. The corresponding 64-node and 125-node Lagrangian cubic elements, which are suitable for incompressibility analysis, have values of f_n^* in the range 10 to 20 % less than the tetrahedral elements.

Equations (3.22) and (3.23) can be generalised for the Lagrangian cube family and tetrahedron family in terms of the parameter N, the order to which the polynomial interpolation displacement function is complete, by substituting the relevant relationships introduced in sub-section 3.2.2. Further discussion on this aspect is provided by Bell *et al* (1991a).

3.2.4 Consideration of computational effort

A major factor in the application of finite elements in two-dimensional and especially three-dimensional problems is the consideration of computational effort. The free degrees-of-freedom per node parameter (f_n^*) developed in this thesis, does not, however, take this into account. So, while progressing to higher order elements provides greater values of f_n^* (Tables 3.1 to 3.4), this gain may be offset by a computational effort which increases at a greater rate. Hence a compromise is required between the number of free degrees-of-freedom introduced per node and the computational effort involved for that node. This can be quantitatively determined using a further new parameter "*free* degrees-of-freedom per computational effort" (f_b^*) defined as

$$f_b^* = \frac{f_n^*}{b_n} \tag{3.24}$$

where f_n^* is the free degrees-of-freedom per node defined in Equation (3.19) and b_n is a measure of the "computational effort per node". The parameter b_n is dependent on element type and increases with element order (N).

In choosing a finite element for incompressibility analysis, f_b^* is a direct measure of the computational performance of a given finite element. However, it is difficult to generalise f_b^* for a particular element since b_n is strongly dependent on the type of finite element analysis performed (Cook, 1981). The type of analysis can vary from linear static to non-linear dynamic problems with non-linear analysis involving a wide range of solution techniques (Mondkar and Powell, 1978; Sloan, 1981). The following discussion for three-dimensional problems is therefore limited to a more qualitative examination of f_b^*. A similar discussion for two-dimensional elements is given in Bell *et al* (1991a).

It is generally accepted that Lagrangian cubic three-dimensional elements are computationally inefficient due to the large number of internal nodes and the incompleteness of the polynomial interpolation functions (Zienkiewicz, 1977), and the Serendipity cube elements are generally used in preference. However, this section has established that the Serendipity cube is unsuitable for incompressible material analysis. It would therefore appear that the Tetrahedron family of elements is clearly the most computationally efficient for incompressible material analysis. For the three-dimensional finite element model adopted in this research, the parameter describing the free degrees-of-freedom per computational effort (f_b^*) is probably at a maximum somewhere in the range of the 20-node quadratic strain tetrahedron and the 35-node cubic strain tetrahedron. However, it must be emphasised that these considerations are dependent on the type of analysis performed, and for non-linear analysis, the solution scheme adopted.

3.2.5 Numerical comparison of 10-node and 20-node tetrahedra

To substantiate some of the findings of the previous sections, this section presents the results of two numerical experiments comparing the performance of the 10-node linear strain tetrahedron and 20-node quadratic strain tetrahedron. For the 6 tetrahedra per cube arrangement adopted in these experiments, the 10-node tetrahedron is on the border-line of suitability ($f_n^* = 0.0$), while the 20-node tetrahedron is expected to be suitable ($f_n^* = 0.78$). As is applicable to offshore foundations, the first experiment involved the analysis of a smooth rigid circular footing, vertically loaded at the surface of a semi-infinite elastic half-space. The exact analytical solution to this set of boundary conditions is given by Poulos and Davis (1974) to be

$$u_V = \left[\frac{1-\nu}{4GR}\right] V \tag{3.25}$$

where u_V and V are the vertical displacement and load respectively, G and ν are the elastic shear modulus and Poisson's ratio of the half-space, and R is the radius of the circular footing. To investigate the effects of incompressibility, a series of elastic finite element analyses were performed for ν ranging from 0.4 to 0.49999. The errors associated with the linear strain and quadratic strain tetrahedra analyses were calculated in terms of the error in the calculated vertical stiffness (K):

$$\text{Error}(\%) = \frac{K_p - K_e}{K_e} \times 100 \tag{3.26}$$

where

$$K = \frac{V(1-\nu)}{4GRu_v} \tag{3.27}$$

and the subscripts p and e denote predicted and exact quantities, respectively. The results are presented in Figure 3.5, where the effect of Poisson's ratio ν is quantified through the expression $\log_{10}(2/1-2\nu)$. Two dimensional visualisations of the linear strain and quadratic strain tetrahedra meshes are presented in Figures 3.6 and 3.7, respectively. The results in Figure 3.5 show that under compressible conditions ($\nu = 0.4$), the linear strain and quadratic strain tetrahedra meshes give the same result. But as incompressible conditions are approached ($\nu \rightarrow 0.5$), the error associated with the linear strain element increases at a much greater rate than the error for the quadratic strain element. Furthermore the former is seen to be still increasing at $\nu = 0.49999$ ($\log_{10}(2/(1-2\nu)) = 5$), while the latter has become constant.

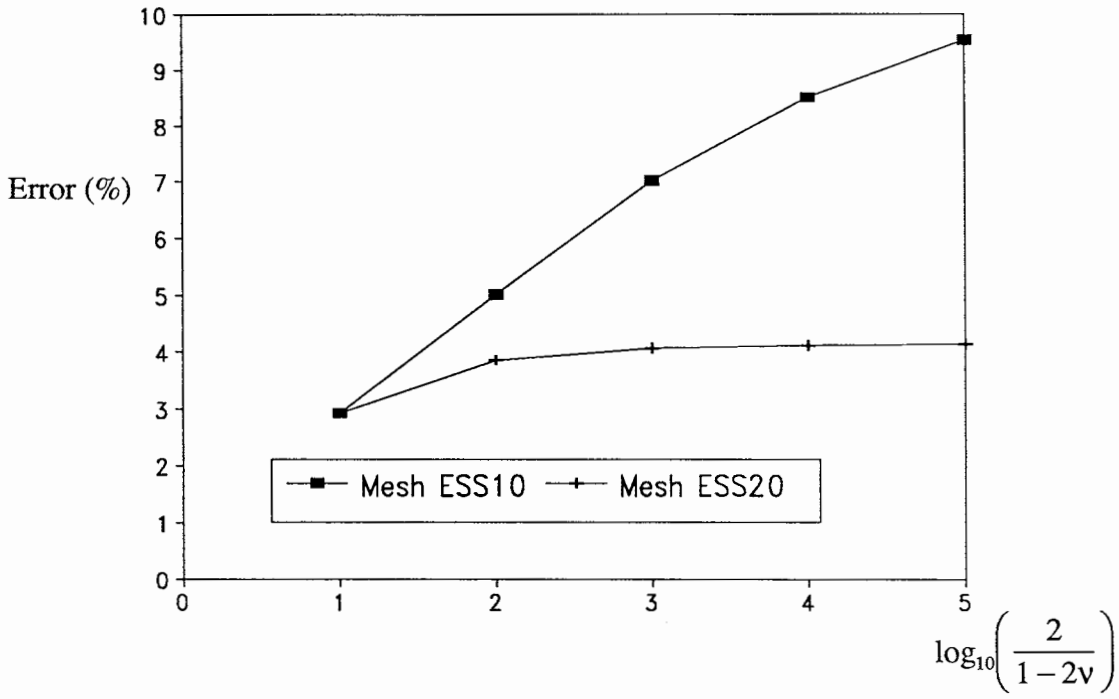

Figure 3.5: The comparison of 10-node and 20-node tetrahedra for a vertically loaded smooth rigid circular surface footing under elastic incompressibility conditions. (Meshes ESS10 and ESS20 are presented in Figures 3.6 and 3.7, respectively).

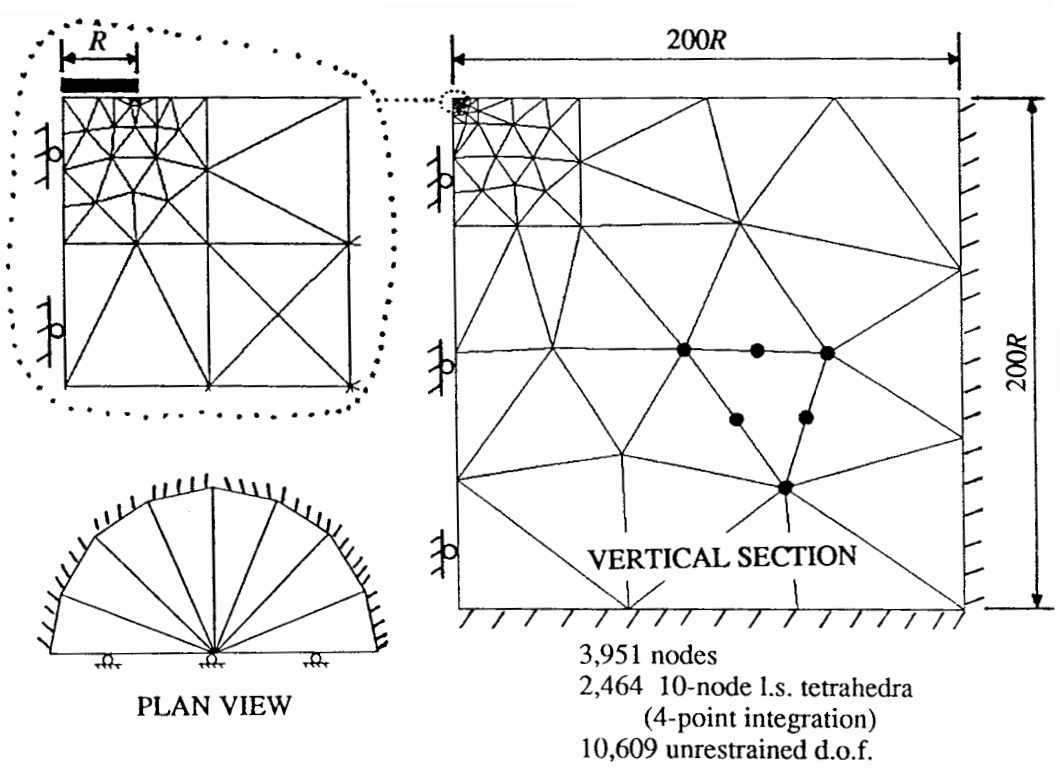

Figure 3.6: Mesh ESS10: 10-node linear strain tetrahedra

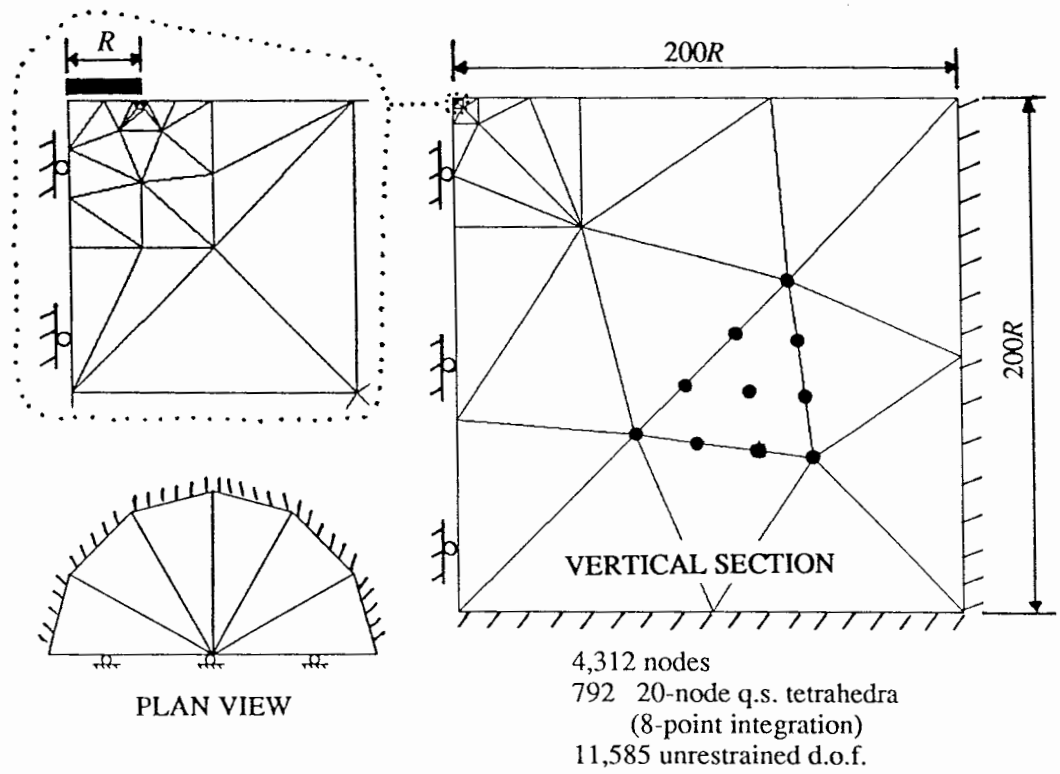

Figure 3.7: Mesh ESS20: 20-node quadratic strain tetrahedra

In the second experiment, the vertical collapse load for a rigid rough circular footing at the surface of a weightless elastic perfectly-plastic von Mises material was investigated. The non-linear load-displacement curves and the 10-node linear strain and 20-node quadratic strain tetrahedra meshes are presented in Figures 3.8, 3.9 and 3.10, respectively. No exact collapse load is known for this problem, however, for a Tresca yield criterion, Eason and Shield (1960) calculated for a rough footing, using upper and lower bound techniques, a vertical collapse load of $6.05s_u/(\pi R^2)$, where s_u is the shear (cohesive) strength of the soil. The collapse load for the von Mises material is therefore greater than $6.05s_u/(\pi R^2)$ and less than $6.05s_u/(\pi R^2)$ multiplied by $2/\sqrt{3}$. This is because in a triaxial stress state the von Mises yield criterion is equivalent to the Tresca yield criterion and in plane strain the von Mises criterion represents the Tresca criterion multiplied by a factor of $2/\sqrt{3}$. For a circular footing, the stress states are intermediate between triaxial and plane strain.

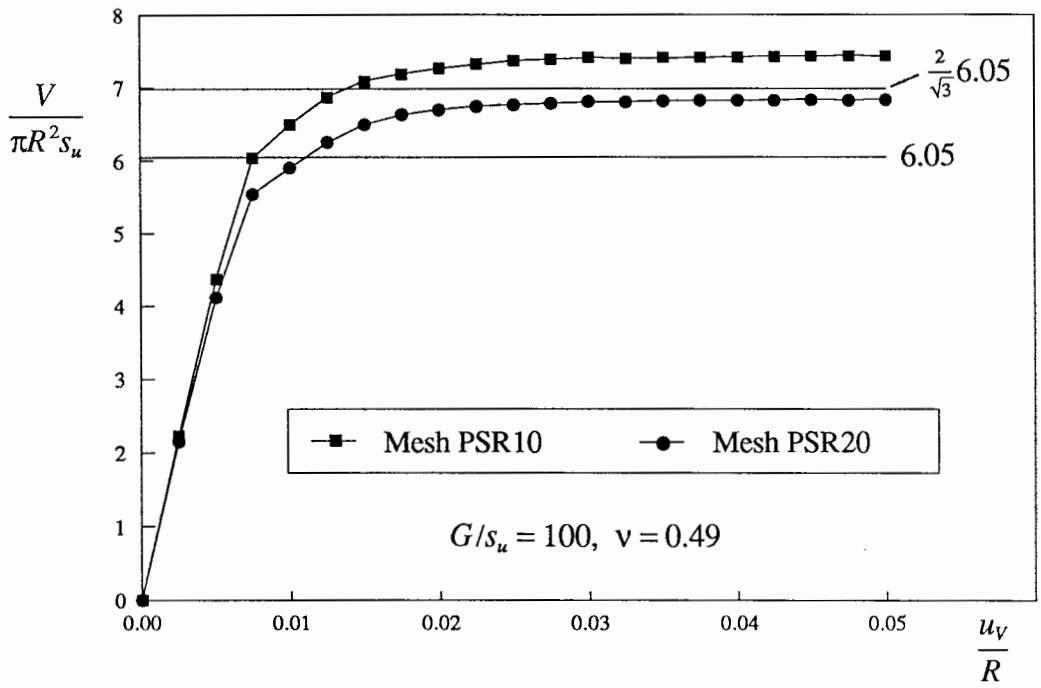

Figure 3.8: The comparison of 10-node and 20-node tetrahedra for the prediction of the vertical collapse load of a rigid rough circular footing at the surface of a von Mises material. (Meshes PSR10 and PSR20 are presented in Figures 3.9 and 3.10, respectively)

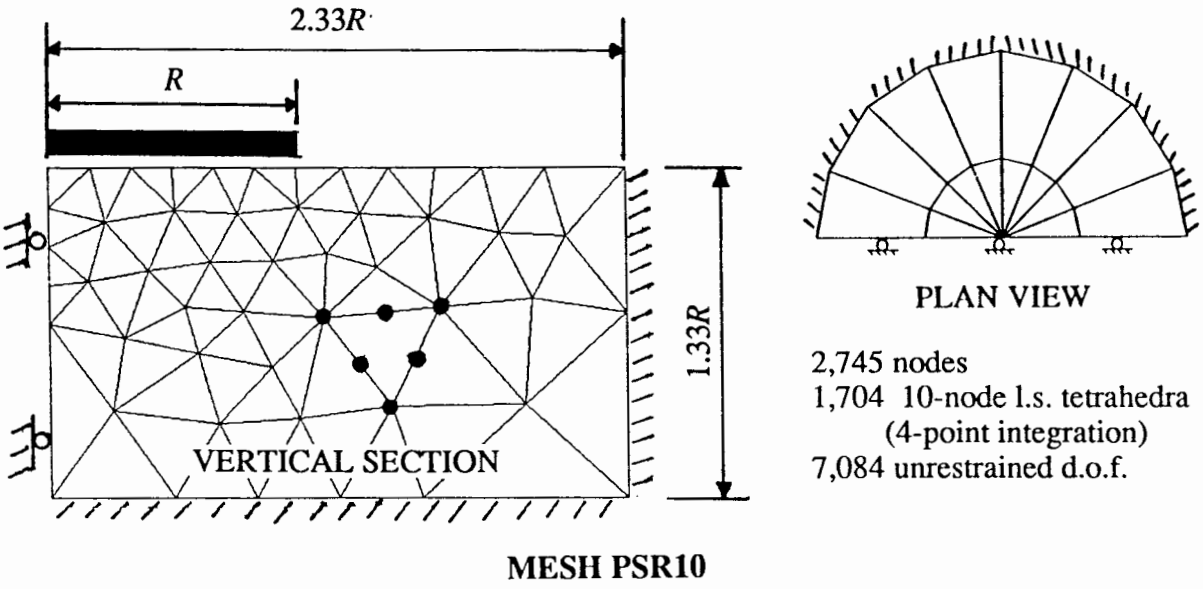

Figure 3.9: Mesh PSR10: 10-node linear strain tetrahedra

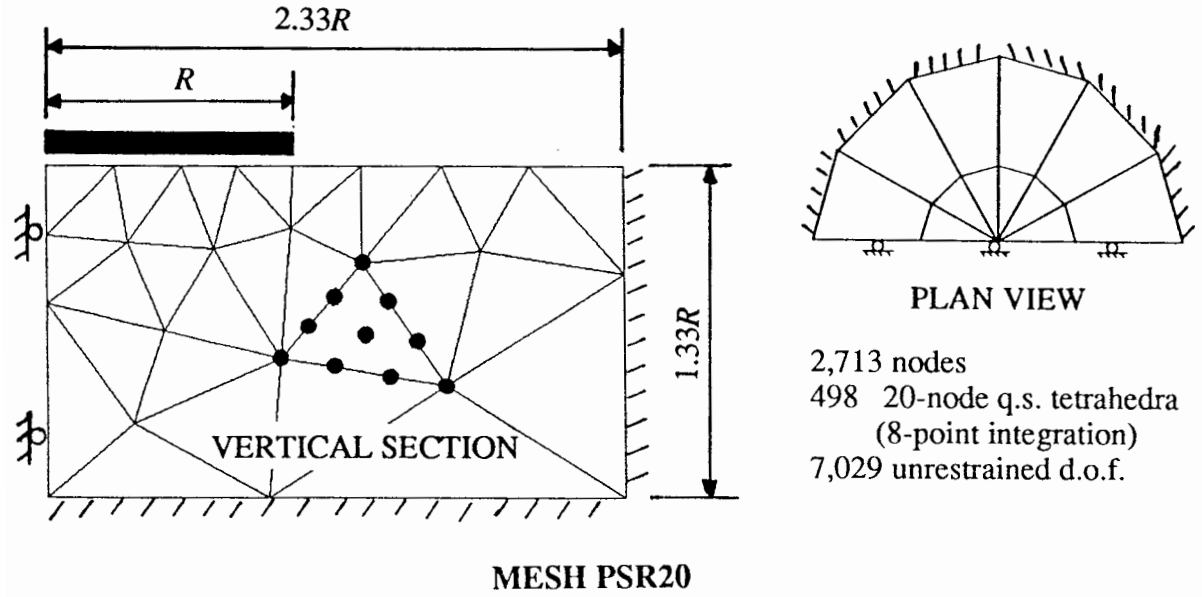

Figure 3.10: Mesh PSR20: 20-node quadratic strain tetrahedra

The 20-node tetrahedra mesh predicts the collapse load to be within the upper and lower limits discussed previously. The 10-node tetrahedra mesh gives a promising result in that a limit load is clearly reached, but this value is well above both the 20-node tetrahedron collapse load and the upper limit for a von Mises material. Analysis of this problem in Section 5.3 using a two dimensional axisymmetric formulation, 15-node cubic strain triangles and a very refined mesh, suggests the exact vertical collapse load to be about $6.65 s_u \pi R^2$. The 20-node tetrahedron collapse load, shown in Figure 3.8, is therefore within 3% of the exact collapse load. The corresponding error for the 10-node tetrahedron is estimated to be +13%.

The procedure used to generate the meshes of Figures 3.6, 3,7, 3.9 and 3.10 is described in detail in Section 3.3. It should be noted that the mesh dimensions differ substantially for the elastic and elasto-plastic analyses of Figures 3.5 and 3.8. Justification and verification of these mesh dimensions are given in Sections 4.3 and 5.3, respectively. For a given experiment, the number of nodes in the 10 and 20 node tetrahedra meshes were within 10% and the total computation times were just as similar. Included in Figures 3.6, 3.7, 3.9 and 3.10 is the number of unrestrained degrees-of-freedom, which for the 10-node tretrahedron meshes in particular, always exceeded the number of incompressibility constraints.

3.2.6. Discussion

The results in Figures 3.5 and 3.8 support the concepts introduced in this section. Under incompressibility conditions for meshes with similar numbers of nodes, the 20-node quadratic strain tetrahedron clearly performs better than the 10-node linear strain tetrahedron. This greater accuracy is a result of more *free* degrees-of-freedom being available in the 20-node tetrahedron mesh. For example, using the elastic analysis in Figure 3.5, the 20-node tetrahedron mesh (Mesh ESS20) has a total number of 11,585 unrestrained degrees-of-freedom and 7,920 incompressibility constraints (= 792 elements x 10 constraints per element) which leaves a remainder of 3,665 free degrees-of-freedom. A similar calculation for the 10-node tetrahedron mesh (Mesh ESS10) gives a much smaller number of 753 free degrees-of-freedom. A similar comparison can be made for the meshes of Figure 3.8, which have 2,049 and 268 free degrees-of-freedom respectively.

Sloan (1981) performed a large number of vertical collapse load calculations for plane strain and axisymmetric conditions, using various unsuitable, marginal and suitable two-dimensional

finite elements. Close examination of his study shows agreement with the collapse load experiment of Figure 3.8 and the findings of this section. Table 3.5 summarises the experiments of Sloan (1981) in terms of free degrees-of-freedom and error in collapse load prediction, and includes the corresponding numbers from Figure 3.8. For plane strain conditions, the 8-node and 12-node quadrilaterals, which are on the border-line of suitability ($f_n^* = 0$), are observed to produce acceptably accurate results as long as the number of free degrees-of-freedom exceeds about 10. Unfortunately this corresponds to a very low ratio of free degrees-of-freedom to unrestrained degrees-of-freedom and is therefore very inefficient. For a given level of accuracy, a better computational performance is provided by an element such as the 15-node cubic strain triangle, which introduces free degrees-of-freedom within each element and therefore has a considerably higher ratio of free degrees-of-freedom to unrestrained degrees-of-freedom. The one anomalous result in Table 3.5 is for a linear strain triangle, an element which would usually be expected to perform well ($f_n^* = 0.5$), in which a plane strain analysis involving 155 free degrees-of-freedom produced an overshoot of the collapse load by 7%. The explanation may be in the fact that for this analysis only, Sloan (1981) used a 7-point integration scheme when a three point integration is all that is necessary. This points to the possibility that "over-integration" of the element stiffness may result in further constraints on the solution, although the precise mechanism by which this could occur is unclear.

Table 3.5 shows similar trends for both two and three dimensional axisymmetric analyses, except for this case at least 50 free degrees-of-freedom (in the two-dimensional sense) are required for the vertical collapse load to be predicted within 5%. The equivalent number of two-dimensional degrees-of-freedom for three-dimensional analysis are obtained by dividing by the number of radial planes of nodes in the mesh. The comparison should be regarded as only approximate. The issue of computational efficiency is reiterated in Table 3.5, where the 10-node linear strain tetrahedron ($f_n^* = 0$) is considerably less accurate than the 20-node quadratic strain tetrahedron ($f_n^* = 0.78$) for meshes with similar numbers of unrestrained degrees-of-freedom and total computational effort.

The favourable performance of elements on the border-line of suitability ($f_e^* = 0$), such as the 10-node linear strain tetrahedron and 8-node and 12-node quadrilateral elements (in plane strain), may be a consequence of more than just *free* boundary degrees-of-freedom. Figure 3.5 demonstrates that the detrimental effects of incompressibility are not fully apparent when

Table 3.5: The relationship between free degrees-of-freedom and collapse load prediction for two and three dimensional finite elements

Element Type	Free degrees-of freedom per node (f_n^*)	Mesh[1] Reference	Unrestrained degrees-of freedom	Incompress-ibility constraints	Free[2] degrees-of-freedom	Error in[3] collapse load (%)
PLANE STRAIN						
8-node quadrilateral	0	SRF8	156	150	6	13
8-node quadrilateral	0	SRF9	392	384	8	10
8-node quadrilateral	0	SRF4	496	486	10	5
8-node quadrilateral	0	SRF10	726	714	12	4
12-node quadrilateral	0	SRF1	94	90	4	#
12-node quadrilateral	0	SRF2	257	250	7	12
12-node quadrilateral	0	SRF5	503	490	13	5
12-node quadrilateral	0	SRF3	739	720	19	4
Linear strain triangle	0.5	SRF6	584	429 [4]	155	7
Cubic strain triangle	0.75	SRF7	786	480	306	1
TWO DIMENSIONAL AXISYMMETRY						
12-node quadrilateral	-0.6	SRF3	726	936	-210	#
Linear strain triangle	-1.0	SRF6	584	858	-274	#
Cubic strain triangle	0.125	SRF7	786	720	66	5
THREE DIMENSIONAL AXISYMMETRY						
Linear strain tetrahedron	0	PSR10	7084	6816	268 (16)	13
Quadratic strain tetrahedron	0.78	PSR20	7029	4980	2049 (108)	3

Notes:
1. SRF* mesh results taken from Sloan (1981).
2. Numbers in brackets correspond to an equivalent two-dimensional mesh.
3. # Load not observed to achieve a clearly defined limit value.
4. Used a 7-point integration scheme.

ν=0.49, with this being the value of Poisson's ratio adopted in many nominally incompressible analyses (Sloan, 1981; Sloan and Randolph, 1982), including the non-linear analysis presented in Figure 3.8. This may be one reason why elements with $f_e^* = 0$ have given favourable results. A further reason may be a consequence of the mesh topology adopted. Special arrangements of elements can result in the total number of incompressibility constraints being less than the product of the number of elements and the number of constraints per element (Nagtegaal *et al*, 1974; Burd and Houlsby, 1990).

3.2.7 Summary

This section has introduced a new quantitative approach for evaluating the suitability of finite elements for accurate analysis of incompressible materials. The previously used method is considered not to provide a rigorous quantitative measure of element suitability, nor to allow comparisons between elements of different order and type, when computational effort is a consideration. Hence three new parameters, quantified in terms of *free* degrees-of-freedom (equal to the degrees-of-freedom minus the incompressibility constraints) have been introduced and applied to two and three dimensional finite elements.

The tetrahedron family is the most suitable and computationally efficient group of three-dimensional elements for incompressible material analysis, when using the displacement finite element method and exact integration. The Serendipity cube family is unsuitable. Similarly the first two elements of the Lagrangian cube family, the 8-node and 27-node cubes, are unsuitable, while all higher order elements are suitable, but computationally inefficient. The examination of the tetrahedron family was divided into two categories since a cube can be divided into either 5 and 6 tetrahedra. The constant strain tetrahedron is unsuitable for both categories. The linear strain tetrahedron is suitable when used in a 5 tetrahedra per cube arrangement and is on the border-line of suitability in a 6 tetrahedra per cube arrangement, since the number of *free* degrees-of-freedom per element (similarly per node) is zero. The latter is thought to be only suitable if the mesh boundary nodes are not over-constrained, although it must be stressed that the analysis would be very inefficient because of the poor ratio of free to total degrees-of-freedom. All subsequent higher order tetrahedra produce *free* degrees-of-freedom and are therefore suitable. For the finite element model adopted in this thesis, the quadratic strain and cubic strain tetrahedra are thought to be the most computationally efficient.

Based on the favourable performance of the 20-node quadratic strain tetrahedron in the numerical experiments of sub-section 3.2.5, it has been chosen for all subsequent analyses in this thesis. Adopting the 35-node cubic strain tetrahedron, which may be more computationally efficient, was considered inappropriate due to the complexity of coding associated with using such a high order element.

3.3 Mesh Generation

Mesh generation for three-dimensional problems is significantly more complex than planar two-dimensional problems. At present very few computer codes have been developed which can generate a mesh of tetrahedral elements for a problem of general geometry. In this research, Program OX3DFM, a much more specific three-dimensional tetrahedron mesh generator, has been developed for the circular footing problem. A simple example of the footing mesh generation procedure is given in Figure 3.11, which also includes the mesh boundary conditions (node fixities) adopted.

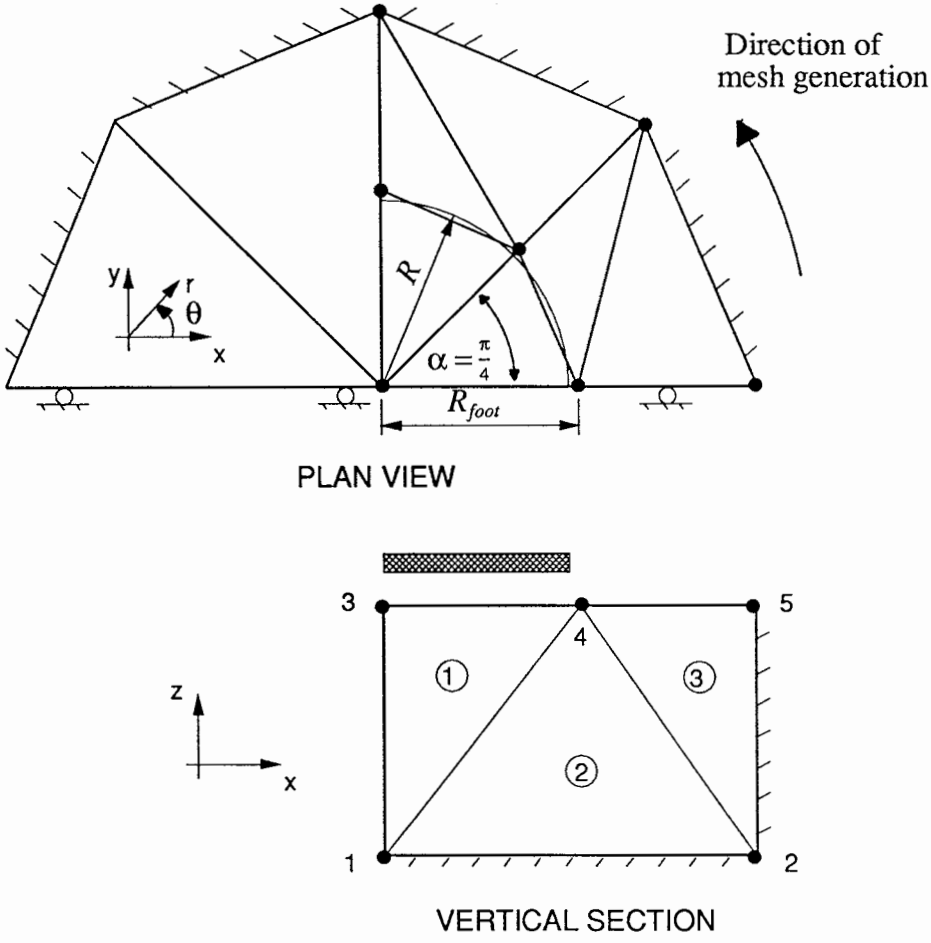

Figure 3.11: Schematic example of the footing mesh generation procedure.

The three-dimensional meshes analysed in this research utilise the symmetry of the problem about the vertical plane in which all loads are assumed to act, corresponding to the direction of the environmental loading (Section 1.2). This plane of symmetry is taken to be the plane defined

by the x and z axes. The meshes are divided into two quadrants, where each quadrant is divided into a number n of vertical sectors. A mesh is formed by generating a two-dimensional mesh of 3-node triangles[5] (vertical section in Figure 3.11) and rotating it about the vertical (z) axis, using cylindrical coordinates, to form the vertical sectors (plan view in Figure 3.11). Triangular elements which do not coincide with the vertical axis (Element 3 in Figure 3.11), which is the common case, form distorted triangular prisms which are divided into three 4-node tetrahedra, as earlier illustrated in Figure 3.4c. Three-node triangles which do coincide with the vertical axis (Elements 1 and 2 in Figure 3.11) result in the formation of one or two 4-node tetrahedron within each sector, depending on whether the element edge or corner is on the vertical axis. Higher order tetrahedron are simply generated by adding edge and face nodes to the existing 4-node tetrahedra.

Program OX3DFM only generates tetrahedral elements which have straight edges and flat faces. The use of curved elements can introduce an unnecessary error into the analysis because the numerical integration scheme used to compute the element stiffnesses is only exact for straight sided elements. Adopting straight sided elements throughout the mesh can give rise, however, to the overlap of the elements defining the circular footing edge and those more external to the footing. To avoid this problem, which can be difficult to detect, and to maintain exact integration, it was decided to model the circular footing edge by a series of segments such that the area of each segment is the same as each sector (Figure 3.11), and the total area of the footing is therefore conserved. This involves adjusting the radius of the node defining the footing edge (R_{foot}) in the two-dimensional mesh (node 4 in Figure 3.11), as follows

$$R_{foot} = \sqrt{\frac{\alpha}{\sin\alpha}} \times R \tag{3.28}$$

where α is the sector angle (in radians), which is defined by the number of sectors per quadrant (n), as given below

$$\alpha = \frac{\pi}{2} \times \frac{1}{n} \tag{3.29}$$

5 The two-dimensional triangular mesh is generated using the software OXMESH

For the schematic example of Figure 3.11, the edge node radius is adjusted by a factor of 1.054, since there are two sectors per quadrant ($n = 2$). For $n = 3$ and 4, representative of the meshes analysed in this thesis, the edge adjustment reduces to 1.023 and 1.013, respectively, and the radial difference between the circular footing edge and each segment is only on average half of 0.023 and 0.013. Therefore, the error associated with using this simplified footing geometry, when modelling a circular footing, is considered insignificant when compared with other errors inherent in the finite element method.

Other aspects of Program OX3DFM worth noting are:

- it also has the ability to generate 1 and 4 quadrant footing meshes, embedded footings (Chapter 4), and horizontal interface elements (Chapter 5);
- following mesh generation, the nodes and elements are re-ordered using the mesh optimisation scheme developed by Sloan (1981), aimed at minimising the computational effort in the frontal solution procedure (discussed in Section 2.4);
- extensive checks are implemented to ensure that all element node-numbering is consistent; and
- the program writes the mesh information to file in a format consistent with the input format used in the three-dimensional finite element program OXFEM2.

CHAPTER 4 ELASTIC BEHAVIOUR

4.1 Introduction

While the design of offshore foundations is principally concerned with an examination of the ultimate capacity, as addressed in Chapter 5, the elastic behaviour of offshore foundations is also of some importance. Firstly, the preliminary stage in the design of an offshore foundation is to use elasticity theory to estimate the deformations caused by the applied loads (Poulos, 1988). The elastic behaviour is also of relevance to the structural analysis of offshore structures where elastic stiffness values are used to represent the compressibility of the foundation soil. There is also an increasing realisation of the importance of the dynamic behaviour of jack-up platforms, where the assessment of the jack-up natural frequency depends on the foundation elastic stiffness (Hambly *et al*, 1990).

All analyses presented in this chapter model the soil as an isotropic homogeneous elastic half-space. The first half of the chapter presents a thorough analytical review and numerical analysis of the deformation characteristics of a rigid circular surface footing. This reveals some inadequacies in the presently available analytical solutions for this class of problem. The latter half of the chapter addresses the important effect of footing embedment using, as for the surface footing, analytical and numerical approaches to the problem.

4.2 Analytical Surface Footing Solutions

Most of the available elastic solutions refer to footings placed at the ground surface. The main reference for elastic solutions in soil mechanics is Poulos and Davis (1974). Four closed-form solutions are given on pages 166 and 167 of this book for a rigid circular flat footing at the surface of an elastic half-space subjected to vertical, horizontal, moment and torsional loads. Examination of the derivation and boundary conditions of these solutions has shown that two refer to a smooth footing, one refers to a rough footing and the other is not exact. This section separates these and other solutions into smooth and rough footing categories for which six cases in total exist.

4.2.1 Smooth footing

For a smooth surface footing, horizontal or torsional loading cannot be applied, since shear stress cannot be transmitted between the base of the footing and the soil. For the vertical and moment loading cases, Poulos and Davis (1974) give closed-form elastic solutions as follows:

Vertical loading

$$u_V = \left[\frac{1-\nu}{4GR}\right]V \tag{4.1}$$

where u_V and V are the vertical displacement and force respectively, G is the elastic shear modulus of the soil, ν is the Poisson's ratio of the soil, and R is the radius of the footing.

Moment loading

$$\theta_M = \left[\frac{3(1-\nu)}{8GR^3}\right]M \tag{4.2}$$

where θ_M and M are the overturning rotation and moment respectively.

Close examination of the derivation of Equations (4.1) and (4.2) confirms that these solutions are exact for a smooth rigid circular footing.

4.2.2 Rough footing

A rough (adhesive) footing is characterised by the fact that the base of the footing is rigidly connected to the soil, thus allowing a full transmission of shear stress. In this instance, all four cases of loading are possible.

Vertical loading

A rigid rough flat circular footing subjected to vertical loading was not considered by Poulos and Davis (1974), who only provide a solution for the smooth footing case (Equation 4.1). Spence (1968), however, provides an exact solution that satisfies the boundary conditions for a rough footing and can be written

$$u_V = \left[\frac{1-2\nu}{4GR\ln(3-4\nu)} \right] V \tag{4.3}$$

where the notation adopted is the same as used in Equation (4.1).

Torsional loading

Poulos and Davis (1974) give the following exact solution for a rough rigid footing subjected to a torsional loading:

$$\theta_T = \left[\frac{3}{16GR^3} \right] T \tag{4.4}$$

where θ_T and T are the torsional rotation and moment respectively. This equation has been included here for completeness, but this loading case will not be considered any further since it is not of great relevance to offshore foundations.

Horizontal and moment loading

The horizontal and moment loading cases for a rough footing are grouped together since they are cross coupled. That is, in a compressible soil, a circular rigid footing subjected purely to a horizontal load will not only displace horizontally, but will also rotate about a horizontal axis normal to the direction of the horizontal load. Similarly, a moment will produce both a rotation and a horizontal displacement. For the combined loading problem under consideration, the stiffness of a footing can be written in the following matrix form in terms of the four non-dimensional coefficients K_1 - K_4:

$$\begin{bmatrix} V/(GR^2) \\ H/(GR^2) \\ M/(GR^3) \end{bmatrix} = \begin{bmatrix} K_1 & 0 & 0 \\ 0 & K_2 & K_4 \\ 0 & K_4 & K_3 \end{bmatrix} \begin{bmatrix} u_V/R \\ u_H/R \\ \theta_M \end{bmatrix} \tag{4.5}$$

The cross coupling of the horizontal and moment components is represented by the coefficient K_4. For the smooth footing case previously examined, it is clear that K_2 and K_4 are zero and K_1 and K_3 are given by Equations (4.1) and (4.2) respectively. For a rough surface footing, K_1 corresponds to Equation (4.3), while for K_2, K_3 and K_4 no exact solutions are known to exist, except for the important case of incompressible soil conditions ($\nu = 0.5$), as demonstrated later

in this chapter. Before examining approximate solutions to the horizontal loading case, it is important to realise that these solutions fail to recognise the existence of the cross coupling coefficient K_4 and are intended in a flexibility sense, that is, the deformations are written in terms of the loads. The complete flexibility relationship can be obtained by inverting the stiffness relationship of Equation (4.5) to give

$$\begin{bmatrix} u_V/R \\ u_H/R \\ \theta_M \end{bmatrix} = \begin{bmatrix} F_1 & 0 & 0 \\ 0 & F_2 & F_4 \\ 0 & F_4 & F_3 \end{bmatrix} \begin{bmatrix} V/(GR^2) \\ H/(GR^2) \\ M/(GR^3) \end{bmatrix} \tag{4.6}$$

where the coefficients of the matrices $[F]$ and $[K]$ are related as follows:

$$F_1 = \frac{1}{K_1}$$

$$F_2 = \frac{K_3}{K_2K_3 - K_4^2}$$

$$F_3 = \frac{K_2}{K_2K_3 - K_4^2} \tag{4.7}$$

$$F_4 = \frac{-K_4}{K_2K_3 - K_4^2}$$

A solution for a rigid rough circular footing subjected to an overturning moment has not been found in the literature, however, two approximate solutions exist for the horizontal loading of a rigid rough circular footing. The first is given by Poulos and Davis (1974) who reference the work of Bycroft (1956). This solution is apparently intended to represent the coefficient F_2 in Equation (4.6). The resulting relationship between the horizontal displacement (u_H) and horizontal force (H) can be written

$$u_H = \left[\frac{7 - 8\nu}{32GR(1-\nu)} \right] H \tag{4.8}$$

In the derivation of Equation (4.8), Bycroft (1956) initially adopted the condition that the footing should not deflect vertically at any point, so as to simplify the solution to the problem. This condition actually makes Equation (4.8) more applicable to the coefficient K_2 (Equation 4.5) than F_2 as intended. His justification for this approach was that it had been observed

experimentally that the rotation caused by a horizontal force is small and the effect on the horizontal displacement of preventing this rotation will be this degree of smallness squared. It turns out, however, and is admitted by Bycroft, that the resulting solution involves some vertical deformation and therefore does not represent K_2 exactly either.

The second horizontal loading solution is found in Gerrard and Harrison (1970), this paper also appearing as Appendix B in Poulos and Davis (1974). Gerrard and Harrison derive solutions for a range of circular footing problems and include the added complexity of anisotropy. Solutions are given for vertical, moment and torsional loading of a rigid footing, which when simplified to their isotropic form agree with those given by Poulos and Davis (1974) (and are repeated in this section in Equations 4.1, 4.2 and 4.4). However, the isotropic solution for a horizontally loaded rigid footing differs from that quoted in the main text of Poulos and Davis (1974) (Equation 4.8) and takes the form

$$u_H = \left[\frac{2-\nu}{8GR}\right] H \tag{4.9}$$

This solution attempts to model the coefficient F_2 in Equation (4.6), but is inexact as it does not comply fully with the boundary conditions imposed by a rigid rough footing. The solution corresponds to a footing which displaces rigidly in the horizontal plane, but flexes in the vertical plane instead of rotating rigidly. Johnson (1985), who also derives Equation (4.9) for the given boundary conditions, states that the solution to the problem of a rigid footing displaced both horizontally and vertically has not been solved. However, he believes that the stress distribution at the footing, and therefore the relationship between u_H and H will not be very different from that given in Equation (4.9). This is demonstrated to be the case in Section 4.3, where a numerical solution is examined.

It is important to note that for the case of undrained conditions ($\nu = 0.5$), where the soil is incompressible, the cross coefficients K_4 and F_4 are zero, and the horizontal and moment loading components therefore become independent. This fact is demonstrated numerically in Section 4.3. In this case Bycroft's and Gerrard and Harrison's solutions are exact and the stiffness coefficient $K_2 = 5.333$. Similarly $K_3 = 5.333$, as the moment loading solution for a rough footing is the same as that for a smooth footing (Equation 4.2) when $\nu = 0.5$.

4.2.3 Evaluation of the cross coupling coefficients for horizontal and moment loading

The derivation of the exact elastic solutions for horizontal and moment loading of a rough surface footing is dependent on the determination of three coefficients: K_2, K_3, K_4 (Equation 4.5) or F_2, F_3, F_4 (Equation 4.6). It is thought that the analytical solution of the governing elastic equations can, if possible, be most easily achieved by evaluating coefficients K_2, K_3, K_4. The cases for analysis, together with the corresponding boundary conditions and quantities which must be evaluated, are specified below. Note that a Cartesian coordinate system is adopted with (u, v, w) being the displacements in the (x, y, z) directions, and in both cases the boundary conditions outside the footing are those of a stress free surface.

Rigid horizontal displacement

Boundary conditions:

$$\begin{aligned} u &= u_H \\ v &= 0 \\ w &= 0 \end{aligned} \tag{4.10}$$

Evaluate:

$$H = \int \tau_{zx} dA \Rightarrow K_2 = \frac{H}{GRu_H} \tag{4.11}$$

$$M = \int \sigma_z x dA \Rightarrow K_4 = \frac{M}{GR^2 u_H} \tag{4.12}$$

Rigid rotation

Boundary conditions:

$$\begin{aligned} u &= 0 \\ v &= 0 \\ w &= x\theta_M \end{aligned} \tag{4.13}$$

Evaluate:

$$H = \int \tau_{zx} dA \Rightarrow K_4 = \frac{H}{GR^2 \theta_M} \tag{4.14}$$

$$M = \int \sigma_z x dA \Rightarrow K_3 = \frac{M}{GR^3 \theta_M} \tag{4.15}$$

Note that there are two ways of evaluating coefficient K_4. Coefficients F_2, F_3, F_4 can now be simply determined by substituting the above stiffness coefficients into Equation (4.7).

As discussed by Bell *et al* (1991b), this approach is referred to as a mixed boundary condition problem, and can in some cases lead to the solution of dual integral equations. No attempt is made here to obtain an analytical solution to this complex problem, but instead numerical techniques are used in the following section.

4.3 Numerical Surface Footing Solutions

4.3.1 Mesh dimensions and topology

Application of the finite element method to footing analysis has largely concentrated on the plastic response and prediction of vertical collapse loads (Sloan, 1981; Sloan and Randolph, 1982; de Borst and Vermeer, 1984). In these analyses the mesh dimensions were generally of the order five times the width of the footing, or in the case of a circular footing, ten times the radius ($10R$). These exact mesh dimensions were adopted by Sloan (1981) in his analysis of smooth rigid strip and circular footings. Using the appropriate finite element formulations, exact collapse loads were predicted to within 1 % accuracy. However, the initial tangent of the load - displacement curves showed a repeatable 10 % overprediction of the initial elastic stiffness. Table 4.1 demonstrates this overprediction to be a consequence of the closeness of the mesh boundaries to the footing.

The effect of mesh dimensions on the accuracy of elastic footing analysis, presented in Table 4.1, was analysed using a mesh of 6-node triangular elements and the program OXFEM (Oxford Soil Mechanics two-dimensional finite element model). The problem of a vertically loaded smooth rigid circular footing placed at the surface of an elastic compressible half-space (ν = 0.25) was considered for which an exact solution, given by Equation (4.1), exists. For a footing of radius R, two-dimensional meshes of dimensions $10R$ x $10R$, $50R$ x $50R$ and $200R$ x $200R$ were refined until no further significant improvement in numerical accuracy was achieved. For each mesh, the error in vertical stiffness, presented in Table 4.1, is calculated using Equations (3.26) and (3.27) introduced in Section 3.2. A coarse example of the topology of the meshes used is given in the vertical section of Figure 3.6 (Mesh ESS10).

Table 4.1: The effect of mesh dimensions on the accuracy of elastic footing analysis.

Mesh dimensions (DxD)	R/D (%)	Number of nodes	Number of[2] elements	Error in[3] stiffness (%)
10Rx10R	10.0	452	205	+10.3
50Rx50R	2.0	528	239	+2.4
200Rx200R	0.5	586	265	+1.1

Notes:
1. Results correspond to a vertically loaded smooth rigid circular footing (radius R) placed at the surface of an elastic half-space with $\nu = 0.25$.
2. The mesh consists of 6-node triangular elements and is analysed using the two-dimensional program OXFEM.
3. Refer to Section 3.2 and Equations (3.26) and (3.27) for details of the error calculation.

Table 4.1 demonstrates that the error in numerical prediction decreases significantly with an increased mesh dimension (D). It can be shown for a point load that the error due to a finite boundary, in this case a mesh boundary, is inversely proportional to the distance to the fixed boundary. For a circular footing, this can be approximated by the non-dimensional parameter R/D, and is thought to become more applicable the greater the distance from the footing to the boundary. The parameter R/D, expressed as a percentage, is included in Table 4.1 and compares well with the observed errors, the latter being on average 0.5% greater. This difference may be due to discretisation errors in the finite element mesh close to the footing, which are not affected by the mesh dimension.

All three-dimensional surface footing elastic analyses presented in this section use the 20-node quadratic strain tetrahedron mesh presented in Figure 3.7 (Mesh ESS20) of Chapter 3, which has a mesh dimension of 200R. Taking into account the results of Table 4.1, the error in stiffness due to the proximity of the mesh boundaries is estimated to be of the order +0.5 %. Adopting a larger mesh dimension, and therefore a larger number of nodes and elements, is considered inefficient as the small improvement in accuracy does not compensate for the increased computational effort. Note that in Mesh ESS20, special care was taken to pack a high density

of elements under the edge of the rigid footing where high stress and strain gradients occur. Also note the extreme gradation of very small elements close to the footing to large elements near the boundary of the mesh.

4.3.2 Numerical integration for the 20-node tetrahedron

The commonly used finite element texts by Zienkiewicz (1977) and Kardestuncer and Norrie (1987) advocate the use of a 5-point Gaussian integration scheme for the numerical integration of the stiffness matrix for the 20-node quadratic strain tetrahedron adopted in this thesis. This scheme involves a negative weighting of -0.8 at the centroid of the tetrahedron. While this scheme is exact when integrating functions up to order 3, it produces spurious solutions when terms of a higher order exist, as is the case in the finite element method. Zienkiewicz (1977) and Kardenstuncer and Norrie (1987) make no mention of this limitation of the 5-point scheme, however, Gens et al (1989) do note the detrimental effect of a negative Gauss point weighting.

An alternative 8-point scheme for tetrahedra, exact to order 3 (quadratic strain), has been developed by Abramowitz and Stegun (1964) and is used in this research. This scheme is given in Appendix A.1, as it is not found in common finite element texts. It has positive weightings and integration points located at the corners and centroid of each triangular face. The location of the Gauss points at the surface of the element proves most advantageous when processing the stress data.

4.3.3 Results and comparison with analytical solutions

The analytical solutions for vertically loaded smooth and rough footings (Equations 4.1 and 4.3 respectively) are plotted in the non-dimensional form $V/(GRu_V)$ against Poisson's ratio (ν) in Figure 4.1 and are compared with numerical results at discrete values of ν. For both rough and smooth conditions, the numerical results compare well, with the error being in the range +2.5% to +3.9% for $\nu = 0.0$ to 0.49. The smooth and rough analytical solutions show the stiffness of rough footing to be about 10% greater than the smooth footing at $\nu = 0.0$. For undrained soil conditions, $\nu = 0.5$, the analytical solutions are the same, and are well reproduced by the numerical solutions when $\nu = 0.49$ is used in the numerical analysis.

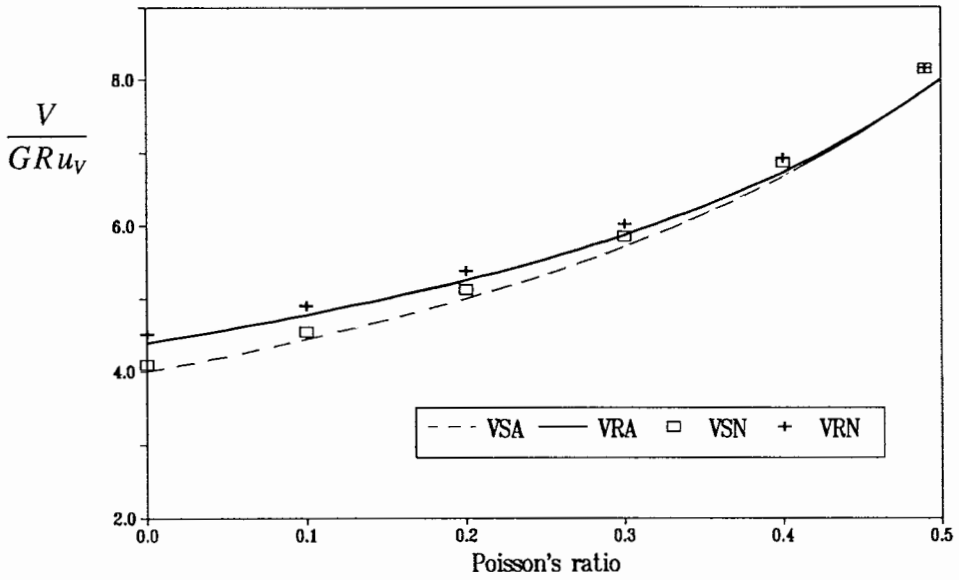

VSA: Smooth footing analytical solution (Equation 4.1)
VRA: Rough footing analytical solution (Equation 4.3)
VSN: Smooth footing numerical solution
VRA: Rough footing numerical solution

Figure 4.1: Results of elastic vertical loading analyses of a surface footing.

For moment loading of a smooth footing, the exact analytical solution (Equation 4.2) is compared with the numerical results in Figure 4.2. The results are expressed in terms of the non-dimensional stiffness parameter $M/(GR^3\theta_M)$. The errors in the numerical solutions are in the range +2.6% to +3.2%, this being very similar to those observed in the vertical loading case.

As discussed in Section 4.2, the horizontal and moment loading cases are cross coupled for a rough footing. This cross relationship can be expressed either as the loads in terms of the deformations (stiffness), Equation (4.5), or the deformations in terms of the loads (flexibility), Equation (4.6). It is far easier in finite element analysis to prescribe the footing node displacements for a rigid body displacement than to use load control. Therefore, the numerical analysis of this section adopted the procedure suggested in Section 4.2 for evaluating the stiffness coefficients K_2, K_3, K_4 of Equation (4.5). That is, the problems of rigid horizontal displacement and rigid footing rotation were examined, for which the results are presented in Table 4.2. It is pleasing to see that the cross coefficient K_4 is the same to 4 significant figures for the displacement and rotation analyses.

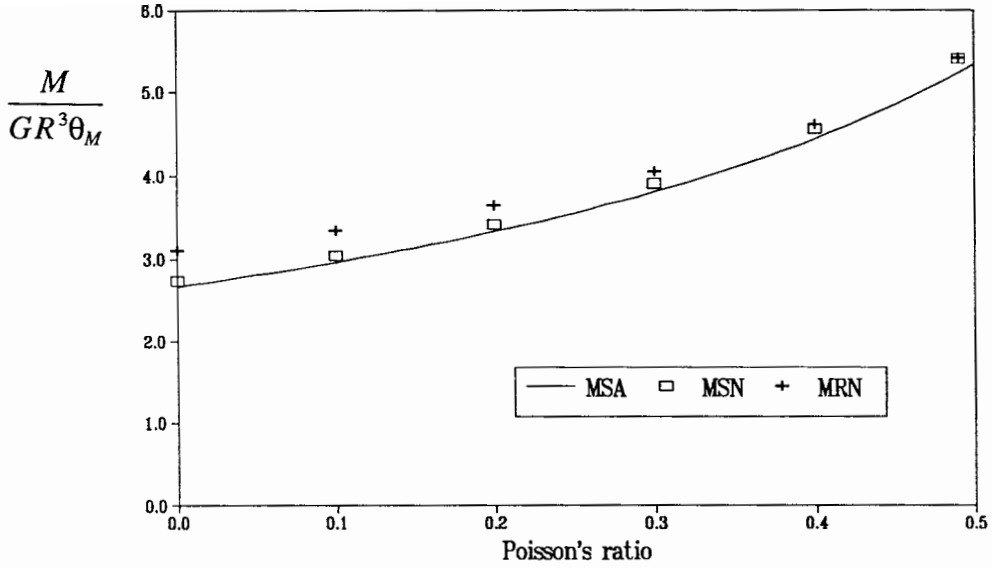

MSA: Smooth footing analytical solution (Equation 4.2)
MSN: Smooth footing numerical solution
MRN: Rough footing numerical solution (= $1/F_3$)

Figure 4.2: Results of elastic moment loading analyses of a surface footing.

Using the relationships given in Equation (4.7), the flexibility coefficients F_2, F_3, F_4, are obtained from the stiffness coefficients K_2, K_3, K_4. These inferred results for horizontal and moment loading are also included in Table 4.2. One of the main features of these results is the cross coupling between the horizontal displacement (u_H) and body rotation (θ_M) for horizontal and moment loading. For pure horizontal loading ($M = 0$), Equation (4.6) can be rearranged to relate θ_M and u_H as follows

$$\frac{\theta_M}{u_H} = \frac{1}{R}\frac{F_4}{F_2} \tag{4.16}$$

or alternatively

$$\frac{u_{V_{edge}}}{u_H} = \frac{F_4}{F_2} \tag{4.17}$$

where $u_{V_{edge}}$ is the maximum vertical edge displacement corresponding to the rotation θ_M. Similarly for pure moment loading ($H = 0$), the following relationships result

Table 4.2: Numerical results for horizontal and moment loading of a surface footing.

	DIRECT RESULTS				INFERRED RESULTS[1]				
	Rigid Horizontal Displacement		Rigid Body Rotation		Horizontal Loading			Moment Loading	
ν	$\frac{H}{GRu_H}$ $(=K_2)$	$\frac{M}{GR^2u_H}$ $(=K_4)$	$\frac{H}{GR^2\theta_M}$ $(=K_4)$	$\frac{M}{GR^3\theta_M}$ $(=K_3)$	F_2	F_4	$\frac{u_{Vedge}}{u_H}=\frac{F_4}{F_2}$ (%)	F_3	$\frac{u_H}{u_{Vedge}}=\frac{F_4}{F_3}$ (%)
0.0	4.271	-0.7364	-0.7364	3.227	0.2437	0.05562	22.8	0.3226	17.2
0.1	4.443	-0.6634	-0.6634	3.441	0.2317	0.04468	19.3	0.2992	14.9
0.2	4.639	-0.5682	-0.5682	3.716	0.2197	0.03359	15.3	0.2742	12.2
0.3	4.868	-0.4401	-0.4401	4.088	0.2074	0.02233	10.8	0.2470	9.04
0.4	5.145	-0.2590	-0.2590	4.628	0.1949	0.01091	5.60	0.2167	5.03
0.49	5.474	-0.0144	-0.0144	5.410	0.1827	4.86×10^{-4}	0.27	0.1848	0.26

Note:

1. The coefficients F_2, F_3, F_4 are obtained from coefficients K_2, K_3, K_4 using Equation (4.7).

$$\frac{u_H}{\theta_M} = \frac{1}{R}\frac{F_4}{F_3} \tag{4.18}$$

and

$$\frac{u_H}{u_{Vedge}} = \frac{F_4}{F_3} \tag{4.19}$$

The ratios u_{Vedge}/u_H (horizontal loading) and u_H/u_{Vedge} (moment loading) are included in Table 4.2. These results show a significant coupling between u_{Vedge} (θ_M) and u_H for low values of Poisson's ratio and no coupling as $\nu = 0.5$, applicable to undrained clay, is approached. For values of Poisson's ratio representative of a drained sand, $\nu \approx 0.2$, the ratios u_{Vedge}/u_H and u_H/u_{Vedge} are in the range 12-15%.

These results can be interpreted as follows. A horizontally loaded footing on drained sand will elastically rotate about a horizontal axis perpendicular to the direction of the applied load, and the corresponding maximum vertical edge displacement in this plane will typically be about 15% of the total horizontal displacement. As demonstrated in Section 4.2, current elastic solutions do not take into account this cross coupling, which is additive for the case when the moment arises from a horizontal load applied at some distance above the footing, as is applicable to offshore foundations. However, by comparison with the errors involved in determining representative elastic soil parameters, this cross coupling effect is thought not to be significant in most cases for a surface footing. Therefore the following comparisons of numerical and analytical elastic solutions for moment and horizontal loading of a rough surface footing do not take the cross coupling into account.

The numerical results for a rough footing subjected to moment loading are also presented in Figure 4.2. These results are expressed as $M/(GR^3\theta_M) = 1/F_3$ since the derivation of the analytical solutions is intended in a flexibility sense (Section 4.2). The difference in response between the smooth and rough footings varies from 13% for $\nu = 0.0$ to zero for undrained conditions, $\nu = 0.5$. This difference represents the error associated with modelling the response of a rough footing, subjected to moment loading, using the smooth analytical solution of Equation (4.2).

For a rough footing loaded horizontally, the numerical solution relating the horizontal load (H) to the horizontal displacement (u_H) is given in Figure 4.3 and compared with two approximate analytical solutions. The results are expressed in terms of the non-dimensional parameter

$H/(GRu_H) = 1/F_2$. Any comparison should take into account the observed errors between the finite element and exact solutions for the vertical and moment loading cases considered previously (Figures 4.1 and 4.2). It is therefore concluded that the Gerrard and Harrison (1970) solution (Equation 4.9), although approximate, provides a very good estimate of the true response for the full range of Poisson's ratio considered. The Bycroft (1956) solution (Equation 4.8) is seen to provide a poorer estimate for values of Poisson's ratio considerably less than 0.5.

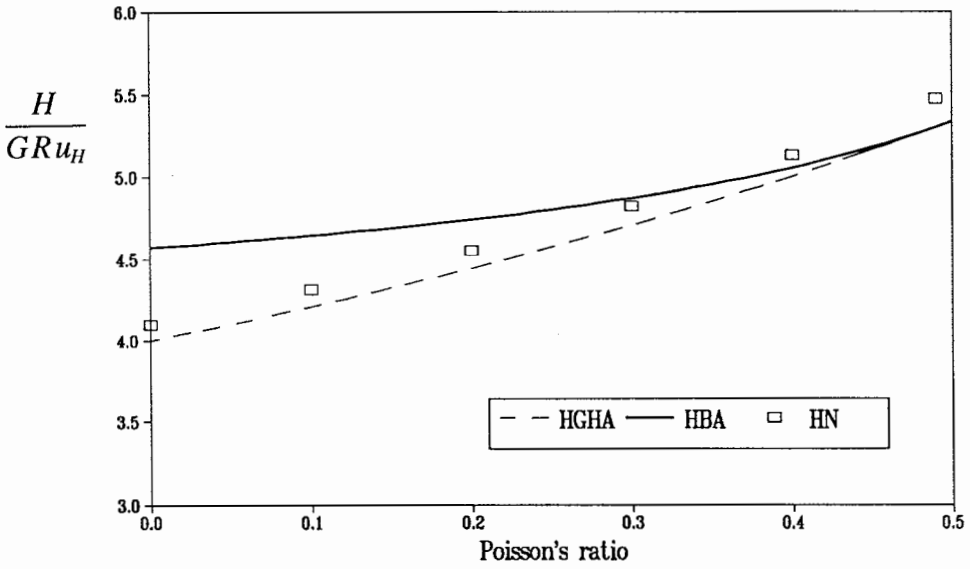

HGHA: Gerrard and Harrison (1970) analytical solution (Equation 4.9)
HBA: Bycroft (1956) analytical solution (Equation 4.8)
HN: Numerical solution (= $1/F_2$)

Figure 4.3: Results of elastic horizontal loading analyses of a surface footing.

4.4 Analytical Embedded Footing Solutions

Most of the available elastic solutions refer to footings placed at the ground surface, as examined in Section 4.2. Solutions that take the effect of embedment into account generally only consider the vertical displacement (settlement). The only known analytical elastic solution which describes the combined loading of an embedded rigid circular footing is provided by Gerrard (1980). He considers the more complex problem of generalised circular loads applied within a cross anisotropic medium. Simplification to a rigid footing case in an isotropic medium is possible, but will not result in a closed-form solution as occurs for the surface loading case (Gerrard and Harrison, 1970). The embedded footing solutions of Gerrard (1980) are expressed

in terms of summations of Gauss's hypergeometric functions, like functions, and trigonometric functions. Further examination of these solutions would need to be computer based and therefore is considered inappropriate.

Because of the difficulty in assessing the effect of embedment on elastic stiffness, the vertical loading problem has generally been simplified to empirical reduction factors applied to the settlement of an equivalent surface foundation. The most recent solution of this type for a rigid footing embedded in an elastic half-space is given by Gazetas *et al* (1985). Based on curve fitting of data from numerous analytical and numerical studies, they develop an analytical expression for estimating the elastic vertical settlement (u_{Vemb}) of an arbitrarily shaped embedded rigid foundation. The expression is given in the form

$$u_{Vemb} = u_{Vsurf} \cdot \mu_{trench} \cdot \mu_{wall} \tag{4.20}$$

where u_{Vsurf} is the vertical settlement of an equivalent surface footing, μ_{trench} is the reduction in settlement for a footing embedded in a trench (with no side wall contact), and μ_{wall} is the further reduction in settlement due to part of the applied load being transmitted to the ground through shear tractions acting along the vertical sides of the footing wall. Each of these parameters is given below and simplified to the special case of a circular footing. Gazetas *et al* (1985) derive Equation (4.20) for Poisson's ratio (ν) ranging from 0.25 to 0.49, depths of embedment (z_D) to $2.5R$, and claim the equation error is in most cases less than 10%.

The vertical settlement of an arbitrarily shaped rigid surface footing (u_{Vsurf}) is given as

$$u_{Vsurf} = 0.45\left(\frac{A_b}{2L.2B}\right)^{-0.38}\frac{(1-\nu)}{2GL}V \tag{4.21}$$

where A_b is the plan area of the foundation-soil contact surface, and $2L$ and $2B$ are the length and width of the rectangle circumscribed to the actual contact surface. For a circular footing, L and B are set equal to R and the expression becomes

$$u_{Vsurf} = 0.99\left[\frac{(1-\nu)}{4GR}\right]V \tag{4.22}$$

Hence the surface footing vertical settlement has algebraically the same form as that for a smooth footing (Equation 4.1), differing in magnitude by only 1%.

The factor μ_{trench}, which makes an allowance for the reduction in settlement for a footing embedded in a trench with no sidewall contact (Figure 4.4a), is given as

$$\mu_{trench} = 1 - 0.04\frac{z_D}{B}\left(1 + \frac{4}{3}.\frac{A_b}{2L.2B}\right) \tag{4.23}$$

where all parameters are as defined previously. Equation (4.23) suggests that when there is no sidewall contact, the settlement decreases linearly with footing embedment and this linear relationship is independent of ν. For a circular footing, this equation reduces to

$$\mu_{trench} = 1 - 0.08\frac{z_D}{R} \tag{4.24}$$

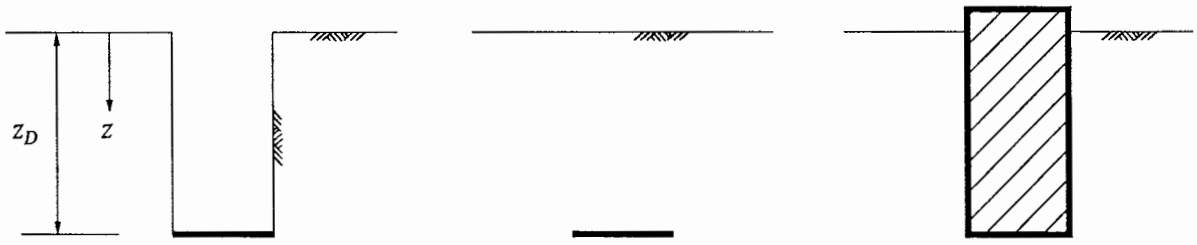

(a) Case 1 (b) Case 2 (c) Case 3

Figure 4.4: Cases of elastic embedment examined for a rigid rough circular footing: (a) Case 1 - Bottom of a trench, (b) Case 2 - Covered footing, (c) Case 3 - Full sidewall contact

The further reduction in settlement due to sidewall contact, represented by the reduction factor μ_{wall}, is given by Gazetas *et al* (1985) as

$$\mu_{wall} = 1 - 0.16\left(\frac{A_w}{A_b}\right)^{0.54} \tag{4.25}$$

where A_w is the area of the sidewall-soil interface. This factor varies non-linearly with depth and like μ_{trench} is taken to be independent of ν. For the cases of embedded footing geometry numerically examined in the following section, it is assumed that if sidewall contact exists, it exists for the full depth of embedment (Figure 4.4c). Equation (4.25) for a cylindrical footing therefore simplifies to

$$\mu_{wall} = 1 - 0.23\left(\frac{z_D}{R}\right)^{0.54} \tag{4.26}$$

4.5 Numerical Embedded Footing Solutions

4.5.1 Cases of embedment examined

The geometry and boundary conditions of footing embedment can vary greatly with the application considered and therefore a comprehensive analysis of all of the possibilities is not feasible. This study examines three cases of embedment, as illustrated in Figure 4.4, which are considered particularly relevant to offshore foundations. The first case, applicable to spudcan footings, is that of a rigid circular footing at the bottom of a trench (Figure 4.4a), where no significant sidewall-soil contact exists. However, it is quite common for the trench walls to collapse in on top of the spudcan and therefore the second case examines an embedded covered footing (Figure 4.4b). The third set of embedment boundary conditions considered, given in Figure 4.4c, is an embedded footing with full sidewall-soil contact. This is appropriate for mudmats and gravity foundations where skirts are used to embed the effective base beneath the surface.

All footing-soil interfaces in this section are assumed to be perfectly rough. This is considered appropriate as most offshore foundation surfaces have a roughened texture. Furthermore, based on the surface footing results in Sections 4.2 and 4.3, there is probably at the most a 10% difference in vertical stiffness between smooth and rough embedded footings.

4.5.2 Results

For the three cases of footing embedment, Table 4.3 presents the results of an elastic study into the effect of footing embedment under combined loading conditions. The study encompasses embedment depths of z_D/R = 0.0, 0.5, 1.0, 2.0 and 4.0 and Poisson's ratio values of 0.0, 0.2, 0.4 and 0.49, these values adequately covering most applications of offshore foundations. The finite

element meshes analysed for $z_D/R = 2.0$ (all three cases) are presented in Figure 4.5 and typify the meshes used in the analysis of other embedment depths. Note that the meshes for cases 1 and 3 are the same, except for the number of nodes restrained to represent the footing geometry. The embedded footing meshes adopt effectively the same mesh dimensions and topology as the surface footing mesh (Figure 3.7). The radial and vertical mesh dimensions are $200R$ and $(200R + z_D)$ with the footing level situated at a height of $200R$ above the mesh base.

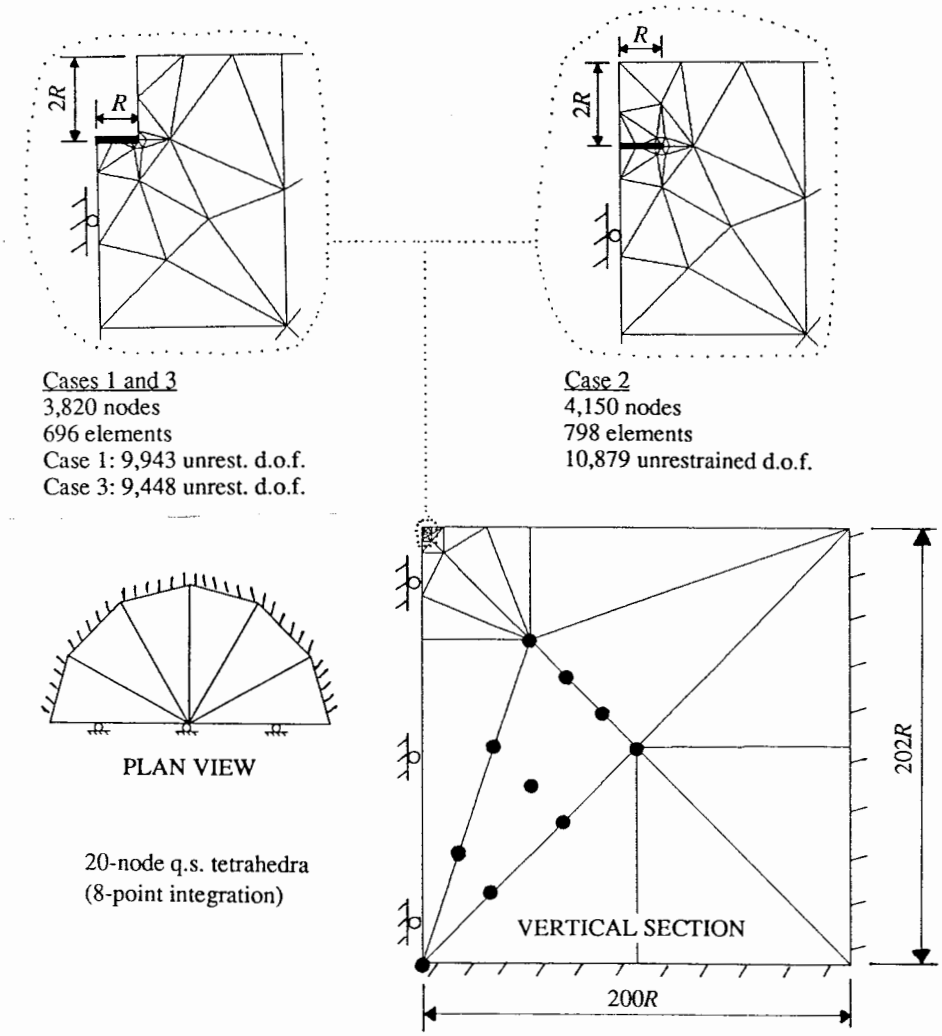

Figure 4.5: For the three cases of embedment examined, 20-node tetrahedron meshes for the elastic analysis of a footing embedded 2.0R.

The results of Table 4.3 are given in terms of the stiffness coefficients K_1, K_2, K_3, K_4, defined earlier in Equation (4.5). These coefficients correspond to the base of the footing (at depth z_D), and were computed by analysing the problems of rigid vertical displacement (to give K_1), rigid horizontal displacement (to give K_2 and K_4), and rigid footing rotation about the base (to give

K_3 and K_4). The procedure used in evaluating these coefficients is given in more detail in Section 4.2. The equivalent flexibility coefficients can be obtained by substituting K_1-K_4 into Equation (4.7). The surface footing stiffness coefficients in Table 4.3 are taken from the numerical analyses of Section 4.3, while the accompanying values in brackets correspond to known exact analytical values (Section 4.2).

The coefficients K_1-K_4 in Table 4.3 use the intersection of the footing base and centre-line as the point of reference, that is, all values are computed at this point. These stiffness coefficients, however, are dependent on the reference point adopted. Varying the position of this point vertically along the footing centre-line affects the horizontal displacement and footing moment, while all other loads and displacements remain unchanged. For a footing base located at a depth z_D, the stiffness matrix ($[\mathbf{K}^z]$) corresponding to a depth z can be shown to be

$$[\mathbf{K}^z] = \begin{bmatrix} K_1^z & 0 & 0 \\ 0 & K_2^z & K_4^z \\ 0 & K_4^z & K_3^z \end{bmatrix} \tag{4.27}$$

where the new stiffness coefficients are written in terms of the values at the base of the footing as follows

$$K_1^z = K_1 \tag{4.28}$$

$$K_2^z = K_2 \tag{4.29}$$

$$K_3^z = K_2\left(\frac{z_D}{R} - \frac{z}{R}\right)^2 - 2K_4\left(\frac{z_D}{R} - \frac{z}{R}\right) + K_3 \tag{4.30}$$

$$K_4^z = K_4 - K_2\left(\frac{z_D}{R} - \frac{z}{R}\right) \tag{4.31}$$

Note that in this transformation the vertical (K_1) and horizontal (K_2) stiffnesses are unaltered while the moment (K_3) and cross coupling (K_4) stiffness coefficients change. One particular reference point which is commonly used in structural analyses is the surface (or seabed) level ($z = 0$). In this case, Equations (4.30) and (4.31) reduce to

Table 4.3: Elastic footing results for three cases of embedment

(a) $\nu = 0.0$

Case[1]	$\frac{z_D}{R}$	Base of footing				Surface[2]		Metacentre[3]	
		K_1	K_2	K_3	K_4	K_3^s	K_4^s	z_m/R	K_3^m
Surface	0.0	4.507 (4.394)	4.271	3.227	-0.7364	3.227	-0.7364	0.1724	3.100
1	0.5	5.167	5.702	4.117	-0.9582	6.501	-3.809	0.6680	3.956
	1.0	5.748	6.154	4.624	-1.023	12.824	-7.177	1.1662	4.454
	2.0	6.412	6.458	4.855	-1.048	34.879	-13.964	2.1623	4.685
	4.0	7.154	6.889	5.055	-1.0832	123.945	-28.639	4.1572	4.885
2	0.5	5.49	6.367	5.112	-0.4546	7.158	-3.638	0.5714	5.080
	1.0	6.345	7.312	6.361	-0.2009	14.075	-7.513	1.0275	6.355
	2.0	7.655	8.181	7.18	-0.0562	40.129	-16.418	2.0069	7.180
	4.0	9.003	8.784	7.471	-0.0146	148.132	-35.151	4.0017	7.471
3	0.5	6.137	6.924	7.233	0.1099	8.854	-3.3521	0.4841	7.231
	1.0	7.303	8.774	12.882	1.836	17.984	-6.938	0.7907	12.498
	2.0	9.416	11.913	33.62	7.303	52.060	-16.523	1.3870	29.143
	4.0	13.147	17.198	129.31	25.266	202.350	-43.526	2.5309	92.191

(b) $\nu = 0.2$

Case[1]	$\frac{z_D}{R}$	Base of footing				Surface[2]		Metacentre[3]	
		K_1	K_2	K_3	K_4	K_3^s	K_4^s	z_m/R	K_3^m
Surface	0.0	5.388 (5.256)	4.639	3.716	-0.5682	3.716	-0.5682	0.1225	3.646
1	0.5	5.983	6.127	4.574	-0.8258	6.932	-3.889	0.6348	4.463
	1.0	6.553	6.588	5.111	-0.9256	13.550	-7.514	1.1405	4.981
	2.0	7.228	6.883	5.395	-0.9885	36.881	-14.755	2.1436	5.253
	4.0	8.014	7.317	5.645	-1.0558	131.163	-30.324	4.1443	5.493
2	0.5	6.354	6.844	5.629	-0.2518	7.592	-3.674	0.5368	5.620
	1.0	7.232	7.775	6.937	-0.0404	14.793	-7.815	1.0052	6.937
	2.0	8.574	8.61	7.836	0.0166	42.210	-17.203	1.9981	7.836
	4.0	9.983	9.185	8.191	0.007	155.095	-36.733	3.9992	8.191
3	0.5	7.061	7.537	7.95	0.5279	9.306	-3.2406	0.4300	7.913
	1.0	8.292	9.548	14.126	2.54	18.594	-7.008	0.7340	13.450
	2.0	10.539	12.961	37.053	8.741	53.933	-17.181	1.3256	31.158
	4.0	14.495	18.694	142.747	28.796	211.483	-45.98	2.4596	98.390

(Table 4.3 continued)

(c) $\nu = 0.4$

Case[1]	$\frac{z_D}{R}$	Base of footing				Surface[2]		Metacentre[3]	
		K_1	K_2	K_3	K_4	K_3^s	K_4^s	z_m/R	K_3^m
Surface	0.0	6.925 (6.729)	5.145	4.628	-0.259	4.628	-0.259	0.0503	4.615
1	0.5	7.472	6.732	5.506	-0.5643	7.753	-3.930	0.5838	5.459
	1.0	8.049	7.252	6.116	-0.7189	14.806	-7.971	1.0991	6.045
	2.0	8.775	7.585	6.511	-0.8486	40.245	-16.019	2.1119	6.416
	4.0	9.73	8.056	6.916	-0.995	143.772	-33.219	4.1235	6.793
2	0.5	7.863	7.479	6.623	0.0745	8.418	-3.665	0.4900	6.622
	1.0	8.779	8.405	8.119	0.2252	16.074	-8.180	0.9732	8.113
	2.0	10.254	9.253	9.265	0.1435	45.703	-18.363	1.9845	9.263
	4.0	11.909	9.851	9.823	0.0423	167.101	-39.362	3.9957	9.823
3	0.5	8.58	8.413	9.15	1.1664	10.087	-3.0401	0.3614	8.988
	1.0	9.888	10.665	16.124	3.58	19.629	-7.085	0.6643	14.922
	2.0	12.336	14.534	42.59	10.847	57.338	-18.221	1.2537	34.495
	4.0	16.574	21.012	163.288	33.953	227.856	-50.095	2.3841	108.424

(d) $\nu = 0.49$

Case[1]	$\frac{z_D}{R}$	Base of footing				Surface[2]		Metacentre[3]	
		K_1	K_2	K_3	K_4	K_3^s	K_4^s	z_m/R	K_3^m
Surface	0.0	8.151 (8.000)	5.474 (5.333)	5.41 (5.333)	-0.0144 (0.00)	5.41 (5.333)	-0.0144 (0.00)	0.0026 (0.00)	5.410 (5.333)
1	0.5	8.745	7.186	6.39	-0.3346	8.521	-3.928	0.5466	6.374
	1.0	9.387	7.835	7.136	-0.5305	16.032	-8.366	1.0677	7.100
	2.0	10.172	8.237	7.605	-0.7042	43.370	-17.178	2.0855	7.545
	4.0	11.388	8.688	8.26	-0.9486	154.857	-35.701	4.1092	8.156
2	0.5	9.112	7.906	7.537	0.319	9.195	-3.634	0.4597	7.524
	1.0	10.085	8.854	9.273	0.4432	17.241	-8.411	0.9499	9.251
	2.0	11.743	9.761	10.727	0.2592	48.734	-19.263	1.9734	10.720
	4.0	13.743	10.427	11.603	0.0683	177.889	-41.640	3.9934	11.603
3	0.5	9.767	9.041	10.139	1.577	10.822	-2.9435	0.3256	9.864
	1.0	11.119	11.488	17.757	4.281	20.683	-7.207	0.6274	16.162
	2.0	13.74	15.8	47.49	12.361	61.246	-19.239	1.2177	37.819
	4.0	18.148	22.944	179.971	37.779	244.843	-53.997	2.3534	117.765

(Table 4.3 continued)

Notes:

1. Refer to Figure 4.4 for the embedded cases examined.
2. Coefficients K_3^s and K_4^s given by Equations (4.32) and (4.33) respectively.
3. z_m and K_3^m given by Equations (4.34) and (4.35) respectively.
4. Values in brackets for the surface footing correspond to exact analytical quantities. In Table 4.3d ($\nu = 0.49$) the exact values are for $\nu = 0.5$.

$$K_3^s = K_2\left(\frac{z_D}{R}\right)^2 - 2K_4\left(\frac{z_D}{R}\right) + K_3 \tag{4.32}$$

$$K_4^s = K_4 - K_2\left(\frac{z_D}{R}\right) \tag{4.33}$$

where the superscript s denotes the surface level. The stiffness coefficients of Equations (4.32) and (4.33) are included in Table 4.3. The other point of reference which is of particular physical significance is where the stiffness matrix ($[\mathbf{K}^z]$) becomes diagonal. This point is termed the *metacentre* and is characterised by the uncoupling of the horizontal and moment components, that is, a moment applied at the metacentre will not produce any horizontal translation at that point. Substituting $K_4^z = 0$ into Equation (4.31) and rearranging gives the depth of the metacentre (z_m) to be

$$\frac{z_m}{R} = \frac{z_D}{R} - \frac{K_4}{K_2} \tag{4.34}$$

Noting that K_2 is always positive, Equation (4.34) establishes that if the coupling stiffness K_4 is positive, the metacentre is located below the footing base, if K_4 is negative, the metacentre is below the base, and if it is zero, the metacentre is at the base. The metacentre depth is included in Table 4.3 together with the moment stiffness at the metacentre K_3^m, as given below

$$K_3^m = K_3 - \frac{K_4^2}{K_2} \tag{4.35}$$

4.5.3 Comparison with available solutions for vertical loading

Section 4.4 revealed that readily available and usable solutions for embedded footings only exist for the vertical loading case. Therefore the following comparisons of the numerical results (Table 4.3) with alternative solutions is only performed for this case.

For a footing located at the bottom of a trench (Case 1), the ratio of the vertical stiffness of the footing (K_{1emb}) to the vertical stiffness of an equivalent surface footing (K_{1surf}) is plotted against the depth of embedment in Figure 4.6. Presenting the results as the ratio K_{1emb}/K_{1surf} represents the reduction in footing settlement due to embedment and has the advantage that the ratio removes many of the discretisation errors inherent in the finite element method. It also allows easy comparison of the numerical results with the empirical solution of Gazetas *et al* (1985), given in Equation (4.20) and discussed in Section 4.4. This equation is rewritten below in terms of the vertical stiffness ratio K_{1emb}/K_{1surf}

$$\frac{K_{1emb}}{K_{1surf}} = \frac{u_{Vsurf}}{u_{Vemb}} = \frac{1}{\mu_{trench}\mu_{wall}} \tag{4.36}$$

and is included in Figure 4.6 for Case 1 ($\mu_{wall} = 1.0$). Figure 4.6 shows the Gazetas et al (1985) solution, which is assumed to be independent of Poisson's ratio (ν), compares poorly with the numerical solutions, which demonstrate the increase in vertical embedment stiffness to be significantly dependent on ν. The finite element results also demonstrate that the incremental increase in vertical stiffness becomes smaller with embedment depth, as would be expected.

Butterfield and Banerjee (1971)[1] present boundary element solutions for a vertically loaded rigid circular footing embedded below the surface of an isotropic homogeneous half-space for values of $\nu = 0.0$, 0.3 and 0.5. The boundary conditions are equivalent to Case 2, a covered footing, except that the footing surface is assumed to be smooth, while in this study it is taken to be rough. The Butterfield and Banerjee (1971) solution demonstrate that with deep embedment the ratio K_{1emb}/K_{1surf} approaches constant values of about 2.5 and 2 for $\nu = 0$ and 0.5 respectively, and that a large proportion of the embedment effect is generated by a depth of $8R$. For the embedment depth range examined in this study, these solutions are compared in Figure 4.7 with the finite element solutions for a covered footing. In general, the two sets of solutions compare

1 Also given in Poulos and Davis (1974).

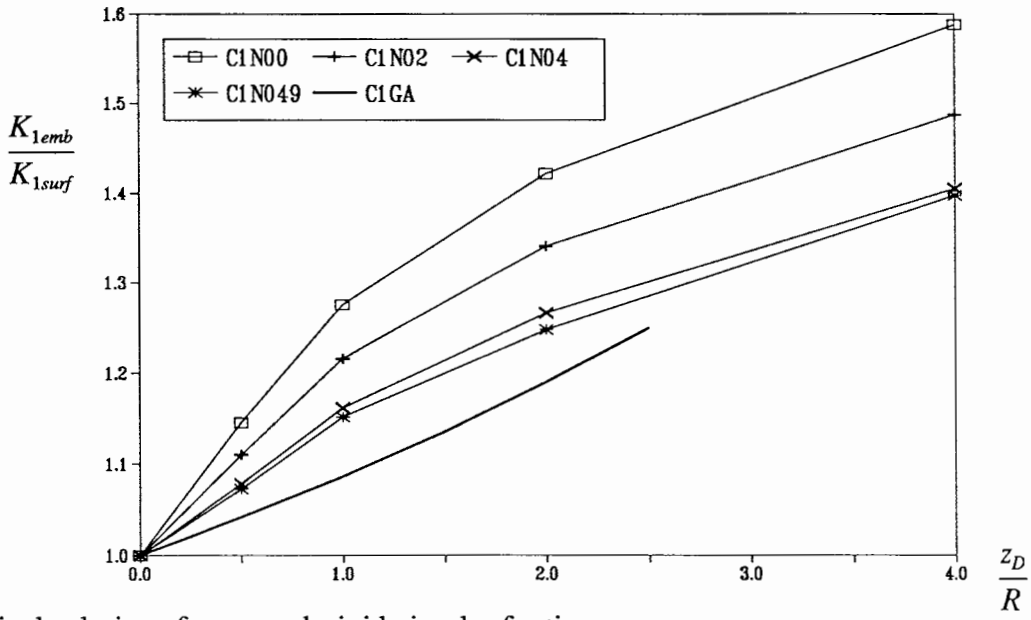

Numerical solutions for a rough rigid circular footing:
C1N00: $\nu = 0.0$ C1N02: $\nu = 0.2$ C1N04: $\nu = 0.4$ C1N049: $\nu = 0.49$
C1GA: Gazetas *et al* (1985) empirical analytical solution (Equation 4.36 for $\mu_{wall} = 1.0$)

Figure 4.6: The increase in vertical stiffness due to embedment for a footing at the bottom of a trench (Case 1).

well. For $\nu = 0.0$, the 10% difference in the curves is attributed to the differing smooth and rough boundary conditions. The solutions are much closer under incompressible soil conditions ($\nu \approx 0.5$). This is as anticipated since the vertical stiffnesses of rough and smooth surface footings are the same when $\nu = 0.5$ (Figure 4.1).

The Gazetas *et al* (1985) solution is also applicable to the problem of an embedded footing with full sidewall contact (Case 3). As for Figure 4.6, this solution, expressed as the stiffness ratio K_{1emb}/K_{1surf} (Equation 4.36), is compared with the numerical results in Figure 4.8. The finite element solution shows the increase in embedment stiffness to be dependent on ν and that the Gazetas *et al* (1985) solution agrees closely with this for $z_D/R = 0.0 - 2.5$ and $\nu = 0.4$. This is a promising result as the Gazetas *et al* (1985) solution is intended for Poisson's ratio values in the range 0.25 to 0.5.

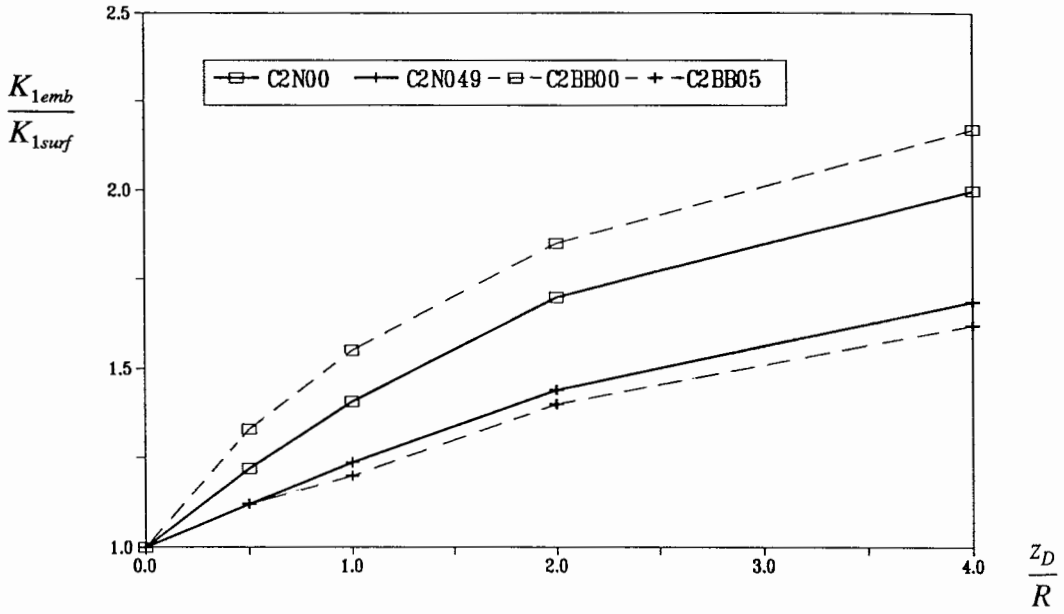

Numerical solutions for a rough rigid circular footing:
C2N00: $\nu = 0.0$ C2N049: $\nu = 0.49$
Butterfield and Banerjee (1971) numerical solution for a smooth rigid circular footing:
C2BB00: $\nu = 0.0$ C2BB05: $\nu = 0.5$

Figure 4.7: The increase in vertical stiffness due to embedment for a covered footing (Case 2).

4.5.4 Further examination of results

Where the previous sub-section made comparisons with available solutions, this sub-section concentrates on the comparative performance of the three cases of footing embedment for all three cases of combined loading. The ratio of embedment to surface vertical stiffness (K_{1emb}/K_{1surf}) is plotted against embedment depth in Figure 4.9 for $\nu = 0.0$ and 0.49. These values of Poisson's ratio represent the upper and lower limits for the full range of possible K_{1emb}/K_{1surf} values. For a given depth of embedment and Poisson's ratio, Figure 4.9 shows that the footing with full sidewall contact (Case 3) has a greater increase in vertical stiffness (greater reduction in vertical displacement) than a covered footing (Case 2). Similarly a covered footing has a greater stiffness than a footing at the bottom of a trench (Case 1). The three sets of footing embedments presented in Figure 4.9 cover a wide range of stiffness values and provide scope for extrapolation to other embedded footing boundary conditions not examined in this study.

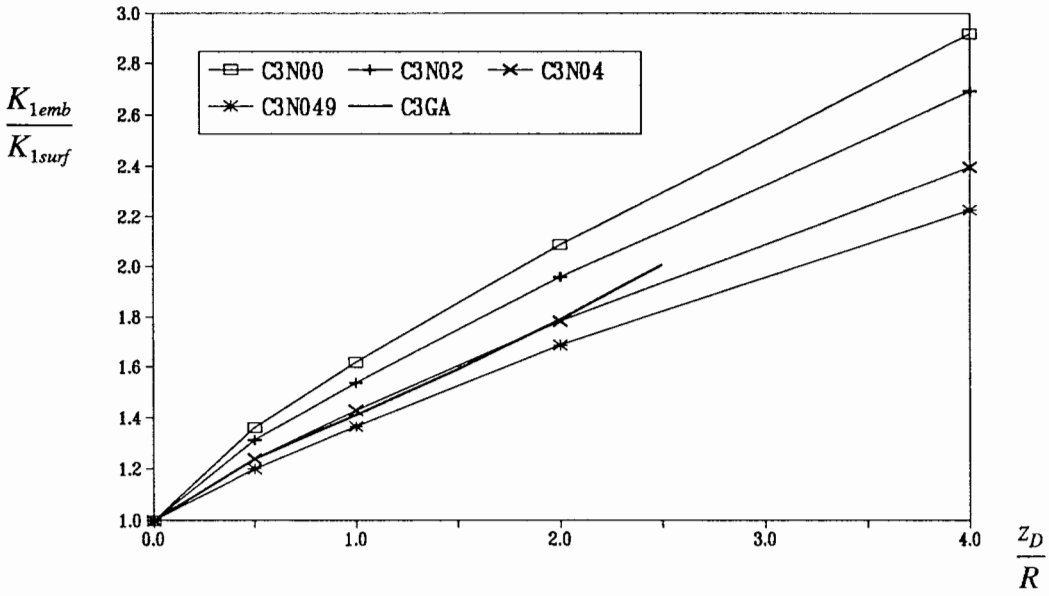

Numerical solutions for a rough rigid circular footing:
C3N00: $\nu = 0.0$ C3N02: $\nu = 0.2$ C3N04: $\nu = 0.4$ C3N049: $\nu = 0.49$
C3GA: Gazetas *et al* (1985) empirical analytical solution (Equation 4.36)

Figure 4.8: The increase in vertical stiffness due to embedment for a footing with full sidewall contact (Case 3).

Cases 1 and 2 in Figure 4.9 suggest that the increase in vertical stiffness due to embedment reaches a constant value with sufficient embedment, this result being consistent with that observed by Butterfield and Banerjee (1971), as discussed previously. Case 3, however, shows a different trend. The increase in vertical stiffness approaches a constant gradient with embedment depth, rather than a constant value. This is a consequence of the sidewall-soil contact area increasing with embedment depth and emphasises the benefits of sidewall contact.

For all three cases of embedment, the ratio of embedment to surface vertical stiffness is significantly dependent on Poisson's ratio (Figure 4.9). However, this ratio for horizontal stiffness (K_{2emb}/K_{2surf}) is demonstrated in Figure 4.10 to be much less dependent on Poisson's ratio. The trends in the three sets of curves are very similar to those observed in Figure 4.9 for vertical stiffness. However, one major difference is that the magnitude of the increase in stiffness for Case 3 is greater for horizontal loading than vertical loading. For example, at $z_D/R = 4.0$ the ratio K_{2emb}/K_{2surf} is about 4, while K_{1emb}/K_{1surf} is in the range 2.3 to 2.9.

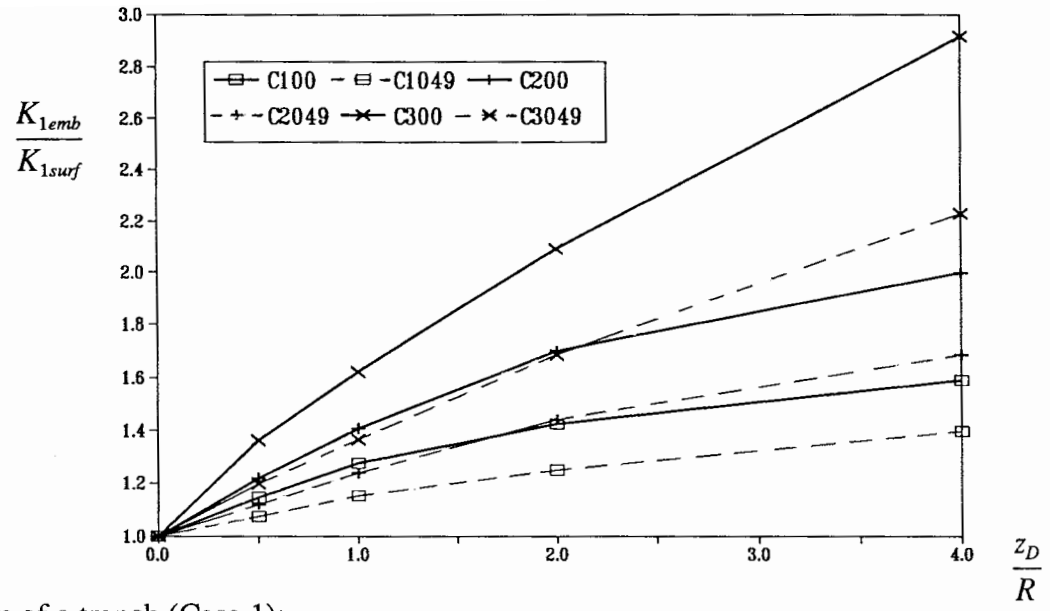

Bottom of a trench (Case 1):
C100: $\nu = 0.0$ C1049: $\nu = 0.49$
Covered footing (Case 2):
C200: $\nu = 0.0$ C2049: $\nu = 0.49$
Full sidewall contact (Case 3):
C300: $\nu = 0.0$ C3049: $\nu = 0.49$

Figure 4.9: The increase in vertical stiffness due to embedment for the three cases examined.

Examination of the effect of embedment on the moment stiffness is not straightforward due to the cross coupling of the stiffness matrix (Equation 4.5) for horizontal and moment loading. As detailed in sub-section 4.5.2, the moment stiffness (K_3) changes with the reference point adopted. To remove the complications of cross coupling, the moment stiffness is examined at the metacentre (K_3^m) where the cross coupling stiffness coefficient K_4 is zero, that is, the stiffness matrix is diagonal. Figure 4.11 presents the ratio K_{3emb}^m/K_{3surf}^m in the same format as adopted in Figures 4.9 and 4.10. For offshore foundations, where the foundation moment is generated by environmental (horizontal) loads acting over the depth of the water, the ratio K_{3emb}^m/K_{3surf}^m is representative of the reduction in footing rotation due to embedment. This presumption, however, is dependent on the depth of the water being significantly greater than the depth of the metacentre, which in most applications would be the case.

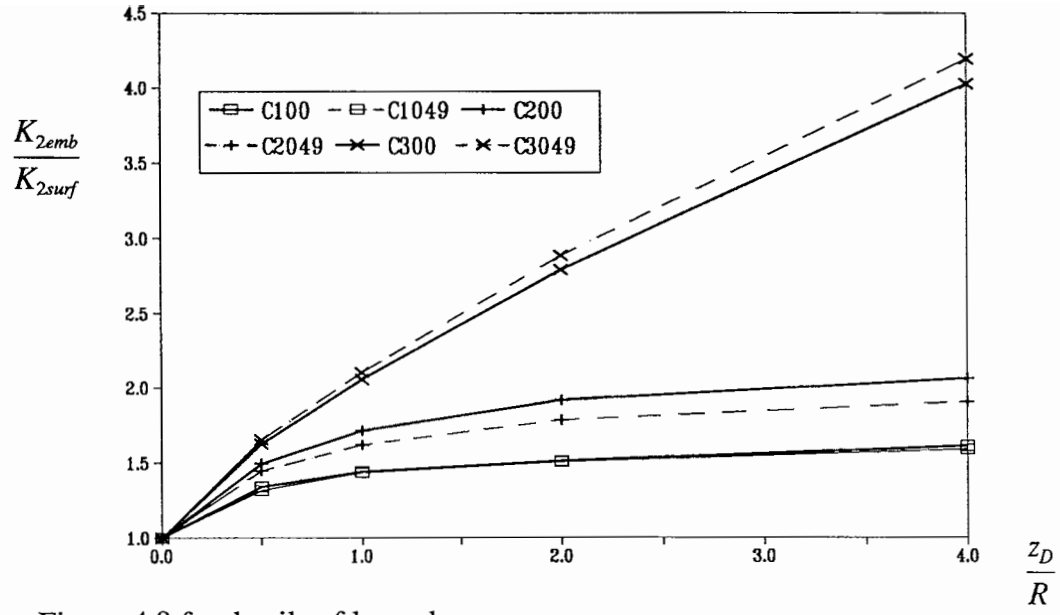

Refer to Figure 4.9 for details of legend

Figure 4.10: The increase in horizontal stiffness due to embedment for the three cases examined.

Figure 4.11 shows the ratio K^m_{3emb}/K^m_{3surf} for cases 1 and 2 to approach a constant value in a similar fashion to that observed for horizontal loading. For a footing with full sidewall contact (Case 3), K^m_{3emb}/K^m_{3surf} is observed to increase quadratically with footing embedment. That is, at $z_D/R = 1.0$, the increase in moment stiffness is shown to be in the range 3.0 to 4.0, where by a depth of $z_D/R = 4.0$, these values have grown to 21.8 and 29.7. For an offshore foundation of this type, this has important implications as only a small degree of embedment will produce a substantial reduction in elastic footing rotation.

An overall comparison of Figures 4.9, 4.10 and 4.11 illustrates the effect of embedment on vertical, horizontal and moment stiffnesses (and therefore deformations) to be very comparable for Cases 1 and 2. By an embedment depth of $z_D = 4.0R$, the ratio of embedment stiffness to surface stiffness has reached values in the ranges 1.4-1.6 and 1.7-2.3 for Cases 1 and 2 respectively. The effect of footing embedment on elastic stiffness is observed at shallow depths for the horizontal and moment cases, with a large proportion of the final constant value being reached by a depth of $2R$. The vertical stiffness, on the other hand, is still showing signs of significant increase at $z_D = 4.0R$, particularly for Case 2. Due to the sidewall-soil contact associated with Case 3, this has shown the largest increases in embedment elastic stiffness. As

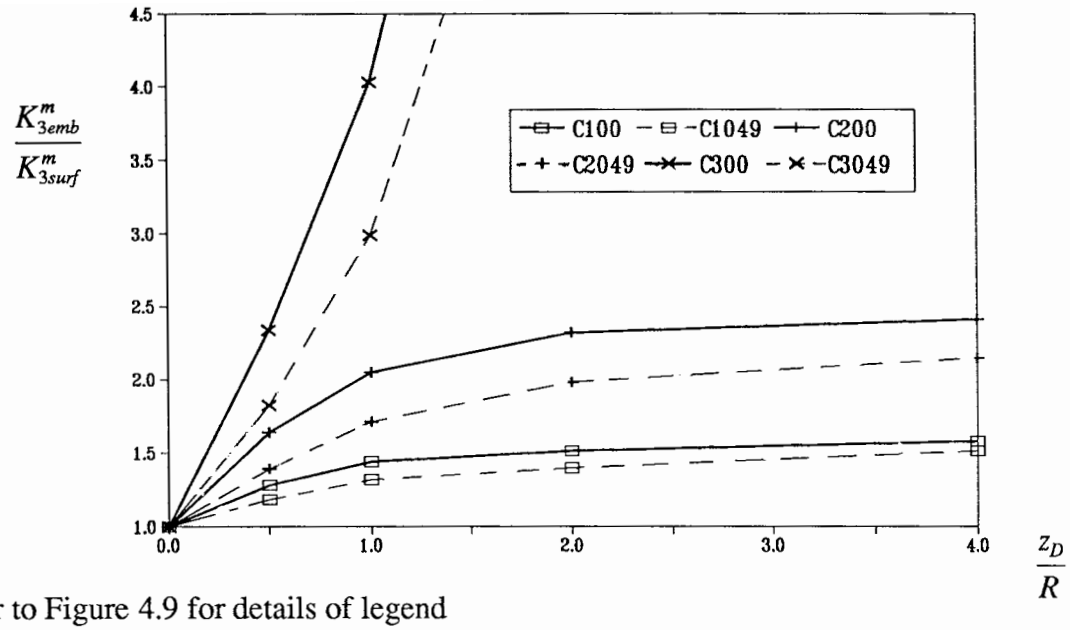

Refer to Figure 4.9 for details of legend

Figure 4.11: The increase in moment stiffness at the metacentre due to embedment for the three cases examined.

for Cases 1 and 2, the influence of embedment on footing stiffness is more localised to the surface for the horizontal and moment loading cases, with an appreciable increase in stiffness being developed by an embedment depth of one footing radius.

To gain a better physical understanding of the cross coupling effect, the metacentre depth (z_m), defined in Equation (4.34) and given in Table 4.3, is presented in Figure 4.12 for the three types of embedded footings considered and a Poisson's ratio of 0.2. In this figure, z_m/R is plotted against the embedment depth (z_D/R) and includes the one to one relationship for these two variables. For a surface footing ($z_D = 0$), the metacentre is shown in Figure 4.12 to be located at a depth of $0.123R$ below the footing. In the case of an incompressible soil ($\nu = 0.5$), the metacentre is situated at the footing base (Table 4.3). The influence of Poisson's ratio on metacentre depth, however, is not included in Figure 4.12 as the general behaviour of the three sets of curves is unchanged with this variable.

The metacentre for Case 1, a footing at the bottom of a trench, is situated just below the footing base in a similar fashion to a surface footing on a compressible soil. Therefore the degree of cross coupling of the stiffness matrix is comparable with that demonstrated in Section 4.3 for a surface footing. Case 2, a covered footing, has no cross coupling by an embedment depth of

$z_D = R$, as the metacentre depth corresponds to the footing base. The metacentre for Case 3 exhibits the greatest deviation from the footing base for all three cases. With deep embedment, the metacentre depth tends towards a depth of about $0.6z_D$, that is, $0.4z_D$ above the footing base. In this case, adopting the footing base as the reference point for the evaluation of the stiffness coefficients will result in a strong cross coupling of the horizontal and moment components.

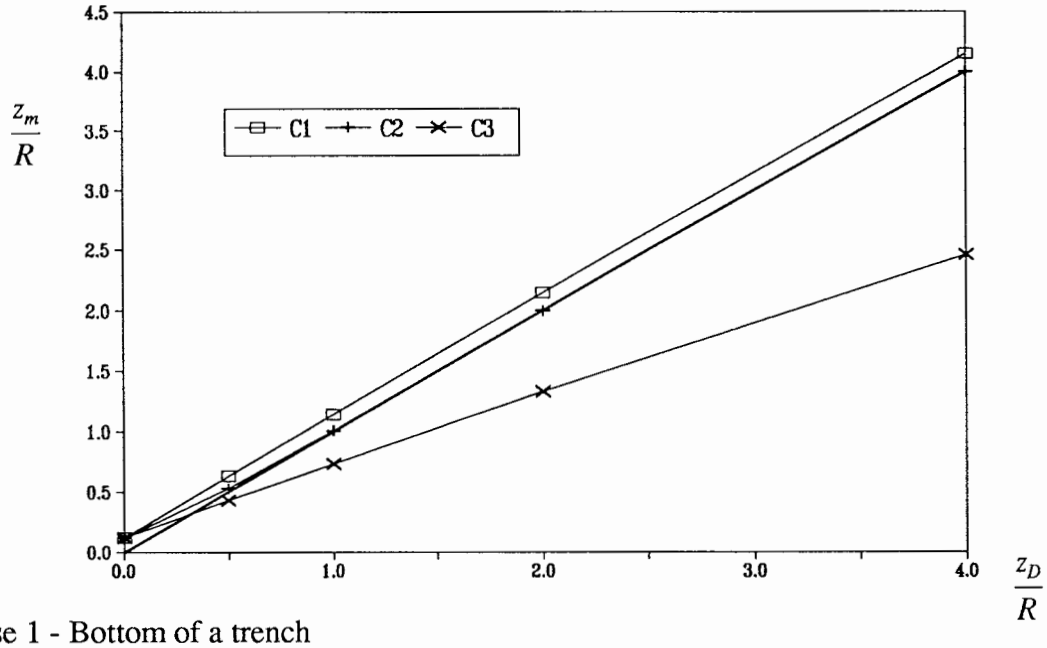

C1: Case 1 - Bottom of a trench
C2: Case 2 - Covered footing
C3: Case 3 - Full sidewall contact

Figure 4.12: Metacentre depth for the three cases of embedment examined and a Poisson's ratio of 0.2.

CHAPTER 5 STABILITY ANALYSIS OF A SURFACE FOOTING

5.1 Introduction

As a first step towards a comprehensive analysis of the stability of shallow offshore foundations, this chapter examines a rigid circular footing placed on the surface of an undrained saturated clay. The clay strength is defined by its undrained shear strength s_u, and the combined loading conditions are assumed to be monotonic. The choice of soil conditions is considered appropriate as many offshore foundations are situated in clayey soils which behave undrained due to the size of the foundation and the short period of the cyclic environmental loads. It is recognised that footing embedment and soil type/properties are key parameters in the overall stability problem, however, their examination is beyond the scope of this thesis.

This chapter commences with a review of existing bearing capacity (stability) solutions for the problem under consideration. This highlights the need for the development of interface elements to model the interaction between the footing base and the soil continuum. The application of interface elements results in a first attempt towards defining the failure envelope of a surface footing at high vertical load. The chapter concludes with a brief comparison of the computed failure envelope with the bearing capacity equations for the inclined (horizontal) loading case.

5.2 Bearing Capacity Solutions

5.2.1 Basis of existing solutions

The bearing capacity solutions of Meyerhof (1953), Brinch Hansen (1970) and Vesic (1975) have been most commonly used in the analysis of footings subjected to combined loading. All of these solutions are based on general shear failure where a clearly defined peak in strength occurs (Vesic, 1975; Craig, 1987). This case can be mathematically modelled by the lower and upper bound theorems of plasticity. The basis of these equations is the solution for the vertical bearing capacity (q_V) of a surface strip foundation, which for a Tresca yield criterion is universally accepted as

$$q_V = \frac{V}{A} = (2+\pi)s_u \tag{5.1}$$

where V is the ultimate vertical load and A is the area of the footing. The extension of this solution to other geometries has been achieved in practice by using empirical *shape factors*. As illustrated in this section, the shape factor is generally taken to be about 1.2 for a circular footing. It seems unnecessary to adopt such a crude factor when solutions for the bearing capacity of a rigid circular footing on a Trecsa material have already been obtained. For smooth and rough footings, these are $5.69s_u$ (Shield, 1955) and $6.05s_u$ (Eason and Shield, 1960) respectively, and therefore indicate a more appropriate shape factor is in the range 1.11-1.18 (ie 5.69/5.14 - 6.05 5.14).

Combined vertical (V), horizontal (H) and moment (M) loading is taken into account by considering an equivalent single load of magnitude P, placed at an eccentricity eR, with an inclination to the vertical of α, as demonstrated in Figure 5.1 for a circular footing of radius R. The eccentricity of the load represents moment loading and is modelled in the bearing capacity solutions by adopting a reduced *effective contact area* (A'), which is dependent on the magnitude of the eccentricity. The inclination of load, representing horizontal loading, is accounted for by adopting an *inclination factor*, which is a dependent on α.

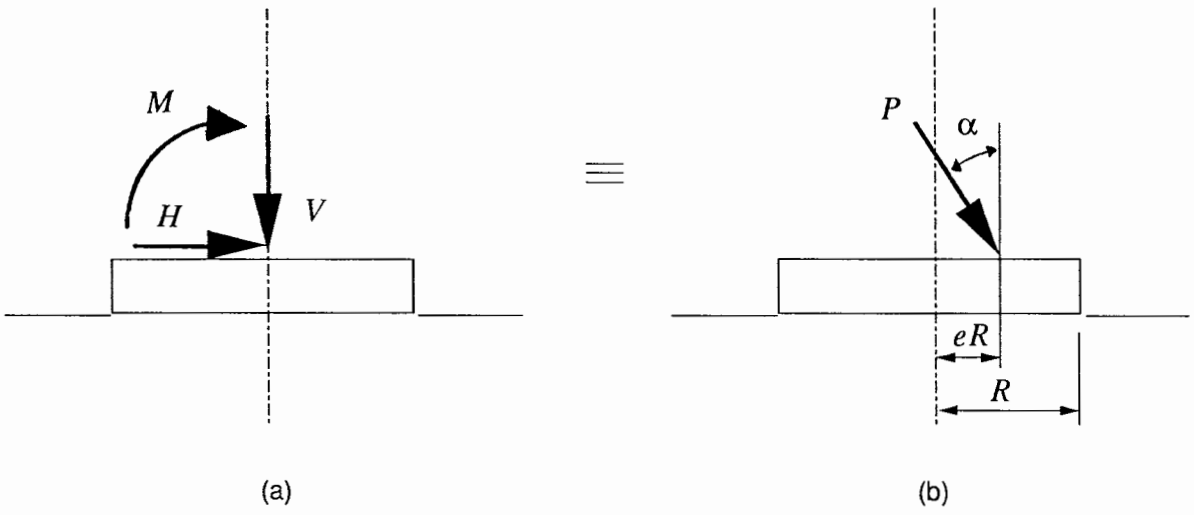

Figure 5.1: (a) Combined vertical, horizontal and moment loading, (b) Equivalent eccentric and inclined load.

The existing combined loading bearing capacity equations are generally expressed in terms of P (or V), α and e. However, they can similarly be expressed in terms of the ultimate combined loads V, H and M using the following relationships

$$V = P\cos\alpha \tag{5.2}$$

$$H = P\sin\alpha \tag{5.3}$$

$$M = eR\,.\,P\cos\alpha \tag{5.4}$$

5.2.2 Meyerhof solution

Meyerhof (1953), based on his earlier work on the ultimate vertical bearing capacity of shallow foundations (Meyerhof, 1951), extended his analysis to include eccentric and inclined loads. As a result of experimental model strip footing tests on cohesive and cohesionless soils, he suggested that the eccentricity of load be incorporated into the existing bearing capacity theory by assuming the load acts centrally on a foundation of reduced area, such that the centroid of the area coincides with that of the load. This effective area concept acknowledges that under moment loading, tensile stresses develop between the footing base and the soil and partial loss of bearing contact results. For a strip footing this leads to a clearly defined effective contact width ($B' = B(1-2e)$) which defines the effective contact area ($A' = B'L$). In the case of a circular footing, the effective contact area is not clearly defined, however, Meyerhof (1953) suggested the shaded area shown in Figure 5.2a. Unfortunately the procedure to be used in determining the area of the shaded region, and the equivalent rectangle dimension B' and L', is not at all obvious from this diagram.

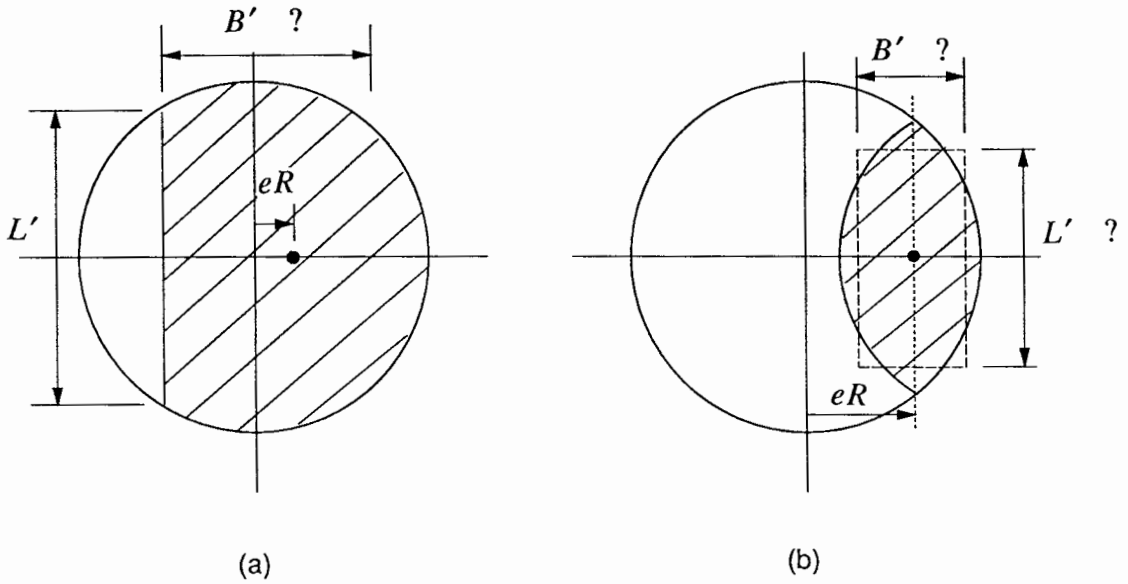

Figure 5.2: Effective contact area due to eccentricity eR, as suggested by: (a) Meyerhof (1953), and (b) Brinch Hansen (1970).

Based on the effective contact area approach, Meyerhof (1953) proposed a combined loading bearing capacity equation, which for a circular footing on an undrained clay reduces to

$$\frac{V}{A'} = (2+\pi)s_u s_c i_c \tag{5.5}$$

where the shape factor s_c = 1.2 and i_c is the inclination factor. In the literature, the inclination factor has been reported in two different forms. One is presented by Lambe and Whitman (1979) as

$$i_c = \left(1 - \frac{2\alpha}{\pi}\right)^2 \tag{5.6}$$

and the other is given by Bowles (1982) as

$$i_c = \left(1 - \frac{2\alpha}{\pi}\right) \tag{5.7}$$

Equations (5.6) and (5.7) are attributed to Meyerhof (1953), however, examination of this paper shows that while he introduced this factor in a graphical form, no formula was fitted to the data. Equation (5.6) appears to be more frequently quoted in the literature.

The Meyerhof (1953) solution (Equation 5.5) is limited in that it does not take into consideration horizontal sliding failure of the foundation. For a given A', it is only applicable for the angle of inclination ranging from α=0°, pure vertical loading, to a value of α where the horizontal component of load (H) reaches its limiting value. This limiting value, expressed in Equation (5.8), is dependent on A' (and therefore the applied moment) and the adhesion between the soil and the footing, commonly taken to be the undrained shear strength of the soil (s_u).

$$H = A' s_u \tag{5.8}$$

5.2.3 Brinch Hansen solution

The Brinch Hansen (1970) bearing capacity solution for combined loading is the most commonly used in the offshore industry. For eccentricity of load, Brinch Hansen (1970) adopts the same effective contact area method as advocated by Meyerhof (1953), but provides a better suggestion for the effective contact area of a circular footing (Figure 5.2b). For a given eccentricity eR, the effective contact area (A') is uniquely geometrically defined as

$$A' = R^2(\pi - 2\arcsin e - 2e\sqrt{1-e^2}) \tag{5.9}$$

For cohesive soils and the problem under consideration, Brinch Hansen (1970) gives the following bearing capacity solution

$$\frac{V}{A'} = (2+\pi)s_u(1+s_c^a - i_c^a) \tag{5.10}$$

where s_c^a and i_c^a are the shape and inclination factors, respectively. These are given for a circular footing as[1]

$$s_c^a = 0.2i_c^a\frac{B'}{L'} = 0.2i_c^a \tag{5.11}$$

$$i_c^a = 0.5\left(1 - \sqrt{1 - \frac{H}{A's_u}}\right) \tag{5.12}$$

As discussed by Houlsby (1984), Equation (5.12) is chosen so that at the point of sliding mode failure, defined by Equation (5.8), i_c^a has a value of 0.5. This corresponds to a reduction in vertical bearing capacity to half of its value for pure vertical loading, and is an exact solution for a strip footing. The Brinch Hansen solution (Equation 5.10) is only applicable for $H \le A's_u$. For greater H, the inclination factor i_c^a is not defined as the term inside the square root of Equation (5.12) is negative. In this case, failure is controlled by horizontal sliding and is independent of vertical load.

The shape factor s_c^a of Equation (5.11) is erroneous as it has a value of zero for pure vertical loading ($i_c^a = 0$). Houlsby (1984) reports that the shape factor has been subsequently changed to

$$s_c^a = 0.2(1 - 2i_c^a) \tag{5.13}$$

This new factor gives the desired value of 0.2 for vertical loading, but reduces to zero as the sliding failure mode is approached. This is considered appropriate as one would assume that sliding failure is solely dependent on the area of contact, and not the shape of the footing.

---

1 The equivalent rectangle dimensions in Equation (5.11) are taken to be the same ($B' = L'$) as these are not uniquely defined for a given effective contact area (Figure 5.2b).

The angle of inclination (α) at which the failure mode changes from bearing (vertical) to sliding (horizontal) can be evaluated by substituting Equations (5.8), (5.12) and (5.13) into Equation (5.10) to give

$$\tan\alpha = \frac{1}{0.5(2+\pi)} \tag{5.14}$$

Solving Equation (5.14) gives $\alpha = 21.26°$.

5.2.4 Vesic solution

Vesic (1975) also adopts the effective area concept of Meyerhof (1953) and Brinch Hansen (1970). For circular foundations, he advocates the effective contact area method adopted by Brinch Hansen, as shown in Figure 5.2b and quantified in Equation (5.9). The resulting bearing capacity equation takes the same form as the Meyerhof solution, Equation (5.5), except in this case the shape factor $s_c = 1 + \frac{1}{2+\pi} = 1.19$ for a circular footing and the inclination factor (i_c) is given as

$$i_c = 1 - \frac{2H}{(2+\pi)A's_u} \tag{5.15}$$

Vesic (1975) also proposes a check against horizontal sliding failure using Equation (5.8). The changeover from vertical to sliding failure mode can be evaluated along the same lines as performed previously for the Brinch Hansen solution. The angle of inclination at this point is given by

$$\tan\alpha = \frac{2+\pi}{\pi(3+\pi)} \tag{5.16}$$

where $\alpha = 14.92°$. This angle is considerably smaller than that which results from the Brinch Hansen solution ($\alpha = 21.26°$), and is a consequence of two things. Firstly, the shape factor is independent of the inclination of the load, where for the Brinch Hansen solution its effect is removed at sliding failure. Secondly, for a strip footing at sliding failure, the inclination factor $i_c = 1 - \frac{2}{2+\pi} = 0.611$, instead of the theoretically correct value of 0.5 adopted by the Brinch Hansen solution. Based on these arguments, it would appear that the Brinch Hansen (1970) inclination

angle, for the transition from bearing to sliding failure, is more appropriate than the Vesic (1975) angle. However, the numerical considerations of Section 5.7 demonstrate that the Vesic solution more accurately predicts the point of transition.

5.3 Mesh Dimensions for Accurate Stability Analysis

Chapter 4 has illustrated the importance of mesh dimensions for accurate finite element analysis of elastic footing behaviour. Examination of the complete load - displacement response would therefore require a mesh dimension of $200R$ to ensure that the initial elastic stiffness of the curve is valid. But this chapter is concerned with stability (failure) analysis, and therefore very little interest is placed in the elastic response. Typical mesh dimensions used previously for the prediction of vertical collapse loads have been of the order five times the width of the footing (Sloan, 1981; Sloan and Randolph, 1982; de Borst and Vermeer, 1984), or in the case of a circular footing, ten times the radius ($10R$). Houlsby and Martin (1990) report that the actual dimensions which encompass the failure envelope of a surface circular footing on undrained clay are considerably smaller than this. Using the Method of Characteristics for a Tresca yield criterion, they show the vertical collapse mechanism to be contained within a radial dimension of $1.85R$ and a depth of $0.85R$. The following investigation demonstrates that mesh dimensions of this order can give acceptably accurate collapse load results. de Borst and Vermeer (1984) have also shown that small mesh dimensions yield accurate collapse loads for frictional soils.

Figure 5.3 presents, for a number of meshes of different dimensions, the load - displacement curves for the vertical loading of a surface rigid rough footing on an elastic perfectly-plastic von Mises material. The analyses use a two-dimensional axisymmetric formulation and 15-node cubic strain triangles[2], this element being shown in Section 3.2 to be suitable for incompressible material analysis. Figure 5.3 also includes the mesh corresponding to the mesh dimensions of $10R \times 10R$, which has 140 *free* degrees-of-freedom, and therefore, as indicated by Table 3.5, should provide accurate results. The smaller mesh dimensions examined, $4R \times 3R$ and $2.33R \times 1.33R$, adopt the same mesh topology as the $10R \times 10R$ mesh, with only a slight variation at the mesh boundaries.

2 Analyses performed using OXFEM

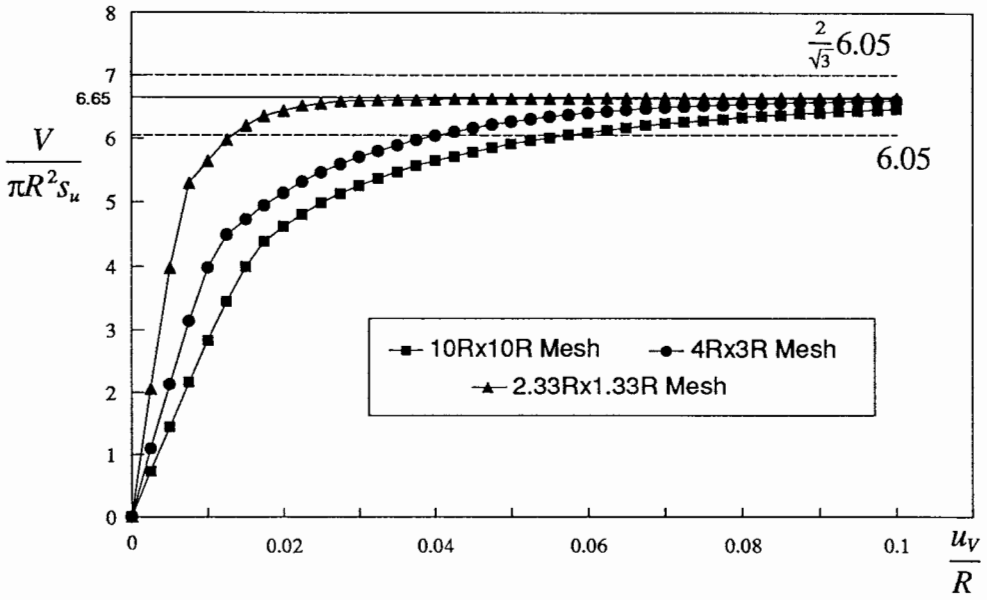

$G/s_u = 100$, $\nu = 0.49$, 15-node cubic strain triangles (13-point integration)

$10R \times 10R$ Mesh: 793 nodes, 92 elements, 1520 unrestrained d.o.f.
$4R \times 3R$ Mesh: 767 nodes, 89 elements, 1468 unrestrained d.o.f.
$2.33R \times 1.33R$ Mesh: 625 nodes, 72 elements, 1180 unrestrained d.o.f.

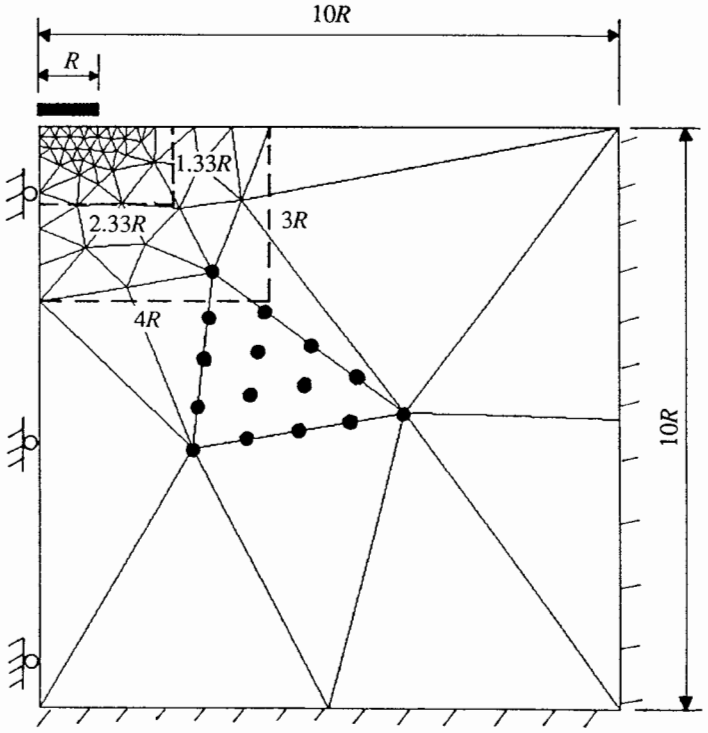

$10R \times 10R$ Mesh

Figure 5.3: Load - displacement response of a vertically loaded rigid rough circular footing for a range of mesh dimensions, using a two-dimensional axisymmetric formulation.

The results of Figure 5.3 demonstrate the vertical collapse load of a rough rigid circular footing to be about $6.65\pi R^2 s_u$. This value is consistent with the upper and lower limits for a von Mises material, which are included in Figure 5.3. As discussed in Section 3.2, these limits are based on the collapse load for a Tresca yield criterion. Figure 5.3 shows that the collapse load can be successfully predicted using the mesh dimensions of $2.33R \times 1.33R$. These dimensions are more desirable than the larger mesh dimensions considered since they are more computationally efficient. The smaller mesh dimensions remove most of the elastic component of the response and concentrates the plasticity to the zone where the failure mechanism forms. Hence, fewer load steps are required in the non-linear analysis to achieve the collapse load. Furthermore, the number of nodes and unrestrained degrees-of-freedom in the $2.33R \times 1.33R$ mesh is significantly less than the larger meshes and therefore leads to a considerable improvement in computational efficiency. Even though the above investigation is limited to the vertical loading case, the mesh dimensions of $2.33R \times 1.33R$ are thought to be equally applicable to combined loading conditions. This is because the failure mechanisms for horizontal and moment loading are much more localised than the vertical loading case (Vesic, 1975).

All three-dimensional stability analyses reported in this chapter use the 20-node quadratic strain tetrahedron mesh PSR20, which has a radial mesh dimension of $2.33R$ and a mesh depth of $1.33R$. Mesh PSR20 is presented in Figure 3.10, and was demonstrated in sub-section 3.2.5 to predict the vertical bearing capacity of a surface footing to within 3% (Figure 3.8).

5.4 Two Dimensional Interface Elements

5.4.1 Background

It is becoming well recognised that conventional continuum finite elements in many cases do not adequately model the soil-structure interaction problem where large relative lateral movement can occur (Griffiths, 1985; Gens *et al*, 1989; Handel *et al*, 1990). This is applicable to the problem under consideration, since the contribution of lateral loading to footing stability is an important factor to be examined. Furthermore, Section 5.2 has highlighted the need for the finite element model to simulate the loss of footing contact with the soil which results when moment loading is applied to the footing. This is also something which cannot be simply modelled using continuum elements. These requirements of the finite element model can only be attained by adopting a special class of finite element called interface elements.

The applications of interface elements have usually involved the modelling of soil-structure interface behaviour, such as: jointed rock masses, footings, piles and soil reinforcement (Goodman *et al*, 1968; Griffiths, 1985; Zaman, 1985; Gens *et al*, 1989; Handel *et al*, 1990; Burd and Brocklehurst, 1991). As detailed by Gens *et al* (1989), four main categories of finite elements have been proposed for the modelling of interfaces. These are as follows:

1. standard finite elements of small thickness (Griffiths, 1985),
2. quasi-continuum elements possessing a weakness plane in the direction of the interface (Zienkiewicz *et al*, 1970),
3. linkage elements in which only the connections between opposite nodes are considered (Frank *et al*, 1982), and
4. interface elements in which the relative displacements between opposite nodes are the primary deformation variables. This category can have finite (Handel *et al*, 1990) or zero thicknesses (Goodman *et al*, 1968; Gens *et al*, 1989; Burd and Brocklehurst, 1991).

Analysing a number of plasticity problems, Griffiths (1985) showed the small thickness 8-node quadrilateral element to give satisfactory results for aspect ratios of up to 100. However, he concluded that recourse to interface elements may prove necessary where slippage (large relative movement) is a major factor. For problems with a clearly defined soil-structure interface, the zero thickness interface element of category 4 has been used with much success. This type of element has therefore been incorporated into the finite element model presented in Chapter 2, and its theory for two-dimensional interface elements is given below.

5.4.2 20-node triangular interface element

The 20-node triangular interface element is incorporated into the finite element model as it is kinematically compatible with the 20-node tetrahedron adopted in this research. The 20-node triangle (Figure 5.4a) has 10 nodes per face, and its displacement (shape) functions are complete to order 3. The element geometry consists of 10 pairs of nodes sharing the same three-dimensional coordinate position, however, within each pair the nodes have independent degrees-of-freedom. The node numbering in Figure 5.4a, where the top nodes are numbered first and the bottom nodes last, is chosen for ease of notation in the following sub-section. It is also convenient that top node 4 has a corresponding bottom node numbered 14.

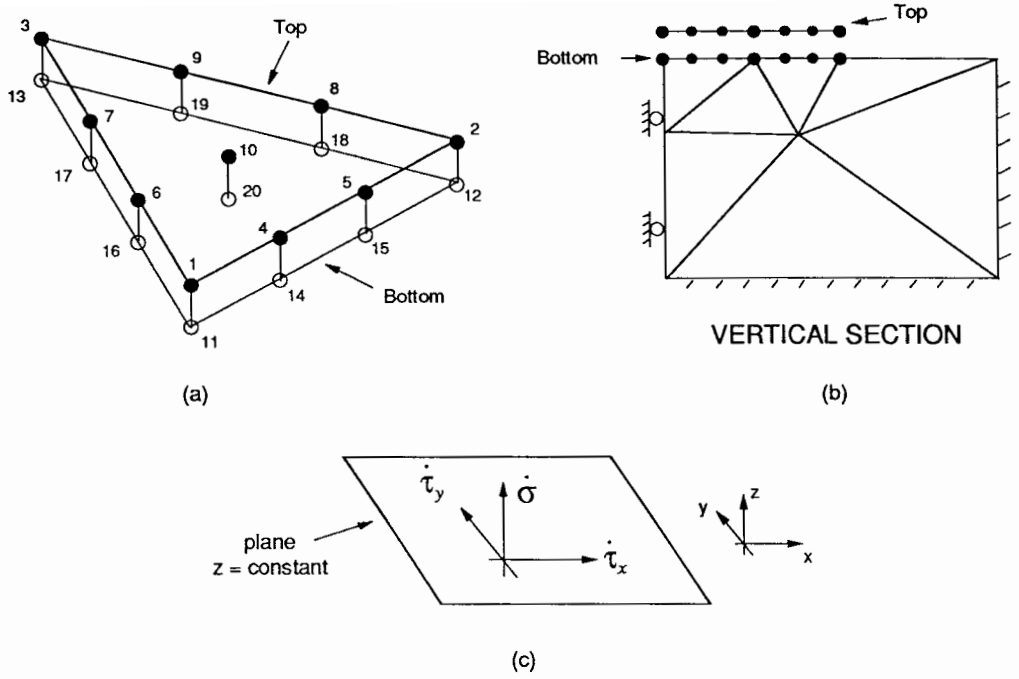

Figure 5.4: (a) 20-node triangular interface element, (b) Application to the modelling of a surface footing - soil interface, (c) Stress orientation and sign convention

The two-dimensional representation of Figure 5.4b illustrates how the 20-node triangle is incorporated into a continuum mesh of 20-node tetrahedra to model the footing-soil interface. The bottom nodes of the interface elements are connected to the corresponding continuum nodes at the top of the mesh. The top interface nodes are left free. As for Chapter 4, all analyses in this chapter are displacement controlled, where the imposed displacements are applied to the top interface nodes.

5.4.3 Finite element equations

For this class of interface element, the constitutive equations, defining the interface element material stiffness matrix ($[\mathbf{D}_i]^{ep}$), are written in terms of the relative velocities ($\mathbf{u}_r$) within the element as follows

$$\dot{\boldsymbol{\sigma}} = [\mathbf{D}_i]^{ep}\mathbf{u}_r \tag{5.17}$$

where the vectors $\dot{\boldsymbol{\sigma}}$ and $\mathbf{u}_r$ have three components

$$\dot{\boldsymbol{\sigma}} = \begin{pmatrix} \dot{\tau}_x \\ \dot{\tau}_y \\ \dot{\sigma} \end{pmatrix} \qquad \text{and} \qquad \mathbf{u}_r = \begin{pmatrix} u_r \\ v_r \\ w_r \end{pmatrix} \tag{5.18}$$

The two shear stress-rate components ($\dot{\tau}_x, \dot{\tau}_y$) and one normal stress-rate component ($\dot{\sigma}$) are illustrated in Figure 5.4c for the sign convention adopted. The relative velocities are related to the nodal velocities **U** by the equation

$$\mathbf{u}_r = \mathbf{u}_T - \mathbf{u}_B = [\mathbf{N}_i](\mathbf{U}_T - \mathbf{U}_B) \tag{5.19}$$

where the notation T and B denote the top and bottom interface nodes, and the matrix $[\mathbf{N}_i]$ contains the shape functions of the two-dimensional 10-node quadratic strain triangle. These shape functions are not presented here as they are given in the finite element texts by Zienkiewicz (1977) and Kardestuncer and Norrie (1987). Equation (5.19) can be rewritten

$$\mathbf{u}_r = [\mathbf{B}_i]\mathbf{U} \tag{5.20}$$

where

$$[\mathbf{B}_i] = [\mathbf{N}_i \mid -\mathbf{N}_i] \qquad \text{and} \qquad \mathbf{U} = \begin{pmatrix} \mathbf{U}_T \\ \mathbf{U}_B \end{pmatrix} \tag{5.21}$$

Substituting Equations (5.17) and (5.20) into an equivalent interface element form of the continuum virtual work relationship of Equation (2.1) gives the interface element tangent stiffness matrix ($[\mathbf{K}_i]$) to be

$$\mathbf{P} = [\mathbf{K}_i]\mathbf{U} \quad \text{where} \quad [\mathbf{K}_i] = \int_A [\mathbf{B}_i]^T [\mathbf{D}_i]^{ep} [\mathbf{B}_i] \det[\mathbf{J}_i] d\alpha \, d\beta \tag{5.22}$$

As for the three-dimensional continuum relationship (Equation 2.7), the stiffness matrix $[\mathbf{K}_i]$ is evaluated using isoparametric mapping. However, in this case, $[\mathbf{J}_i]$ is the Jacobian of the two-dimensional transformation from global (x, y) to local coordinates (α, β). In this formulation the interface element is assumed to be flat and lie on the plane z = constant, as this is all that is required by the geometry of the problem. A curved interface element, at a given orientation, can be formulated by mapping from three-dimensional global coordinates (x, y, z) to two-dimensional local coordinates (α, β). The mathematics involved in uniquely defining the Jacobian matrix, however, is complex. This special type of transformation has been performed by Burd and Brocklehurst (1991) for the plane strain analysis of soil reinforcement. In their formulation, for a 6-noded one-dimensional interface element, they map from (x, y) to (α).

5.4.4 Elasto-plasticity

The adopted interface element elasto-plasticity (constitutive) model is essentially the same as that used for the continuum elements (Section 2.3). As the element is assumed to have zero thickness, the normal stress (σ) behaves in a purely elastic fashion. The two shear stress components (τ_x, τ_y) adopt a linearly-elastic perfectly-plastic von Mises constitutive behaviour. The von Mises yield function of Equation (2.6) therefore reduces to

$$f(\boldsymbol{\sigma}) = 3\tau_x^2 + 3\tau_y^2 - 4c^2 \tag{5.23}$$

which is simply a circle in the (τ_x, τ_y) plane. In the analyses presented in this chapter, the shear (or adhesive) strength of the footing-soil interface (c in Equation 5.23) is set equal to the undrained shear strength of the continuum (s_u).

As for the continuum formulation, the interface element material stiffness matrix ($[\mathbf{D}_i]^{ep}$), defined in Equation (5.17), is divisible into elastic and plastic components as follows

$$[\mathbf{D}_i]^{ep} = [\mathbf{D}_i]^{e} + [\mathbf{D}_i]^{p} \tag{5.24}$$

The elastic material stiffness matrix ($[\mathbf{D}_i]^{e}$) takes the form originally suggested by Goodman *et al* (1968)

$$[\mathbf{D}_i]^{e} = \begin{bmatrix} K_s & 0 & 0 \\ 0 & K_s & 0 \\ 0 & 0 & K_n \end{bmatrix} \tag{5.25}$$

where K_s and K_n are the interface stiffnesses tangent and normal to the element. The ratio of continuum shear stiffness (G) to tangent interface stiffness (K_s) has dimensions of length and represents the equivalent continuum thickness of the interface element when subjected to pure shear. For a rough footing base, the problem at hand, G/K_s should ideally be set to a very small dimension to represent a footing base that has no relative movement to the soil until the adhesive strength of the interface, taken to be s_u, is exceeded. Unfortunately, small values of G/K_s were observed to cause numerical instability when non-linear behaviour is modelled. This issue is addressed later in this section. To represent a zero thickness element in the direction normal to

the interface, the normal interface stiffness K_n should be given a value such that the ratio G/K_n is also a very small value. As for G/K_s, this ratio has dimensions of length, but does not simply equate to an equivalent continuum thickness of the interface element. There is uncertainty as to whether the normal deformation characteristics of the interface element is best represented by Young's modulus or the constrained modulus of the continuum. In either case, the value of $G/K_n = 10^{-6}R$, adopted in the analyses presented in this chapter, is thought to represent a very thin element such that the compressibility of the interface element is insignificant.

Adopting an associated flow rule ($f(\boldsymbol{\sigma}) = g(\boldsymbol{\sigma})$), the plastic material interface stiffness matrix ($[D_i]^p$) is derived from Equation (2.9), the general form of this matrix for a continuum, as

$$[\mathbf{D}_i]^p = -\frac{3K_s}{4s_u^2}\begin{bmatrix} \tau_x^2 & \tau_x\tau_y & 0 \\ \tau_y\tau_x & \tau_y^2 & 0 \\ 0 & 0 & 0 \end{bmatrix} \tag{5.26}$$

The interface Gauss point stress updating procedure is in essence the same as that detailed in sub-section 2.3.3 for the continuum. For conciseness of presentation the relevant interface equations will not be repeated here. Instead it will be noted that the equations of sub-section 2.3.3 can be modified to the interface problem by substituting in:

- the relative velocities u_r, v_r, w_r for the corresponding continuum strain rates $\dot{\gamma}_{zx}, \dot{\gamma}_{yz}, \dot{\varepsilon}_{zz}$,
- the interface stresses τ_x, τ_y, σ for the corresponding continuum stresses $\tau_{zx}, \tau_{yz}, \sigma_{zz}$,
- the interface stiffnesses K_s and K_n for the continuum G as appropriate, and

noting that the interface normal stress σ is always elastic.

5.4.5 Numerical integration

Gens *et al* (1989) investigated the application of one and two dimensional interface elements to model a pull-out test, where a reinforcement element is extracted from a surrounding material. This problem is similar to a laterally loaded footing since it is basically controlled by the sliding mode of deformation. For one-dimensional elements, it was observed that spurious oscillations of the shear stress resulted when a Gaussian integration scheme was used. However, they were removed when a Newton-Cotes scheme, where all of the integration points lie at the element nodes, was adopted. An eigenvalue analysis of the problem indicated that better performances

are obtained when the interface element stiffness matrix is diagonally dominant, as occurs with a Newton-Cotes scheme since the nodal degrees-of-freedom are uncoupled. Burd and Brocklehurst (1991), however, observed interface element stresses to be stable for a Gaussian integration scheme where sliding failure is not the dominant mode of deformation.

For three-dimensional problems, Gens *et al* (1989) suggest that the performance of two-dimensional interface elements are relatively unaffected by the integration scheme used. This was observed to be the case in this study where initial analyses using the 20-node triangular interface element included both Gaussian and Newton-Cotes integration. A 7-point Gauss scheme (Zienkiewicz, 1977), accurate to order 5, was adopted since the advocated 4-point scheme, for triangular elements with shape functions to order 3 (Zienkiewicz, 1977; Kardestuncer and Norrie, 1987), involves a large negative weighting at the centre of the element[3]. The 10-point Newton-Cotes scheme was formulated by Houlsby (1990) and is included as Appendix A.2, as it is not given in finite element texts. Comparisons under combined loading conditions showed the stability and load-displacement performance of the two schemes to be virtually the same. Spurious oscillations of the interface stresses were not observed for the Gaussian scheme, however, a slightly smoother distribution of stress, desirable for the modelling of footing loss of contact, was noted for the Newton-Cotes scheme. Therefore Newton-Cotes was used in all analyses presented in this chapter.

5.4.6 Numerical instability

Initial applications of interface elements to the finite element model showed numerical instability occurred under combined loading plasticity conditions. Numerical instabilities have also been noted by Burd (1990) in the application of one-dimensional interface elements to soil reinforcement problems. For the case of rigid horizontal displacement, Figure 5.5 provides examples of the types of numerical instabilities observed. Note that the these analyses are preceded by a pure vertical displacement of the rigid circular footing until all vertical load capacity is exhausted. The vertical load - vertical displacement curves for the three runs examined in Figure 5.5 (Runs IH1 to IH3) are almost identical. The curve for Run IH3 is given in Figure 5.6 and labelled Run IV3.

---

3 The problems associated with using a negative weighting is discussed in greater detail in Section 4.3 for the 20-node tetrahedron.

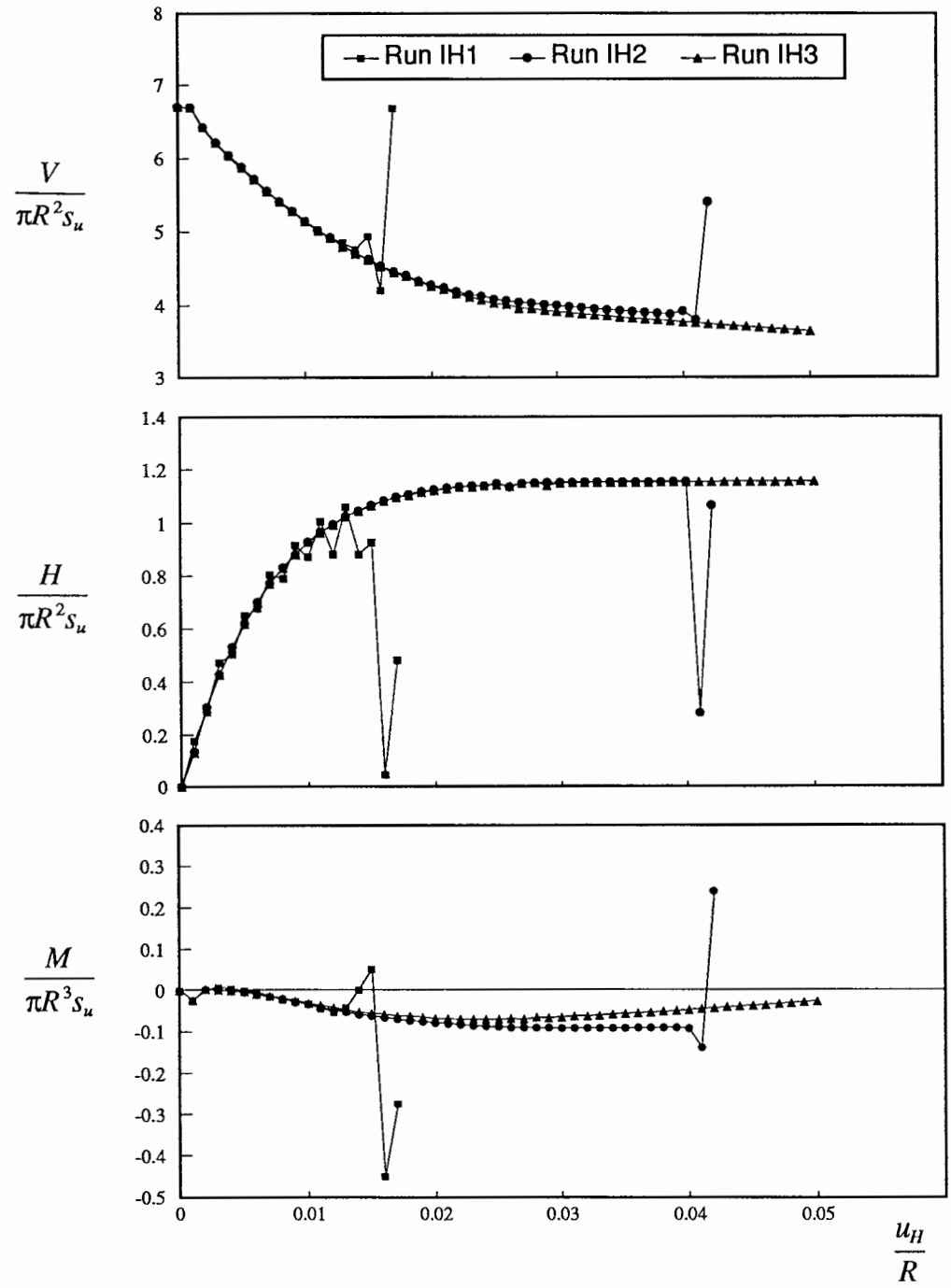

Continuum: $G/s_u = 100$, $\nu = 0.49$

Interface: $G/K_n = 10^{-6}R$

All analyses are preceded by vertical displacement to failure (Figure 5.6), are displacement controlled, and use Mesh PSR20 (Figure 3.10)

Run IH1: $G/K_s = 0.01R$, $C = 1.0$

Run IH2: $G/K_s = 0.025R$, $C = 1.0$

Run IH3: $G/K_s = 0.025R$, $C = 0.99$

Figure 5.5: Examples of interface element numerical instability for rigid horizontal displacement combined loading conditions.

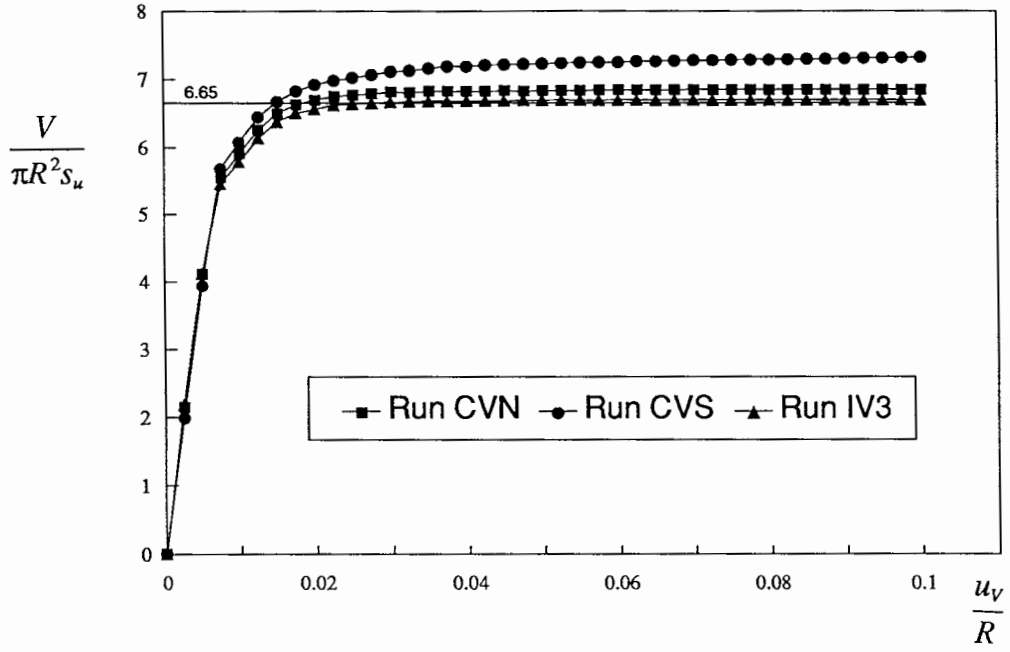

Continuum: $G/s_u = 100$, $\nu = 0.49$

All analyses are displacement controlled (40 steps) and use Mesh PSR20 (Figure 3.10)

Run CVN: Continuum elements - V computed as summation of nodal forces
Run CVS: Continuum elements - V computed from integration of surface Gauss point stresses
Run IV3: Interface elements - $G/K_n = 10^{-6}R$, $G/K_s = 0.025R$, $C = 0.99$

Figure 5.6: Prediction of the vertical collapse load using continuum and interface elements to model the footing-soil interface.

Figure 5.5 demonstrates that there are two main causes of the numerical instabilities observed. The first cause is that interface elements are sensitive to the interface tangent stiffness (K_s) values used in the analysis. As discussed in sub-section 5.4.4, to model ideally a rough footing base, the equivalent interface element thickness, represented by the ratio G/K_s, should be given a very small dimension. However, if a moderate value of $G/K_s = 0.01R$ (interface element thickness of 1% of R) is adopted, as in Run IH1 in Figure 5.5, numerical instabilities occur well before the limit horizontal load is reached. This particular case of instability can be overcome by adopting a more modest value of $G/K_s = 0.025R$ (thickness of 2.5% of R), as shown in Runs IH2 and IH3 in Figure 5.5. Similar instability problems, and sensitivity to K_s, were also observed for the combined loading analyses of rigid footing rotation. It was also observed in separate interface element runs that the numerical instability of Run IH1 can be somewhat alleviated by

using a smaller step size in the non-linear analysis and smaller element dimensions. The sensitivities of the instability to these factors, however, were found to be significantly less than K_s.

It is important to note in Run IH1 that instability develops in the horizontal load before it is observed in the vertical and moment loads (Figure 5.5). Close examination of the shear stresses of the footing interface elements and the underlying continuum Gauss points showed the two distributions of stress to be significantly different prior to the instability developing. This suggests that the sensitivity of the problem to K_s may be a result of incompatibility between the interface and continuum plasticity models. It seems unlikely that the instability is a consequence of ill-conditioning of the global stiffness matrix due to the ratio of G/K_s, since a ratio of two orders of magnitude ($G/K_s = 0.01R$) should not cause round-off error problems when using double precision arithmetic.

The main concern with adopting an interface tangent stiffness value corresponding to $G/K_s = 0.025R$ is whether it models accurately the footing-soil interface for a perfectly rough footing. The results of Figure 5.6 suggest that this may not be the case. For pure vertical loading and footing loads calculated using the common summation of nodal forces technique, the mesh of solely 20-node tetrahedron continua elements (Run CVN) predicts a vertical collapse load 3% greater than the best available estimate of the exact collapse load, $6.65\pi R^2 s_u$ (Section 5.3), and 2% greater than what the combined interface-continuum mesh predicts (Run IV3). This difference could be a consequence of the latter's equivalent interface thickness (G/K_s) being too large, and therefore allowing significant lateral movement to occur before the interface has yielded. Alternatively, it may be a consequence of the conflicting shear stress distributions of the interface and the continuum elements at the footing-soil interface, as noted in the previous paragraph. Considering the relative insensitivity of the predicted vertical collapse load to the value of K_s (for values of $G/K_s = 0.01R$ and $0.025R$), it is thought that the explanation based on conflicting stresses is the most likely. Nevertheless, a 2% difference in the predicted vertical collapse load is not considered significant, and an interface thickness of $G/K_s = 0.025R$ is thought to model adequately the footing-soil interface for a perfectly rough footing.

The second cause of numerical instability is demonstrated in Run IH2 of Figure 5.5, where instability was not observed until the horizontal load had reached its limit value for a von Mises material ($2/\sqrt{3}\,\pi R^2 s_u$). Under lateral shearing conditions for a surface footing, the diagonal terms in the stiffness matrix corresponding to the "top" interface element nodes tend to zero as "full" plasticity is developed. This problem can be overcome by redefining the interface element material stiffness matrix ($[D_i]^{ep}$), previously given in Equation (5.24), to be

$$[D_i]^{ep} = [D_i]^{e} + C.[D_i]^{p} \tag{5.27}$$

where the parameter C can vary from 0, for a purely elastic matrix, to 1, for the standard elastic perfectly-plastic matrix (Equation 5.24). A value of $C = 0.99$, as adopted in Run IH3, allows a nominal 1% stiffness of the top interface nodes to be retained under full plasticity conditions. This prevents the global stiffness matrix from becoming ill-conditioned and results in the stable solution given in Figure 5.5. The only shortcoming of this approach is that a 1% error is automatically induced into the convergence parameter computation (discussed in Section 2.2), and can result in a significant increase in computational effort per run.

5.5 Rigidly Connected Footing

The first stage in the application of finite elements to offshore foundations is to examine the problem of a surface footing connected rigidly to the soil (continuum) so that loss of footing contact cannot develop. This simpler problem can be modelled by both continuum and interface elements located at the footing-soil interface. To evaluate the performance of these two alternative approaches, the combined loading cases of rigid horizontal displacement and rigid rotation, presented in Figures 5.7 and 5.8 respectively, are considered. These runs are both preceded by rigid vertical displacement of the footing until the vertical collapse (failure) load is clearly reached (Figure 5.6). The results of Figures 5.7 and 5.8 are presented as the non-dimensional loads of $H^* = H/(\pi R^2 s_u)$ and $M^* = M/(\pi R^3 s_u)$ plotted against $V^* = V/(\pi R^2 s_u)$. In these figures the horizontal (H^*) and moment (M^*) loads are seen to develop while the vertical (V^*) load reduces with the imposed displacement.

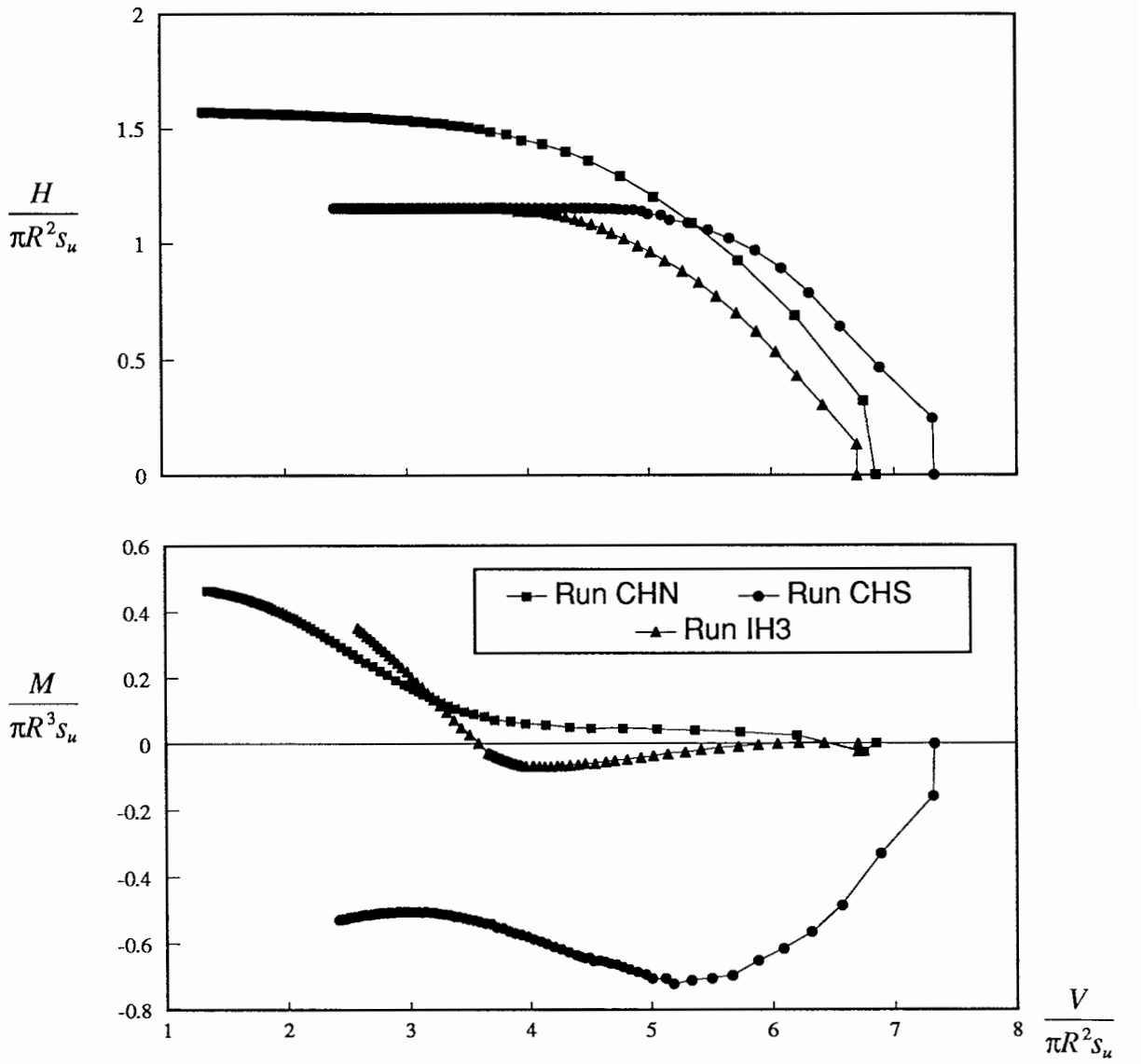

Continuum: $G/s_u = 100$, $\nu = 0.49$

All analyses are displacement controlled, and use Mesh PSR20 (Figure 3.10)

Run CHN: Continuum elements - V, H, M values computed as summation of footing nodal forces. Analysis follows from Run CVN (Figure 5.6)
$u_H/R = 0.0 \rightarrow 0.05$ (25 steps) and $0.05 \rightarrow 0.25$ (50 steps)

Run CHS: Continuum elements - V, H, M values computed from integration of footing Gauss point stresses. Analysis follows from Run CVS (Figure 5.6)
$u_H/R = 0.0 \rightarrow 0.05$ (25 steps) and $0.05 \rightarrow 0.25$ (50 steps)

Run IH3: Interface elements - $G/K_n = 10^{-6}R$, $G/K_s = 0.025R$, $C = 0.99$. Analysis follows from Run IV3 (Figure 5.6)
$u_H/R = 0.0 \rightarrow 0.05$ (50 steps) and $0.05 \rightarrow 0.15$ (25 steps)

Figure 5.7: The failure envelope for rigid horizontal displacement of a rigidly connected footing using continuum and interface elements to model the footing-soil interface.

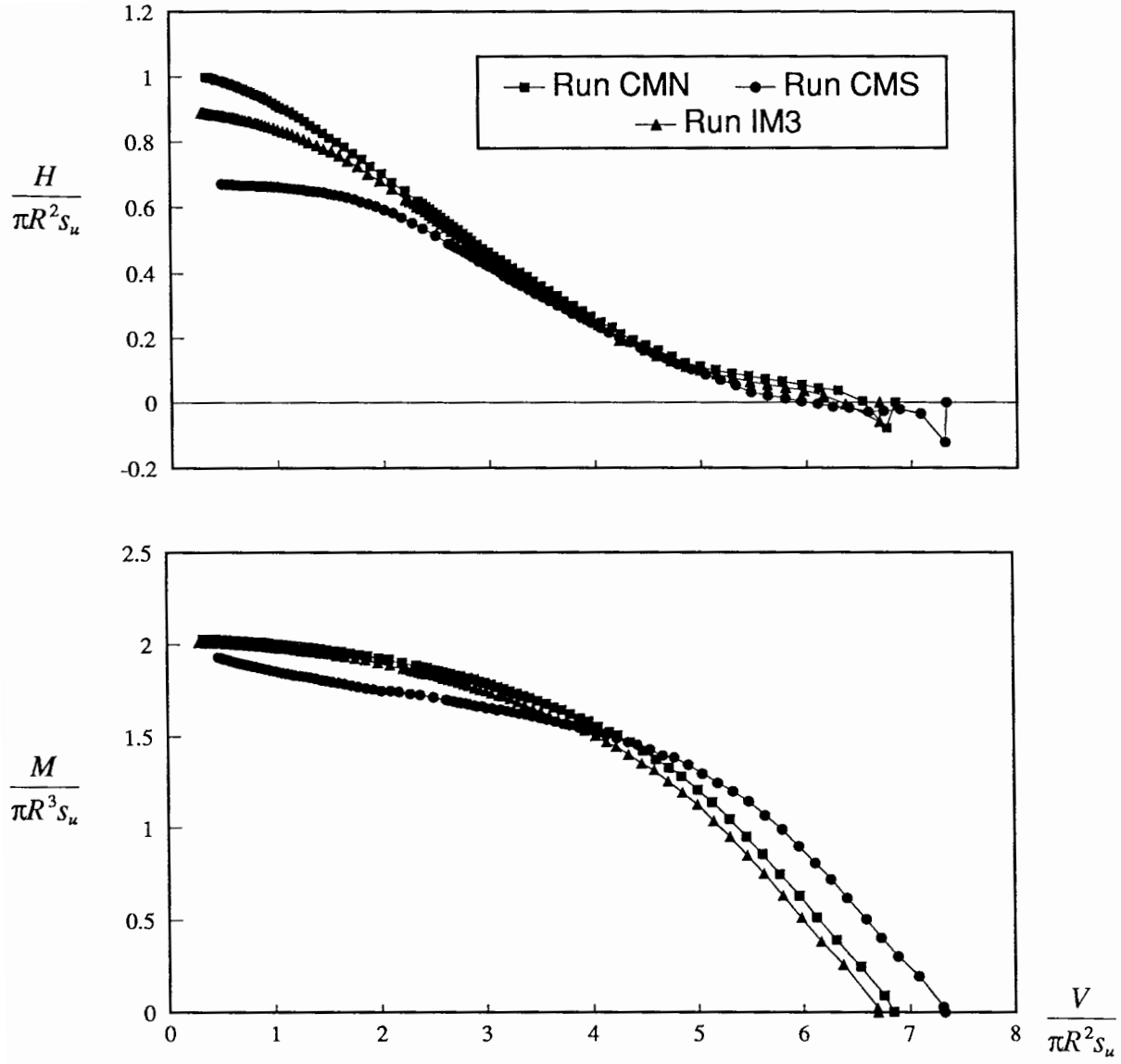

Continuum: $G/s_u = 100$, $\nu = 0.49$

All analyses are displacement controlled, and use Mesh PSR20 (Figure 3.10)

Run CMN: Continuum elements - V, H, M values computed as summation of footing nodal forces. Analysis follows from Run CVN (Figure 5.6)
$\theta_M = 0.0 \rightarrow 0.05$ (50 steps) and $0.05 \rightarrow 0.25$ (50 steps)

Run CMS: Continuum elements - V, H, M values computed from integration of footing Gauss point stresses. Analysis follows from Run CVS (Figure 5.6)
$\theta_M = 0.0 \rightarrow 0.05$ (50 steps) and $0.05 \rightarrow 0.25$ (50 steps)

Run IM3: Interface elements - $G/K_n = 10^{-6}R$, $G/K_s = 0.025R$, $C = 0.99$. Analysis follows from Run IV3 (Figure 5.6)
$\theta_M = 0.0 \rightarrow 0.05$ (50 steps) and $0.05 \rightarrow 0.25$ (50 steps)

Figure 5.8: The failure envelope for rigid rotation of a rigidly connected footing using continuum and interface elements to model the footing-soil interface.

As the footing is initially loaded vertically to failure, and therefore the incremental response is perfectly plastic (no elasticity), the curves of Figures 5.7 and 5.8 define paths across the failure envelope in three-dimensional (V,H,M) space. This assumption was confirmed to be the correct in analyses, not presented here, where the footing was initially loaded vertically to a value less than that corresponding to failure. Subsequent rotation and horizontal displacement modes showed the footing to load elastically to the failure envelope defined by the runs where the vertical failure load was reached (eg Figures 5.7 and 5.8). During this elastic loading the vertical load (V) remained reasonably constant. Further imposed displacement demonstrated the footing response to follow the failure envelope.

Figures 5.7 and 5.8 examine three possible ways of modelling the footing-soil interface for a rigidly connected footing. Continuum elements are used in the first case, Runs CHN and CMN, where the commonly used technique of computing the V,H,M values as the summation of footing nodal forces is adopted. A different interpretation of the continuum element analysis is to calculate the footing loads by integrating the Gauss point stresses at the footing interface (Runs CHS and CMS). For the numerical integration scheme used, the Gauss points are located at the corners and centroid of each face (Appendix A.1). The integration of the stresses involved a numerical scheme with weightings of 1/12 at the corners and 3/4 at the centroid. The final method considered is to use interface elements, as introduced in the previous section. Run IH3 $(G/K_n = 10^{-6}R, G/K_s = 0.025R$ and $C = 0.99)$, which was demonstrated to be numerically stable in Figure 5.5 for rigid horizontal displacement, is repeated in Figure 5.7. The response for rigid footing rotation, Run IM3 in Figure 5.8, used the same values of K_n, K_s and C as Run IH3.

The inadequacy of continuum elements to model interfaces, where large lateral relative movement can occur, is illustrated in Figure 5.7. Run CHN demonstrates that computing H as the summation of footing nodal forces leads to a 35% overprediction of the horizontal sliding load for a von Mises material $(2/\sqrt{3}\pi R^2 s_u)$. A similar observation for continuum elements has been made by Griffiths (1985) who examined a laterally loaded circular footing using the harmonic loading technique (discussed briefly in Section 1.4). His analysis showed the limit load to be exceeded by 20%. Examination of the Gauss point stresses at the footing base for Run CHN revealed that the shear stresses corresponding to the direction of imposed displacement were all at the limit value for pure shear in a von Mises material $(2/\sqrt{3}s_u)$. Calculating H using the footing Gauss point stresses therefore gives the correct limit load (Run CHS in Figure 5.7). However, this approach is deficient in that it gives a high vertical bearing capacity, and what is

thought to be a rather spurious moment. The inclusion of interface elements in Figure 5.7, to model the footing-soil interface, is seen to alleviate many of the problems experienced by the continuum elements. For Run IH3, the moment stays small (maximum eccentricity of $0.025R$) up to the point where the true horizontal limit load is reached.

Figure 5.8 demonstrates that the modelling of a footing-soil interface using continuum and interface elements is more comparable when the shearing mode of deformation is not dominant. Apart from differing vertical bearing capacities, the three sets of curves are in close agreement for most of the imposed rigid footing rotation. It is interesting to note that a large horizontal load develops under conditions of large rigid footing rotation. An important aspect of the analyses in Figure 5.8 is the vertical normal stresses which develop in the interface elements under large moment. This provides an indication as to the suitability of interface elements to model loss of footing contact when tensile stresses develop between the footing base and the soil. Figure 5.9 presents contour plots of the vertical interface stresses for three points on the track of the failure envelope defined by Run IM3 in Figure 5.8.

The first footing stress distribution considered in Figure 5.9 is at the point of full vertical bearing capacity $(V^*, H^*, M^*) = (6.7, 0, 0)$. As would be expected, this plot shows the symmetry of the vertical stress about the y axis, and that the stress for most of the footing is between $6s_u$ and $7s_u$. However, the very high stresses at the edge of the footing are not consistent with plasticity theory, which results in the fact that the vertical normal stress at the edge of the footing cannot exceed the vertical bearing capacity. This phenomenon was also observed for the continuum elements and is therefore not thought to be a consequence of using interface elements. A spurious stress concentration at the edge of a pile tip has been observed by van Langen and Vermeer (1990) who examined the problem of pile penetration in clay and modelled the soil-structure interaction using interface elements. The high edge stress was attributed to a lack of mesh flexibility in this area. Implementation of special internal interface elements at the edge of the tip, orientated in directions of potential slip planes, alleviated the problem. It is thought that the finding of van Langen and Vermeer (1990) is the most likely explanation for the stress concentrations observed in Figure 5.9. However, the implementation of two-dimensional internal interface elements was considered beyond the scope of this research.

1. (V^*, H^*, M^*)
$= (6.7, 0.0, 0.0)$

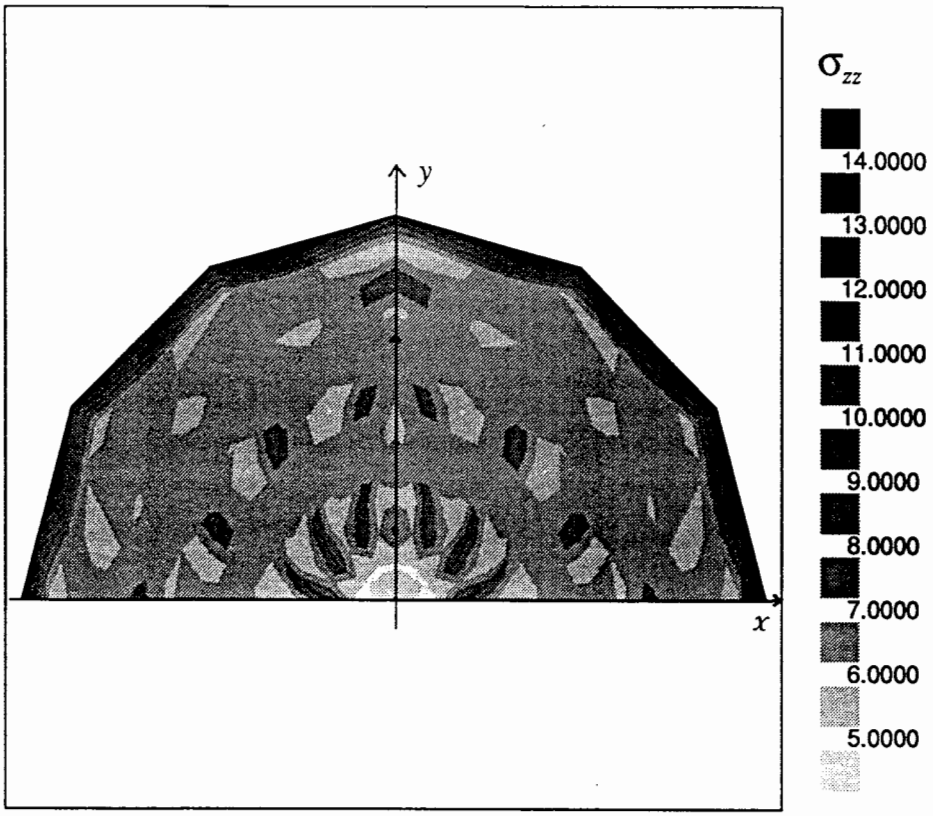

2. (V^*, H^*, M^*)
$= (5.0, 0.10, 1.13)$

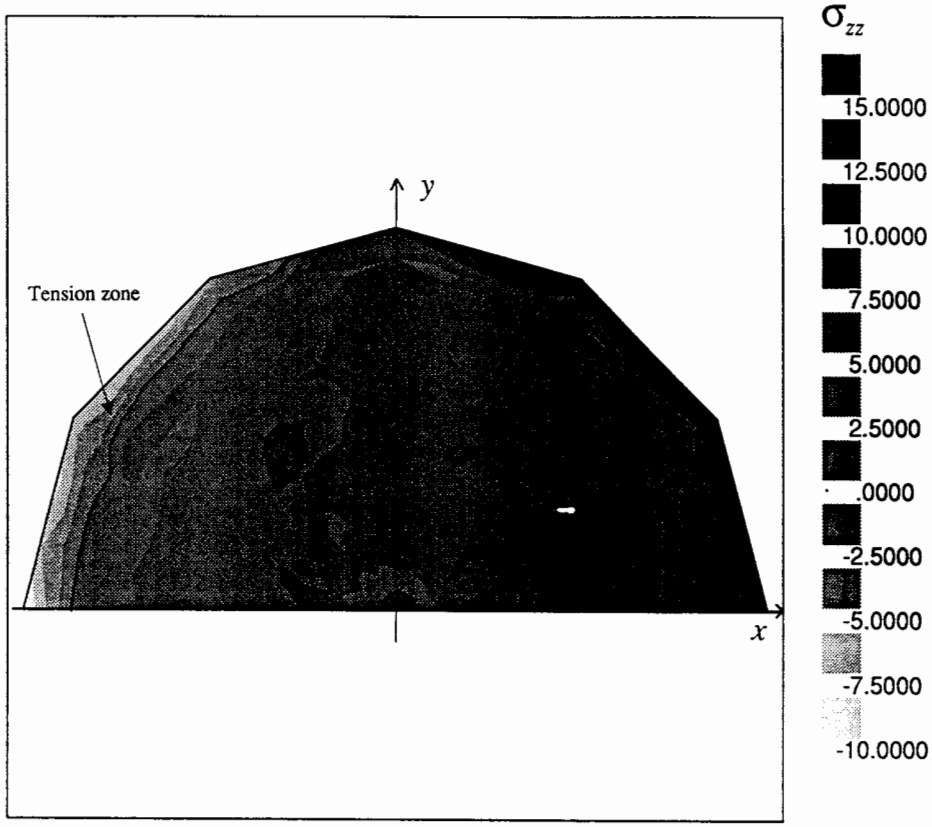

(Figure 5.9 continued next page)

(Figure 5.9 continued)

3. (V^*, H^*, M^*)
$= (3.5, 0.36, 1.65)$

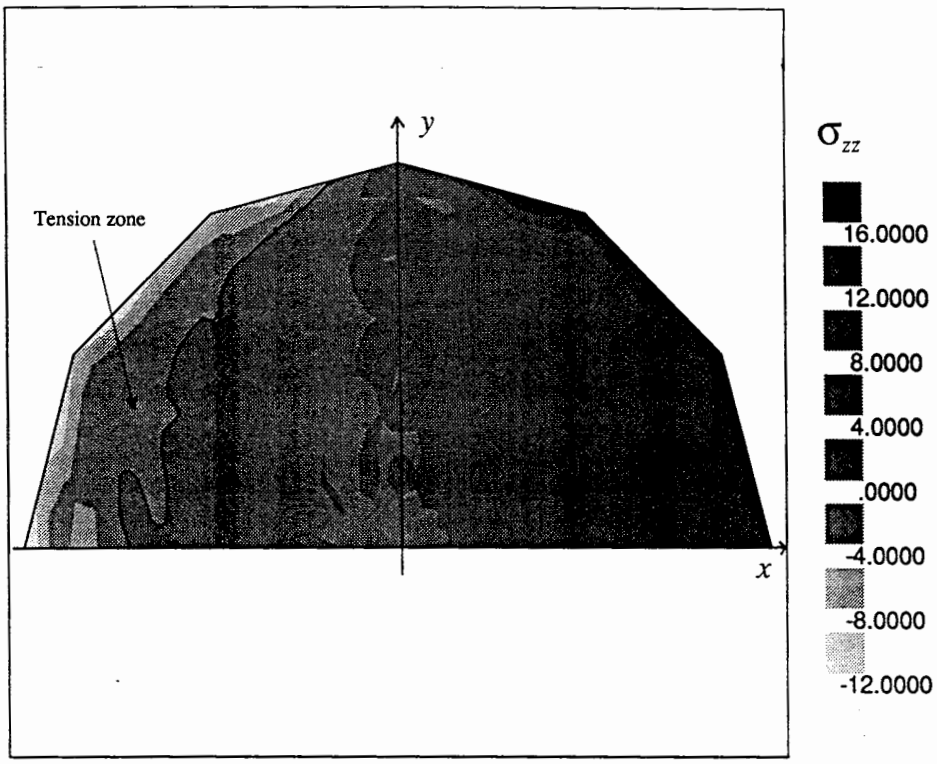

Figure 5.9: Contours of the vertical normal interface stress at three points on the failure envelope for rigid rotation of a rigidly connected footing (Run IM3 in Figure 5.8).

The other interface vertical stress distributions examined in Figure 5.9 correspond to the points $(V^*, H^*, M^*) = (5.0, 0.10, 1.13)$ and $(V^*, H^*, M^*) = (3.5, 0.36, 1.65)$. Both contour plots of stress display a clearly defined zone where tensile stresses have developed on the side of the footing opposite to the direction of the imposed rotation. The shape of the tension zone is reasonably consistent with that postulated by Brinch Hansen (1970) for loss of footing contact due to moment loading (Figure 5.2b). The results are furthermore consistent in that the area of the tension zone is directly related to the magnitude of the moment, as can be seen by comparing points 2 and 3 in Figure 5.9. This good correlation with theory, and what would be conceptually expected, suggests that interface elements will be able to model loss of footing contact. This extension of the finite element model is addressed in the next section. Note that the edge stress concentration, discussed previously, is still prevalent for rigid footing rotation (Figure 5.9) and will undoubtedly introduce a positive error to the computed moment (M). This is because the high edge stresses are generally at a greater lever arm than the acceptable smaller stresses closer to the centroid of the footing base.

5.6 Loss of Footing Contact

Loss of footing contact is incorporated into the interface element theory, presented in Section 5.4, by introducing a new state parameter to the Gauss point stress updating routine. When the Gauss point normal stress becomes tensile (negative), STATE is set to 2, and the normal and shear stresses are given a value of zero to represent the stress free surface that has developed. The normal and tangent interface stiffnesses (K_n and K_s) for the Gauss point are given a small residual value, that is, the ratios of G/K_n and G/K_s are given very large dimensions. This represents a very thick interface where the top and bottom interface element nodes are effectively independent. This addition to the constitutive model is simplistic in that it is assumed that the footing contact with the soil is never re-established.

This new loss of contact model was applied to the rigid footing rotation displacement mode, and is presented as Run IM5 in Figure 5.10. The residual interface stiffnesses, corresponding to STATE = 2, were given values of $G/K_n^{res} = 300R$ and $G/K_s^{res} = 100R$. The convergence parameter CONV (Section 2.2) was observed in Run IM5 to increase with each imposed displacement, resulting in complete numerical instability of the solution by $\theta_M = 0.033$. Varying K_n^{res} and K_s^{res} by an order of magnitude indicated that the computed response and numerical stability were relatively insensitive to these parameters. A thorough examination of the causes of the increasing convergence parameter and numerical instability is beyond the scope of this thesis, however, some insight into these problems is gained by inspecting the contour plots of the interface vertical stresses presented in Figure 5.11. This figure presents the footing stress distributions for three points, defined by Run IM5, representing progressively increasing loss of contact. The results show that significant loss of contact does not propagate smoothly from the edge of the circular footing, as would be expected for a rigid footing. Instead, internal zones lose contact while some external zones still remain in contact, this facet being clearly highlighted in the stress contours for point 3 (Figure 5.11). Random loss of contact may well be one reason for instabilities in the solution, however, the cause of this randomness is not immediately apparent.

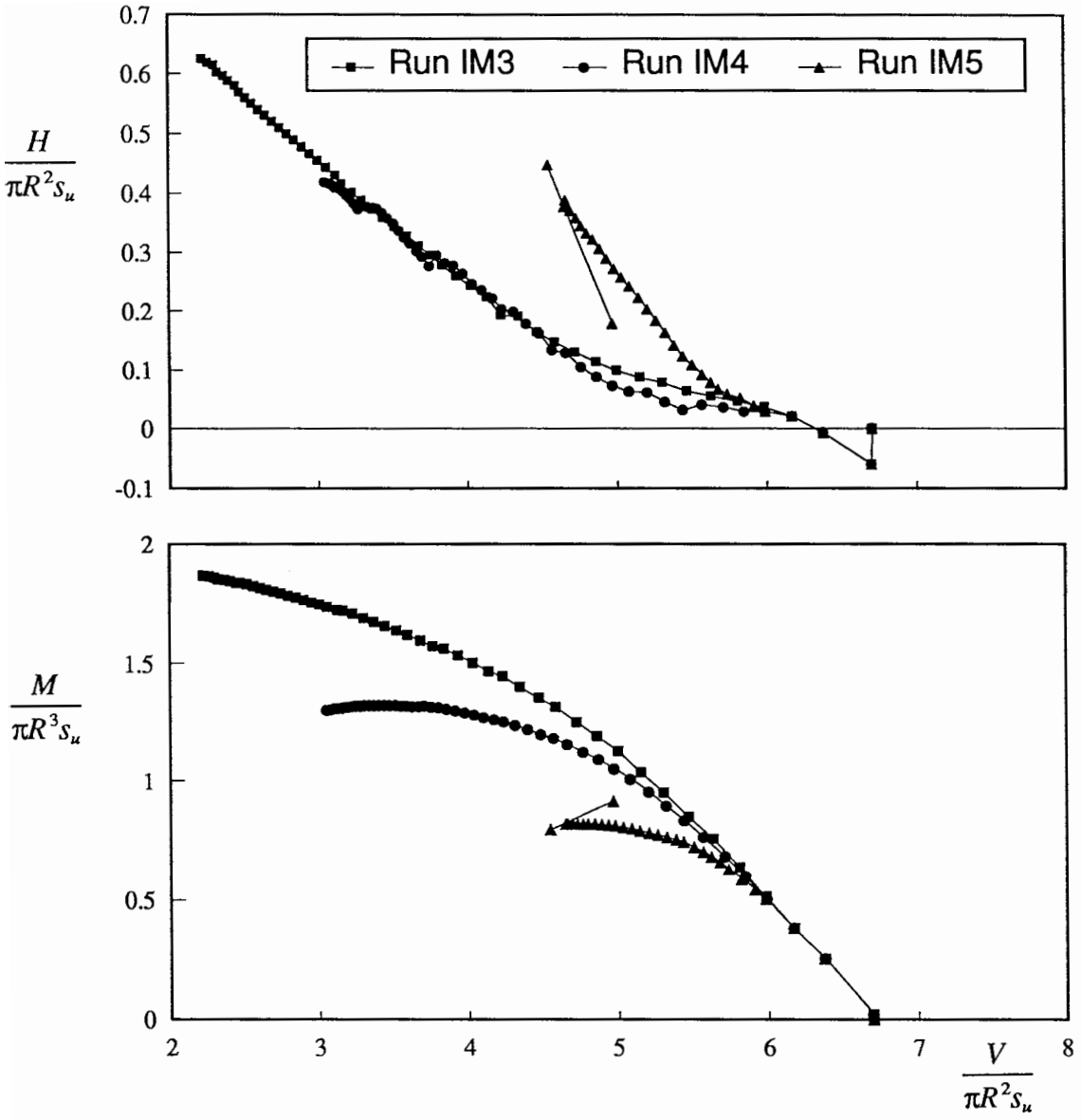

Continuum: $G/s_u = 100$, $\nu = 0.49$

Interface: $G/K_n = 10^{-6}R$, $G/K_s = 0.025R$, $C = 0.99$

All analyses are displacement controlled, follow from Run IV3 (Figure 5.6), model the footing-soil interface using interface elements, and use Mesh PSR20 (Figure 3.10)

Run IM3: Rigidly connected footing - V, H, M computed from all footing nodes
$\theta_M = 0.0 \rightarrow 0.05$, 50 steps

Run IM4: Rigidly connected footing - V, H, M computed from all footing nodes where V is compressive (positive)
$\theta_M = 0.0 \rightarrow 0.05$, 50 steps

Run IM5: Loss of footing contact - $G/K_n^{res} = 300R$, $G/K_s^{res} = 100R$
$\theta_M = 0.0 \rightarrow 0.033$, 33 steps

Figure 5.10: Different applications of interface elements to modelling loss of footing contact with the soil, for the displacement mode of rigid footing rotation.

1. (V^*, H^*, M^*)
$= (5.9, 0.04, 0.54)$

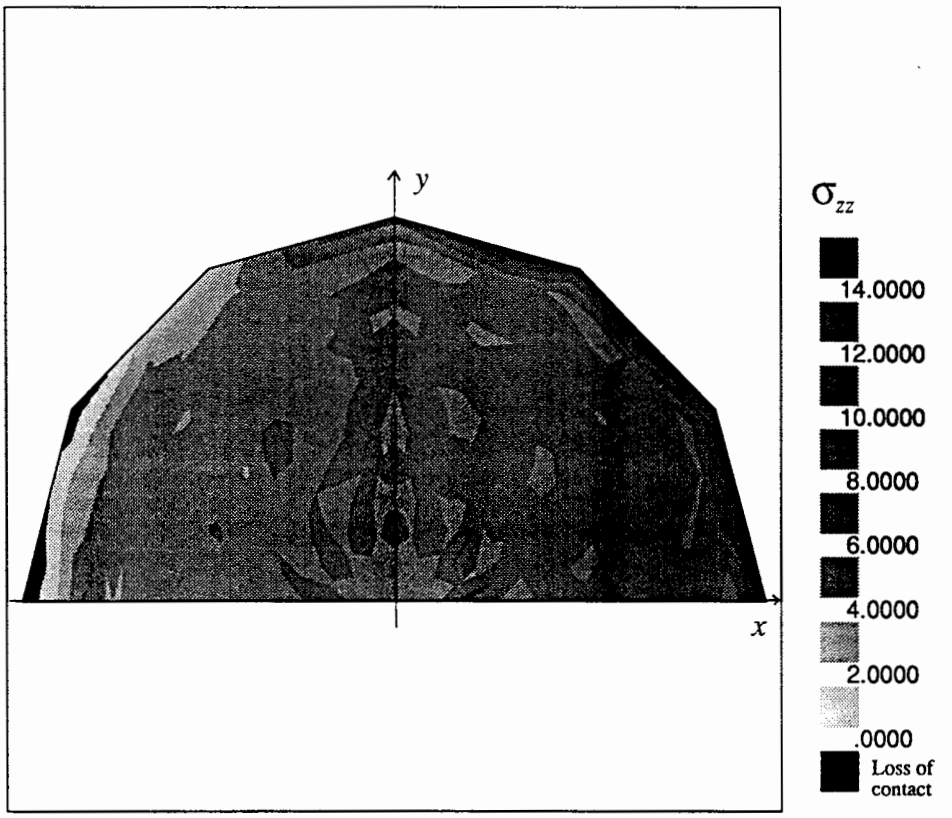

2. (V^*, H^*, M^*)
$= (5.3, 0.18, 0.77)$

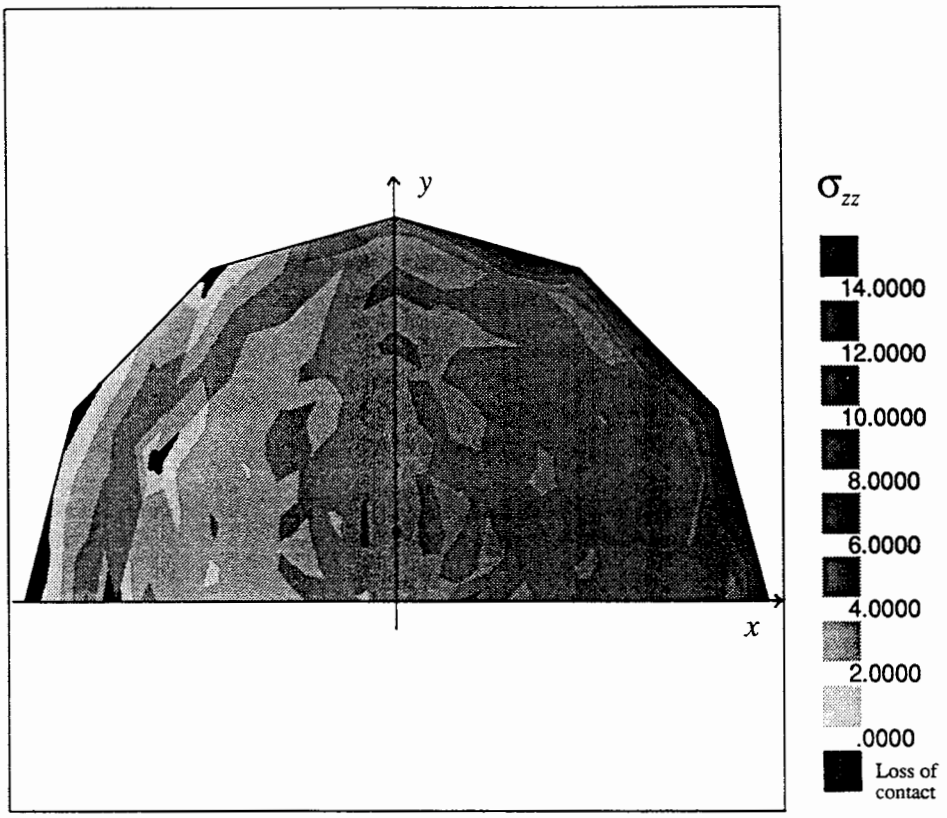

(Figure 5.11 continued next page)

(Figure 5.11 continued)

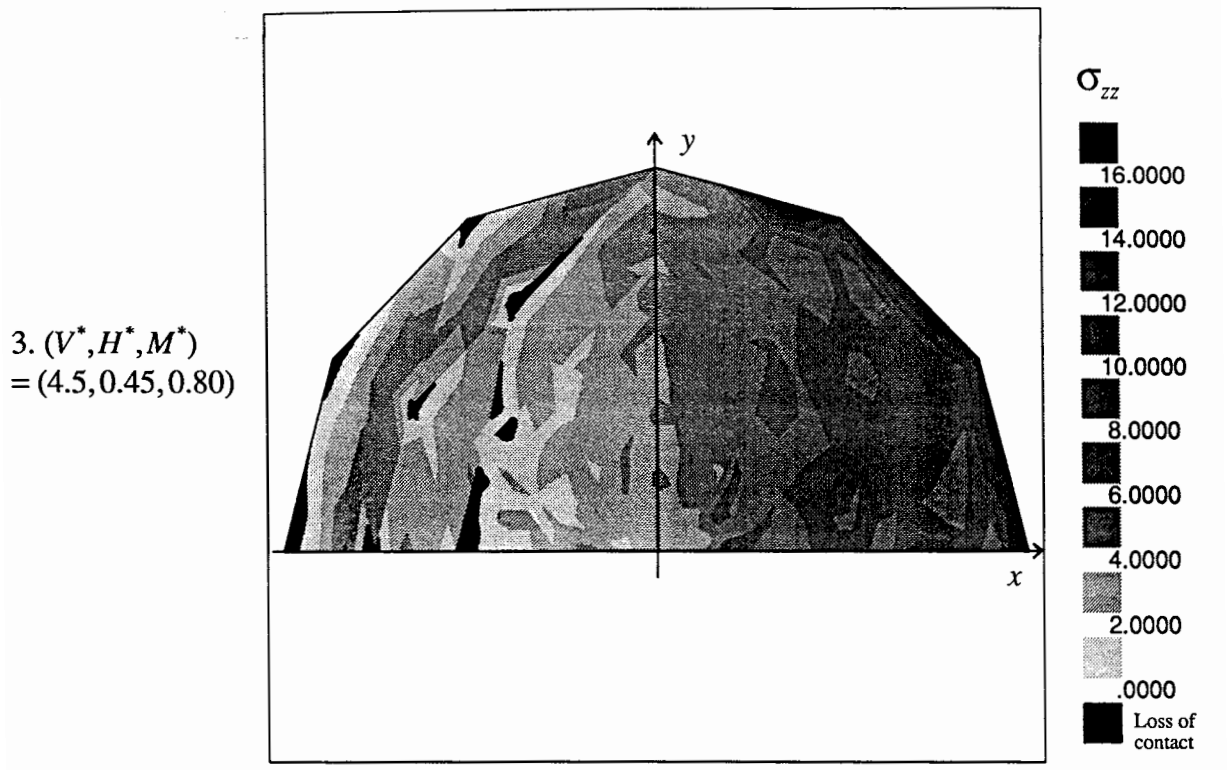

Figure 5.11: The vertical normal stress distributions of the interface elements at three points on the failure envelope for rigid rotation of a footing that can lose contact with the soil (Run IM5 in Figure 5.10).

The increasing convergence parameter and resulting instability of Run IM5 places doubt on the validity of this solution and the loss of contact model. This run also suffered from excessively long computing time as the large convergence parameter required the stiffness equations to be formulated and solved each displacement step. For the purposes of this research, an alternative more simplistic approach to modelling loss of footing contact was sought. As presented in Figure 5.10, one approach considered is to approximate the response by the rigidly connected footing solution (Run IM3) examined in the previous section. However, a better approximation is thought to be obtained by using the rigidly connected footing analysis and calculating the footing loads only from the footing nodes where the vertical load (V) is compressive. The failure envelope of this solution, designated Run IM4 in Figure 5.10, lies between the rigidly connected and loss of contact footing solutions, for rigid footing rotation. Based on the stability and smoothness of the tensile stress zone for this solution (Figure 5.9), it is thought to be a reasonable approximation to the true response, and is therefore adopted in the following analyses of Figure 5.12.

The analyses presented so far in this chapter have only considered 3 imposed displacement modes: vertical displacement to full vertical bearing capacity, rigid horizontal displacement, and rigid rotation. The latter modes define tracks across the failure envelope in (V,H,M) space. The complete failure envelope for the footing can be built up by examining other (V,H,M) tracks corresponding to displacement modes which are a combination of horizontal displacement and rotation. This approach is demonstrated in Figure 5.12, where a first attempt towards defining the shape of the failure surface at high vertical loads is presented.

As illustrated in Figure 5.12a, six displacement modes, covering a range of combinations of horizontal displacement (u_H) and rotation (θ_M), were analysed. These incorporate the first two quadrants of the (u_H, θ_M) displacement space. Because of the symmetry of the problem, the V,H,M results for the other two quadrants are obtained by simply reflecting the computed values about the V axis. The non-dimensional vertical load V^*, for all four quadrants, is contoured against H^* and M^* in Figure 5.12b, and effectively represents a plan view of the top half of the failure surface. The quality of the solution is thought to be high when there is no loss of contact, however, as discussed earlier, the solution only serves as a best approximation for large moment and loss of footing contact. The zones which correspond to significant loss of footing contact, as highlighted in Figure 5.12b, were evaluated by determining the point where the solution deviates from the footing loads computed using all of the footing nodes. The results of Figure 5.10 demonstrate this to be a sound approach. Run IM4, which uses the same solution technique as adopted in Figure 5.12b, indicates a loss of contact, by deviating from Run IM3 (rigidly connected footing), at the same point as suggested by the loss of contact solution (Run IM5).

The contoured plan view of the failure envelope (Figure 5.12b) shows a series of (approximate) ellipses which seem to rotate clockwise as V reduces and H and M increase in absolute value. At the same time the eccentricity of the ellipses decreases. For large H and M the contours become more square than elliptical, however, this may not correctly reflect the true failure surface as these contours do encompass the loss of contact zone. Furthermore, the contouring is coarser for these contours as the H,M values are more widely spaced.

The failure envelope given in Figure 5.12b is a first attempt towards determining a more comprehensive and "complete" (all values of vertical load) failure surface. Apart from a possible refinement of the displacement modes analysed in Figure 5.12, other combinations of displacement modes need to be examined, for example, rigid horizontal displacement followed

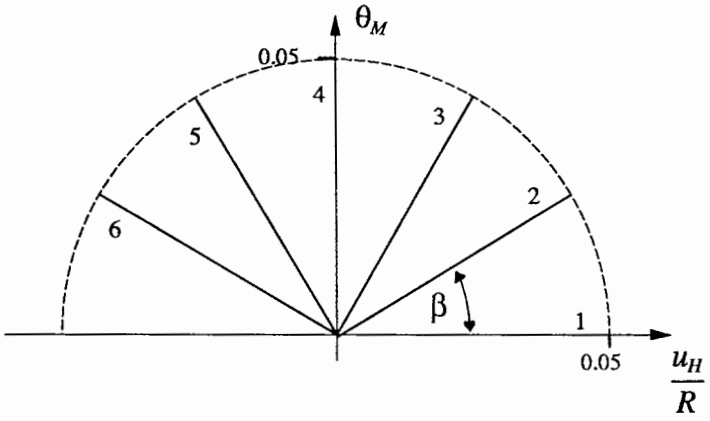

Run	β
1 (IH3)	0°
2	30°
3	60°
4 (IM4)	90°
5	120°
6	150°

(a)

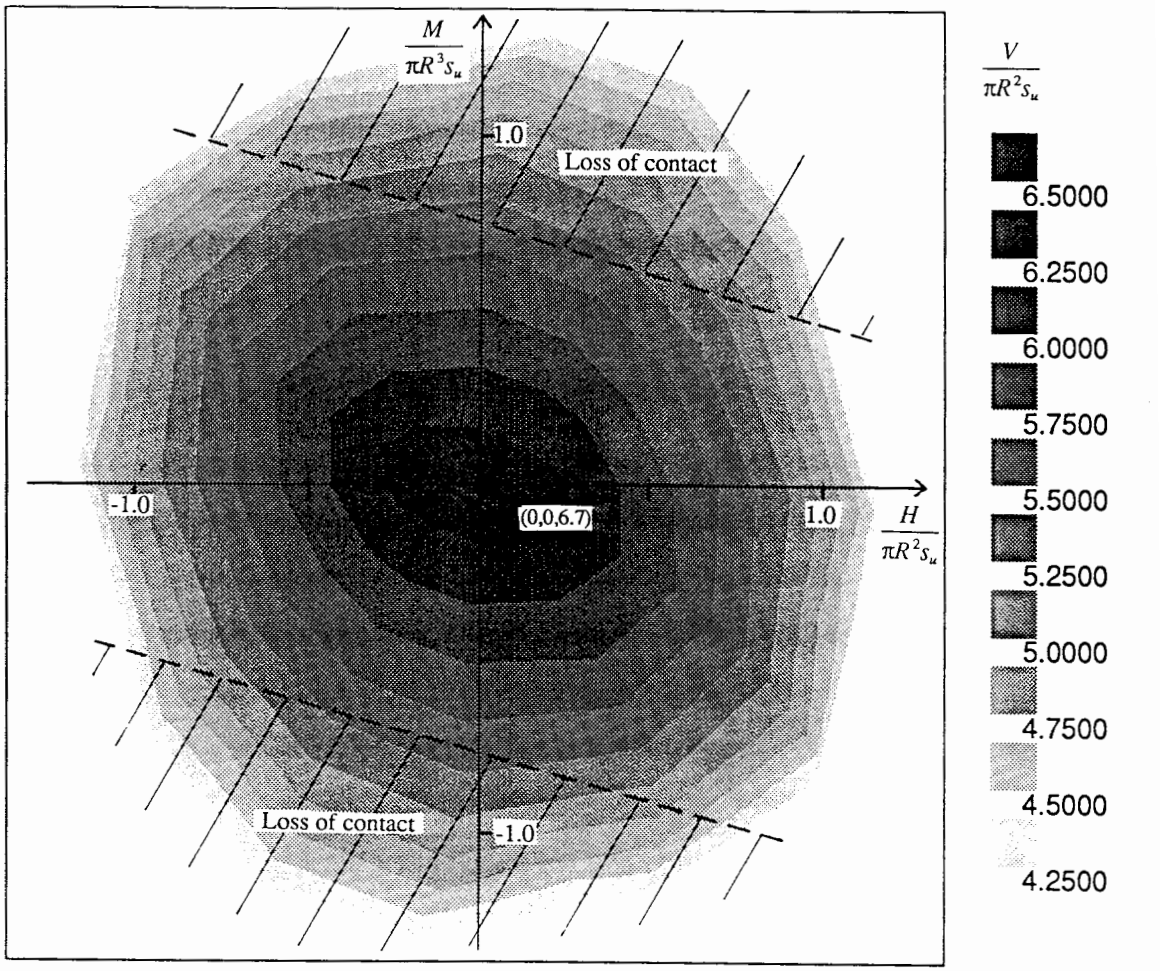

(b)

Figure 5.12: Determination of the failure envelope of a rigid rough circular footing at the surface of an undrained clay (a) Displacement modes analysed (b) Contour plan view of the failure envelope at high vertical load.

by rigid rotation. Comparing these runs with those examined in this study can confirm that a given point on the failure envelope is independent of the direction from which it is approached. The bottom half of the failure envelope (small values of vertical load) can be derived by initially loading the footing vertically to a very small value, say $V/(\pi R^2 s_u) = 0.5$. The footing is then elastically loaded to the failure envelope by imposing combinations of u_H and θ_M. It is expected that the resulting track on the failure surface will generally show V to increase with the imposed displacement in a manner opposite to that observed in this study.

5.7 Comparison with Bearing Capacity Solutions

An important component of this overall study is to compare the computed failure envelopes with the combined loading bearing capacity equations reviewed in Section 5.2. A comprehensive comparison is not thought appropriate as insufficient confidence exists in the failure envelope presented in Figure 5.12b for loss of footing contact. Therefore, the effective area concept, which represents moment loading in the bearing capacity solutions, cannot be fully investigated. Nevertheless, a good level of confidence exists in the computed failure surface where horizontal loading is predominant (no loss of contact), and therefore the inclination factors of Section 5.2 (which model horizontal loading) are examined.

Figure 5.13 presents a comparison of the numerical and analytical solutions in (V^*, H^*) space. Since the moment (M) is taken to be zero (no eccentricity of load), the examination of the bearing capacity solutions is simplified in that they adopt the full footing area ($A' = \pi R^2$). The finite element solution corresponds to the continuum-interface analysis of Run IH3, previously presented in Figure 5.7. This is considered appropriate as the moment in this run was small. Obtaining the V^*, H^* values from the contours of Figure 5.12b would have essentially provided the same result. The inclined loading bearing capacity solutions examined in Figure 5.13 are given in Equations (5.28)-(5.30) in their non-dimensional form. They have been normalised with respect to the numerically computed vertical bearing capacity ($V^* = 6.7$), and slightly modified to account for the fact that the non-dimensional horizontal limit load for a von Mises material is $H^* = 2/\sqrt{3}$.

Meyerhof (1953):

$$V^* = 6.7\left\{1 - \frac{2}{\pi}\tan^{-1}\left(\frac{H^*}{V^*}\right)\right\}^2 \qquad (5.28)$$

Brinch Hansen (1970):

$$V^* = 5.88\left\{1.2 - 0.7\left(1 - \sqrt{1 - \frac{H^*}{2\sqrt{3}}}\right)\right\} \tag{5.29}$$

Vesic (1975):

$$V^* = 6.7(1 - 0.34H^*) \tag{5.30}$$

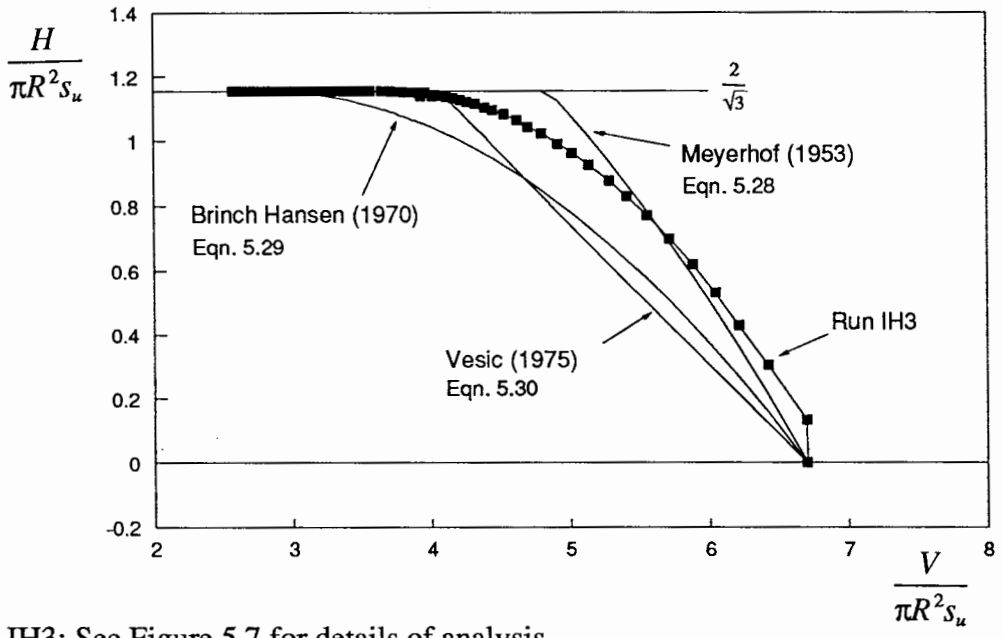

Run IH3: See Figure 5.7 for details of analysis

Figure 5.13: Comparison of finite element and bearing capacity solutions in (V^*, H^*) space (M = 0).

The finite element solution shows that Brinch Hansen (1970) best approximates the general shape of the failure envelope under inclined loading conditions, but is considerably conservative. This bearing capacity equation also does not correctly pick up the point of transition from pure vertical loading to sliding failure. The Vesic (1975) solution is also over-conservative, but does accurately predict the point of transition from bearing to sliding failure, even though the straight line is a poor fit to the numerical data. The initial part of the failure envelope is best approximated by the Meyerhof (1953) solution. Unfortunately this solution becomes unsafe for large H^*. It is recognised that errors will be associated with the finite element solution. However, noting that the vertical and horizontal limit loads are well approximated, the errors are thought to be no greater than 5% at any point on the numerical curve, and therefore the above comparisons valid.

CHAPTER 6 CONCLUSIONS

6.1 Concluding Remarks

Shallow offshore foundations which achieve their stability through the action of the foundation base bearing on the seabed, such as: gravity platforms, the spudcans of jack-up oil rigs, and mudmats of piled structures, can in most applications be idealised as large rigid circular footings. These foundations may often be embedded slightly below the soil surface and are required to withstand significant horizontal and moment loading.

The objective of this study was to examine the elastic behaviour and stability of shallow offshore foundations under combined vertical, horizontal and moment loading, using both existing analytical solutions and finite element modelling techniques. A small strain linear-elastic perfectly-plastic three-dimensional finite element program (OXFEM2) was developed to analyse the problem of a circular footing subjected to combined loading. For non-linear analysis, the governing finite element equations are solved using the modified Euler scheme with selective stiffness formulation. This scheme limits the number of times the stiffness matrix is formulated and solved, while still maintaining the desired level of accuracy. It therefore has a particular advantage in three-dimensional analyses since the solution of the stiffness equations is in many applications the most computationally intensive component.

The research in this thesis is divided into three main areas, as addressed separately in the following sub-sections.

6.1.1 Suitability of three dimensional finite elements for modelling material incompressibility

The choice of a suitable finite element for accurate and computationally efficient analysis is dependent on the element's ability to model incompressible soil conditions, when using the displacement finite element method and exact numerical integration. Chapter 3 has introduced a new quantitative approach for evaluating the suitability of finite elements to analyse incompressible materials. The previously used method is considered not to provide a rigorous quantitative measure of element suitability, nor to allow comparisons between elements of different order and type, where computational effort is a consideration. Hence three new

parameters, quantified in terms of *free* degrees-of-freedom (equal to the degrees-of-freedom minus the incompressibility constraints) have been introduced and applied to two and three dimensional finite elements. The basis of this approach is that the number of free degrees-of-freedom are directly related to the accuracy of the analysis. This conjecture is supported by a number of three-dimensional finite element experiments and comparisons with a similar two-dimensional study.

The tetrahedron family is the most suitable and computationally efficient group of three-dimensional elements for incompressible material analysis. The Serendipity cube family is unsuitable. Similarly the first two elements of the Lagrangian cube family, the 8-node and 27-node cubes, are unsuitable, while all higher order elements are suitable, but computationally inefficient. The examination of the tetrahedron family was divided into two categories since a cube can be divided into either 5 or 6 tetrahedra. The constant strain tetrahedron is unsuitable for both categories. The linear strain tetrahedron is suitable when used in a 5 tetrahedra per cube arrangement, and is on the borderline of suitability in a 6 tetrahedra per cube arrangement, since the number of free degrees-of-freedom per element is zero. The latter is thought to be only suitable if the mesh boundary nodes are not over-constrained, although the analysis would be very inefficient because of the poor ratio of *free* to *total* degrees-of-freedom. All subsequent higher order tetrahedra produce free degrees-of-freedom and are therefore suitable. For the finite element model adopted in this thesis, the quadratic strain and cubic strain tetrahedra are thought to be the most computationally efficient. The 20-node quadratic strain tetrahedron, configured in a 6 tetrahedron per cube arrangement, was adopted for all analyses presented in this thesis.

6.1.2 Elastic behaviour

The elastic behaviour of offshore foundations has important applications to many aspects of offshore design. For a rigid circular footing, most of the available elastic solutions refer to footings placed at the surface level. Exact solutions exist for the two possible loading cases of a smooth surface footing, that is, vertical and moment loading. For a rough footing, the vertical loading case has an exact solution, while the only other available solutions approximate horizontal loading. These approximate solutions fail to recognise the cross coupling between the horizontal load and moment responses for a rough surface footing.

Finite element analyses of a rigid circular footing placed on an elastic continuum demonstrated that the proximity of the mesh boundaries can affect the accuracy of the elastic stiffness prediction. A mesh dimension of 200 footing radii (R) was therefore adopted for all elastic analyses reported, and is thought to limit the error to about +0.5%. For a surface footing, the exact analytical solutions are well reproduced by the numerical solutions. The numerical solutions also show that the cross coupling between the horizontal load and moment components is in most cases not very significant for a rough surface footing, and is non-existent for an incompressible soil. Numerical comparisons with two approximate horizontal loading analytical solutions demonstrated that one solution provides a good estimate of the true response, while the other gives a poorer estimate for compressible soils.

The effect of footing embedment on the elastic response was investigated to embedment depths of $4R$, for combined loading conditions, and the full range of Poisson's ratio. Three cases of (rough) footing embedment were numerically examined: (i) footing at the bottom of a trench, (ii) covered footing, and (iii) embedded footing with full sidewall contact, for which the vertical, horizontal, moment and cross coupling stiffness coefficients were computed. Comparison with readily available and usable analytical and numerical solutions was limited to the vertical loading case. This in some cases verified the finite element solutions, and in other cases highlighted possible limitations in the empirical equations of Gazetas *et al* (1985).

Closer examination of the embedment results was performed in terms of the ratio of the embedded footing stiffness to an equivalent surface footing stiffness. This ratio effectively represents the reduction in footing displacement (or rotation) due to embedment. The results clearly show that a footing with full sidewall contact has a greater increase in stiffness with embedment than a covered footing, and that a covered footing has a greater increase than a footing at the bottom of a trench. The latter two cases of footing embedment approach a constant value of stiffness with embedment depth, while a footing with full sidewall contact approaches a constant gradient of increasing stiffness. For the horizontal and moment loading cases, the influence of embedment on footing stiffness is developed at shallower depths than vertical loading, with an appreciable reduction in horizontal displacement and rotation being observed by an embedment depth of one footing radius.

6.1.3 Stability analysis of a surface footing

The examination of offshore foundation stability was limited to the problem of a rough rigid circular footing placed on the surface of an undrained clay. The plasticity of the clay was modelled by the von Mises yield function. A review of the Meyerhof (1953), Brinch Hansen (1970) and Vesic (1975) bearing capacity solutions is presented, where the combined loading of a circular footing is represented by a number of semi-empirical factors.

For small strain finite element analysis, the mesh dimensions required for accurate stability analysis need only encompass the immediate slip (failure) surface. Therefore a mesh with a radial dimension of $2.33R$ and depth of $1.33R$ was adopted. These mesh dimensions are generally much smaller than those used in previous collapse load studies, and prove to be more computationally efficient.

Finite element analysis of a footing rigidly connected to the soil demonstrated that the conventional 20-node tetrahedron continuum elements do not model adequately the soil-structure interaction when subjected to large horizontal loads. The application of a zero thickness 20-node triangular interface element to model the footing-soil interface alleviated many of the problems experienced by the continuum elements. Unfortunately, the interface elements experienced numerical instabilities under certain combined loading plasticity conditions. The main cause of the instabilities is attributed to the large elastic interface tangent stiffness values used in the analyses, and is thought to be a consequence of incompatibility between the interface and continuum plasticity models. For numerical stability to be achieved, a more modest tangent stiffness value, than is ideally desired for the modelling of a perfectly rough footing-soil interface, was adopted.

Examination of the vertical stress distribution for a rigidly connected footing under large moment loading showed a clearly defined tensile stress zone developed on the side of the footing opposite to the direction of the applied moment. The shape of the zone is reasonably consistent with that postulated by Brinch Hansen (1970) for loss of footing contact due to moment loading, and therefore suggests that interface elements may adequately model these conditions. However, application of interface elements to footings which can lose contact with the soil resulted in numerical instability of the solution. A thorough examination of the causes of this instability was beyond the scope of this research. A more simplistic approach was therefore adopted of

using the rigidly connected footing analyses and calculating the footing loads from the footing nodes where the vertical force component is compressive. For a combination of horizontal displacement and rotation displacement modes, this model produced a first estimate of the shape of the three-dimensional failure envelope (for combined vertical, horizontal and moment loading) at high vertical load.

The numerical stability analysis concluded with a comparison of the computed failure envelope and the inclination factors of the bearing capacity solutions for vertical-horizontal loading. This indicated the Brinch Hansen (1970) and Vesic (1975) solutions to be considerably conservative, while the Meyerhof (1953) solution may be unsafe under large horizontal load.

6.2 Future Research

This thesis presents the preliminary work towards a comprehensive analysis of the behaviour of shallow offshore foundations. The results of this study therefore provide a lot of scope for further research. The numerical elastic analyses of Chapter 4 can be extended to consider conical footings, as applicable to spudcan footings. The effect of embedment is also a key parameter to be examined in this case.

The non-linear three-dimensional finite element model developed in this research requires further development to model accurately the loss of contact between the footing and the soil under moment loading conditions. This will involve further research into the behaviour of interface elements and their application to soil-interaction problems. The improved numerical model can be used to determine the complete three-dimensional combined loading failure envelope for a surface footing, using the approach detailed in Section 5.6. This analysis could also be extended to examine the effect of footing embedment and increasing undrained shear strength with depth (Davis and Booker, 1973).

The finite element model can also be extended to include other constitutive models, such as the Matsuoka yield function (Matsuoka, 1976) to model drained sand. The model could also be extended to include non-linear large strain effects (Burd, 1986).

APPENDIX A NUMERICAL INTEGRATION SCHEMES

A.1 8-point Scheme for Exact Integration of a Cubic Displacement N=3 (Quadratic Strain) Tetrahedral Element

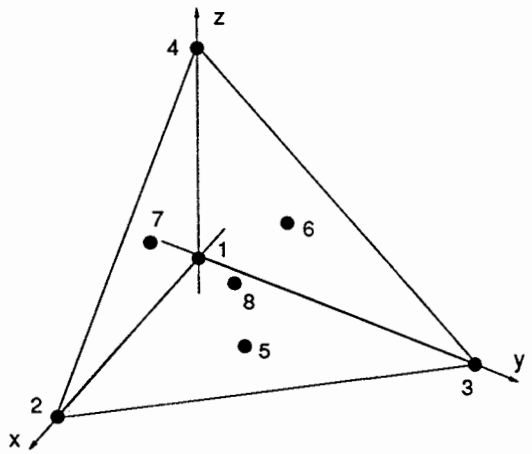

Integration points	Local coordinates (x,y,z)	Weights
1	(0,0,0)	$\frac{1}{40}$
2	(1,0,0)	$\frac{1}{40}$
3	(0,1,0)	$\frac{1}{40}$
4	(0,0,1)	$\frac{1}{40}$
5	$\left(\frac{1}{3},\frac{1}{3},0\right)$	$\frac{9}{40}$
6	$\left(0,\frac{1}{3},\frac{1}{3}\right)$	$\frac{9}{40}$
7	$\left(\frac{1}{3},0,\frac{1}{3}\right)$	$\frac{9}{40}$
8	$\left(\frac{1}{3},\frac{1}{3},\frac{1}{3}\right)$	$\frac{9}{40}$

A.2 10-point Newton-Cotes Scheme for Exact Integration of a Cubic Displacement N=3 (Quadratic Strain) Triangular Element

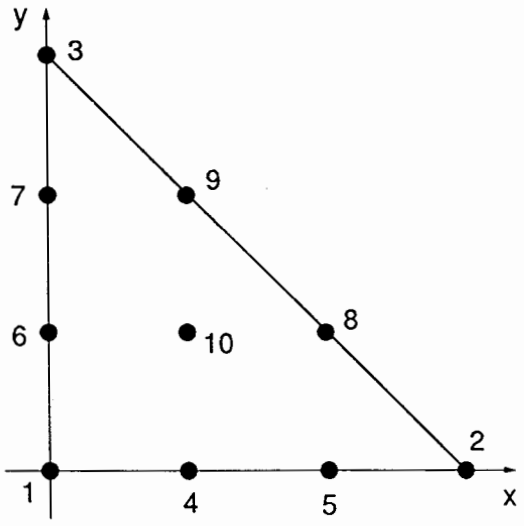

Integration points	Local coordinates (x,y)	Weights
1	(0,0)	$\frac{1}{30}$
2	(1,0)	$\frac{1}{30}$
3	(0,1)	$\frac{1}{30}$
4	$\left(\frac{1}{3},0\right)$	$\frac{3}{40}$
5	$\left(\frac{2}{3},0\right)$	$\frac{3}{40}$
6	$\left(0,\frac{1}{3}\right)$	$\frac{3}{40}$
7	$\left(0,\frac{2}{3}\right)$	$\frac{3}{40}$
8	$\left(\frac{2}{3},\frac{1}{3}\right)$	$\frac{3}{40}$
9	$\left(\frac{1}{3},\frac{2}{3}\right)$	$\frac{3}{40}$
10	$\left(\frac{1}{3},\frac{1}{3}\right)$	$\frac{9}{20}$

REFERENCES

M. Abramowitz and I.A. Stegun, 'Handbook of mathematical functions', National Bureau of Standards, 1964.

K. Arnesen, R. Dahlberg, K. Helge and C.A. Carlsen, 'Soil - structure - interaction aspects for jack-up platforms', *BOSS '88*, Trondheim, 1988.

R.W. Bell, G.T. Houlsby and H.J. Burd, 'Suitability of two and three dimensional finite elements for modelling material incompressibility using exact integration', Oxford University Report Number OUEL 1874/91, Soil Mechanics Report Number 116/91, 1991a. (Submitted for publication in *Int. J. Num. Meth. Eng.*)

R.W. Bell, G.T. Houlsby and H.J. Burd, 'Finite element analysis of axisymmetric footings subjected to combined loads', *7th IACMAG '91*, Cairns, 6-10 May, 1991b.

J.E. Bowles, 'Foundation analysis and design', 3rd edn, McGraw-Hill, 1982.

J. Brinch Hansen, 'A revised and extended formula for bearing capacity', Danish Geotechnical Institute Bulletin No. 28, 5-11, 1970.

H.J. Burd, 'A large displacement finite element analysis of a reinforced unpaved road', DPhil thesis, Oxford University, 1986.

H.J. Burd, 'Personal communication', 1990.

H.J. Burd and C.J. Brocklehurst, 'Parametric studies of a soil reinforcement problem using finite element analysis', *7th IACMAG '91*, Cairns, 6-10 May, 1991.

H.J. Burd and G.T. Houlsby, 'Finite element analysis of two cylindrical expansion problems involving nearly incompressible material behaviour', *Int. J. Num. Anal. Meth. Geomech.* **14**, 351-366, 1990.

R. Butterfield and P.K. Banerjee, 'A rigid disk embedded in an elastic half space', *Geot. Engng.* **2**, 35-52, 1971.

R.N. Bycroft, 'Forced vibrations of a rigid circular plate on a semi-infinite elastic space and on an elastic stratum', *Phil. Trans. Roy. Soc. A.* **248**, 327-368, 1956.

C.R. Calladine, 'Plasticity for engineers', Ellis Horwood, 1985.

Y.K. Cheung and M.F. Yeo, 'A practical introduction to finite element analysis', Pitman, London, 1979.

R.D. Cook, 'Concepts and applications of finite element analysis', 2nd edn, John Wiley & Sons, 1981.

R.F. Craig, 'Developments in soil mechanics and foundation engineering', 4th edn, Chapman & Hall, London, 1987.

E.H. Davis and J.R. Booker, 'The effect of increasing strength with depth on the bearing capacity of clays', *Geotechnique* **23**(4), 551-563, 1973.

R. de Borst, 'Calculation of collapse loads using higher order elements', *Proc. IUTAM Symp.*, Deformation and Failure of Granular Materials (eds P.A. Vermeer and H.J. Luger), 503-513, 1982.

R. de Borst and P.A. Vermeer, 'Possibilities and limitations of finite elements for limit analysis', *Geotechnique* **34**(2), 199-210, 1984.

G. Eason and R.T. Shield, 'The plastic indentation of a semi-infinite solid by a perfectly rough circular punch', *J. Appl. Math. Phys. (ZAMP)* **11**, 33-43, 1960.

P. Frank, A. Guenot and P. Humbert, 'Numerical analysis of contacts in geomechanics', *4th Int. Conf. Num. Meth. Geomech.*, 37-45, 1982.

G. Gazetas, J.L. Tassoulas, R. Dobry and M.J. O'Rourke, 'Elastic settlement of arbitrarily shaped foundations embedded in half-space', *Geotechnique* **35**(3), 339-416, 1985.

A. Gens, I. Carol and E.E. Alonso, 'An interface element formulation for the analysis of soil-reinforcement interaction', *Computers and Geotechnics* **7**, 133-151, 1989.

C.M. Gerrard, 'Solutions for point loads and generalised circular loads applied within cross anisotropic media', C.S.I.R.O Aust. Div. App. Geomech., Tech. Paper No. 28, 1980.

C.M. Gerrard and W.J. Harrison, 'Circular loads applied to a cross-anisotropic half space', C.S.I.R.O. Aust. Div. App. Geomech., Tech. Paper No. 8, 1970.

R.E. Goodman, R.L. Taylor and T.L. Brekke, 'A model for the mechanics of jointed rock', *ASCE, J. Soil Mech. Found. Eng. Div.* **94**(SM3), 637-659, 1968.

D.V. Griffiths, 'Numerical modelling of interfaces using conventional finite elements', *5th Int. Conf. Num. Meth. Geomech.*, 837-844, Nagoya, 1-5 April, 1985.

E.C. Hambly, G.R. Imm and B. Stahl, 'Jackup performance and foundation fixity under developing storm conditions', *22nd Offshore Technology Conference*, Texas, 7-10 May, 1990.

E. Handel, H.F. Schweiger and K.C. Yeo, 'A simple thin-layer element to model soil-geotextile interaction', *Int. Reinf. Soil. Conf.*, Strathclyde, 10-12 September, 1990.

E. Hinton and D.R.J. Owen, 'Finite element programming', Academic Press, London, 1977.

G.T. Houlsby, 'Foundation fixity of spudcan footings', Report prepared for Noble Denton and Associates Ltd, 1984.

G.T. Houlsby, 'Personal communication', 1990.

G.T. Houlsby and C.M. Martin, 'Personal communication', 1990.

K.L. Johnson, 'Contact Mechanics', Cambridge University Press, 1985.

H. Kardestuncer and D.H. Norrie (eds), 'Finite Element Handbook', McGraw-Hill, 1987.

R.D. Krieg and D.B. Krieg, 'Accuracies of numerical solution methods for the elastic - perfectly plastic model', *ASME, J. Pres. Ves. Tech.* **99**, 510-515, 1977.

L.T. Lambe and R.V. Whitman, 'Soil Mechanics', SI Version, John Wiley & Sons, New York, 1979.

M.E. Laursen and M. Gellert, 'Some criteria for numerically integrated matrices and quadrature formulas for triangles', *Int. J. Num. Meth. Eng.* **12**, 67-76, 1978.

H. Matsuoka, 'On the significance of the spatial mobilised plane', *Soils and Foundations* **116**, 91-100, 1976.

G.G. Meyerhof, 'The ultimate bearing capacity of foundations', *Geotechnique* **2**, 301-332, 1951.

G.G. Meyerhof, 'The bearing capacity of foundations under eccentric and inclined loads', 3rd *ICSMFE*, Vol. 1, 440-445, 1953.

D.P. Mondkar and G.H. Powell, 'Evaluation of solution schemes for nonlinear structures', *Int. J. Comput. Struct.* **9**, 237-253, 1978.

J.C. Nagtegaal, D.M. Parks and J.R. Rice, 'On numerically accurate finite element solutions in the fully plastic range', *Comp. Meth. Appl. Mech. Eng.* **4**, 153-177, 1974.

H.G. Poulos, 'Marine Geotechnics', Unwin Hyman, London, 1988.

H.G. Poulos and E.H. Davis, 'Elastic solutions for soil and rock mechanics', John Wiley, New York, 1974.

J.H. Prevost, B. Cuny and R.F. Scott, 'Offshore gravity structures: Centrifugal modelling', *ASCE, J. Geotech. Engng Div.* **107**(GT2), 125-141, 1981.

R.T. Shield, 'On the plastic flow of metals under conditions of axial symmetry', *Proc. Roy. Soc. London Ser. A* **233**, 267-287, 1955.

S.W. Sloan, 'Numerical analysis of incompressible and plastic solids using finite elements', PhD thesis, Cambridge University, 1981.

S.W. Sloan and M.F. Randolph, 'Numerical prediction of collapse loads using finite element methods', *Int. J. Num. Anal. Meth. Geomech.* **6**, 47-76, 1982.

D.A. Spence, 'Self similar solutions to adhesive contact problems with incremental loading', *Proc. Roy. Soc. A.* **305**, 55-80, 1968.

F.S.C. Tan, 'Centrifuge and theoretical modelling of conical footings on sand', PhD thesis, Cambridge University, 1990.

H. van Langen and P.A. Vermeer, 'Finite element analysis of a pile penetration problem in clay', *2nd ENUMGE*, Satander, 18-20 September, 1990.

A.S. Vesic, 'Bearing capacity of shallow foundations', In: Foundation Engineering Handbook, Ch. 3 (eds. H.F. Winterkorn and H.Y. Fang), 1975.

C.P. Wroth and G.T. Houlsby, 'Soil mechanics - Property characterisation and analysis procedures', Proc *11th ICSMFE*, San Fransisco, 1-57, 1985.

H.S. Yu, 'Cavity expansion theory and its application to the analysis of pressuremeters', DPhil thesis, Oxford University, 1990.

M.M. Zaman, 'Evaluation of thin-layer element and modelling of interface behaviour in soil-structure interaction', *5th Int. Conf. Num. Meth. Geomech.*, 1797-1803, Nagoya, 1-5 April, 1985.

O.C. Zienkiewicz, 'The finite element method', 3rd edn, McGraw-Hill, Maidenhead, 1977.

O.C. Zienkiewicz, B. Best, C. Dullage and K.G. Stagg, 'Analysis of nonlinear problems in rock mechanics with particular reference to jointed rock systems', *2nd Int. Conf. Rock. Mech.*, Beograd, 501-509, 1970.